Doctoral Theses at NTNU, 2006:7

Espen Tøndell

CO_2 -expansion work recovery by impulse turbine

NTNU
Norwegian University of
Science and Technology
Doctoral thesis
for the degree of doktor ingeniør
Faculty of Engineering Science and Technology
Department of Energy and Process Engineering

NTNU
Innovation and Creativity

Espen Tøndell

CO_2 -expansion work recovery by impulse turbine

Doctoral thesis
for the degree of doktor ingeniør

Trondheim, January 2006

Norwegian University of
Science and Technology
Faculty of Engineering Science and Technology
Department of Energy and Process Engineering

NTNU
Innovation and Creativity

NTNU
Norwegian University of
Science and Technology

Doctoral thesis
for the degree of doktor ingeniør

Faculty of Engineering Science and Technology
Department of Energy and Process Engineering

ISBN 82-471-7752-8 (printed ver.)
ISBN 82-471-7750-1 (electronic ver.)
ISSN 1503-8181

Doctoral Theses at NTNU, 2006:7

Printed by Tapir Uttrykk

Foreword

This thesis is based on work conducted from August 2002 to November 2005 at the Norwegian University of Science and Technology, Department of Energy and Process Engineering, as a study for the degree Dr. Ingeniør.

The work was financed by the Norwegian Research Council , SINTEF Energy Research, and Norsk Hydro/Shecco Technologies.

The main supervisor was Professor Jostein Pettersen. Co-supervisors were Dr. Petter Nekså and Professor Arne M. Bredesen. I would like to thank my supervisors for

- Good scientific quality on the supervision
- Giving high priority to this work with regards to resource allocation
- Good humour and optimistic attitude

Much of the work has been made in the laboratory, and I will thank the laboratory manager Harald Mæhlum for allocating the necessary laboratory personnel to the project. Most of the personnel in the laboratory have given vital contributions on this project. Especially I would like to mention

- Reidar Tellebon and Arvid Allmening for building the test facility and the nozzle test stand
- Jostein Bakken and Helge Johansen for instrumentation and logging in the test facility
- Gunnar Lohse for building the test facility electrical system and keeping the R-22 cooling plant alive.
- Tore Rye for general assistance through the project period, and lately for assistance in mounting of high speed bearings for the turbine.

Students who have made important contributions are

- Stian Tandberg at heat exchanger design
- Matthias Schweitzer at test facility construction
- Ralf Groß at assisting the experimental work

I would like to thank Ole Gunnar Dahlhaug for taking time to discuss issues related to turbines and how they work. On a general basis I feel that the Norwegian University of Science and Technology and SINTEF Energy Research have many skilled persons who are willing to answer questions and hereby bring the work forwards. Another impression is that

the University Library is well equipped. That is very important for the research effectiveness.

For building up the instrumentation and mechanical system around the turbine I would like to thank Mr. Hans Ammon in the company Nomma in Switzerland. His contribution was on engineering, production and installation of all the mechanical components necessary for measuring torque and speed on the turbine, in a high-pressure chamber and with little space available. He also welcomed me twice in Switzerland for following up the production of the system. Another important supplier is Maccon GmbH in Germany. They have supplied a high-speed motor for the test facility. When parts shall be delivered for research and development, most suppliers do not want to quote for that delivery. Maccon delivered the necessary motor, and gave assistance until the motor was working as intended.

Because a lot of effort has been made on this work, I have been able to see my girlfriend, family, friends and relatives less than I wanted. I think it is enough to make one Dr. Ingeniør study in a life time, therefore I will not be busy with Dr. Ingeniør related work in the future.

To those who only read the part of this report showing that the tested expander had low efficiency, I would say: "Read the whole report!" I have asked my self if it is justified to spend a lot of resources on investigating a machine when it turns out to be inefficient. The research on turbines for CO_2 expansion should not be stopped because of the results shown in this report. There is a potential for the technology if optimized parts are used together with a design that matches the purpose. Let this study be the first of many on this theme.

Trondheim 18.12.2005

Espen Tøndell

Summary and conclusions

Literature review and theoretical background

This study focuses on refrigeration processes with relatively low cooling capacities and hereby low circulation rates. The presented theory for turbines focuses on work extraction in impulse turbines. For an impulse turbine, the optimal rotational speed gives a turbine blade tip speed equal to half the nozzle jet velocity. With small volume flow rates, the turbine will have small dimensions, and hereby the rotational speed will be high.

Together with principles for work extraction, the losses in the turbine were discussed. The main losses are

- Nozzle losses (Friction and incomplete flashing)
- Rotational losses
  - Disc friction
  - Windage
  - Changing angles
- Non-rotational losses
  - Fluid friction between jet and turbine blade
  - Jet not hitting turbine blade
- Mechanical losses in bearings

A literature survey was made to show some examples on two-phase turbines and to create a theoretical basis for fluid expansion in a nozzle. The literature survey on two-phase expanders showed some examples on Helium expanders with small dimensions and good efficiencies. Compared to a helium expander, a CO_2 expander will be working on a higher pressure, and hereby some extra losses must be expected. Some work on expander for R134a was also referred. That work was however focused on high cooling capacities, which means that the R134a expander will have much higher mass flow than the CO_2 expander in this study. The literature survey on fluid expansion and nucleation showed that the critical radius is important in nucleation. The critical radius is dependent on the surface tension and the difference between the liquid saturation pressure and the local pressure. For the current study, understanding of nucleation will be important in order to understand the function of the nozzle. Finally some models for critical flow were presented.

Evaluation and design of model expander

A design basis for this study was defined with basis in cooling capacities and process conditions that an expander might meet in mobile air conditioning.

Consideration of n_s-d_s diagrams for various machines showed that the ideal expander would be a Pelton type expander. A pure Pelton expander however has a special 3-dimensional geometry, so manufacture was considered to be expensive in sensible dimensions. Therefore it was decided to compromise on the turbine geometry in order to be able to gain some experience with an impulse turbine for CO_2. The resulting turbine was a radial outflow impulse turbine with one nozzle. The nozzle had 1.02 mm outlet diameter and the rotor wheel had 15 mm diameter on the inner circle (turbine inlet), whereas the outer diameter (turbine discharge) was 20 mm.

Some considerations were made with regards to utilization of the expansion energy. Regarding dimensions and pressure differences it would be preferable to utilize the expansion energy in a pre-compressor.

Experimental equipment

A test facility was built for testing of various expansion equipment. The test facility was equipped in order to make control of the inlet- and outlet conditions of the expander possible. And in order to have an oil-free system where lubricant in the CO_2 flow could not disturb the expander performance, the CO_2 circuit contained a condenser after the two-phase expander. Then there was a liquid pump for pressure elevation, and a heater for raising the temperature until the desired value. As the uncertainties in inlet- and outlet conditions were expected to play an important role in the total uncertainty of each experiment, the instruments measuring these properties were paid special attention. The mass flow was measured by a Coriolis meter from Rheonik, whereas inlet and outlet temperatures were measured by PT100 transmitters.

Experimental program, methods and data processing

First, goals and process conditions for the experimental program were set up. It was decided to combine three values for inlet pressure with three values for outlet pressure and three values for inlet temperature. This makes 27 experiments in the full program.

Nozzle test setup and expander performance test setup were described in detail. For nozzle testing, the reactive power was measured, and the average nozzle jet velocity was derived from that. In turbine performance testing, an electrical motor was used as a brake for the turbine. On the electrical motor's stator, the rotary torque was measured.

A brief test procedure for nozzle- and expander tests was given, whereas data processing and extrapolation of data were described in detail.

Experimental results

An extensive experimental program has been made in order to characterize the function of the turbine and its individual parts. The experimental program consisted of

- Nozzle testing
  - Straight bore nozzle
  - Convergent-divergent nozzle, polished and non-polished
  - Convergent-divergent nozzle, inlet distribution plate
  - Flow visualisation tests at non-violent conditions
- Expander blocked shaft testing
- Turbine performance testing
  - Bearing tests
  - Disc friction tests
  - Turbine tests

The nozzle characterisation tests showed efficiencies between 0.5 and 0.7 for the convergent-divergent nozzle, and 0.55-0.65 for the straight bore nozzle. For all the nozzle tests, the uncertainties could be as high as ± 0.1 No clear differences can be seen between the performances of the polished nozzle towards the non-polished one. The tests with a multiple holes orifice plate at the nozzle inlet showed very low performance.

Nozzle flow visualisation tests were only possible for relatively non-violent conditions. Already at these conditions, however, there were considerable secondary fluid flows and the nozzle jet was conically shaped.

The blocked shaft testing showed that measured torques were between 50 and 70 % of the optimal ones. Considering the fluid flow visualisation, it is natural to assume that a considerable part of this deviation origins from jet not hitting the turbine blade.

The bearing- and disc friction tests showed considerable losses. And the turbine tests showed that the turbine did not reach the desired speed when it was driven by CO_2. Possible reasons for the turbine not reaching the desired speed are bearing and disc friction losses, in addition to windage losses that must be high as long as the turbine blades are not shielded. Another important loss is the loss caused by the jet not hitting the turbine blades.

Discussion

The experimental results were analysed, in order to find the reasons for the losses in the process. The nozzles had high losses, caused by friction and incomplete expansion. The incomplete expansion can to some extent

be reduced by improving the nozzle design. The nozzle also showed a conical jet shape, which means that some part of the nozzle jet would be expected to not hit the turbine blades. Experiments with blocked shaft confirmed that considerable parts of the nozzle jet did not hit the turbine blade.

In the expander performance testing, the intended turbine rotational speed was not reached. Analysis of the losses in the turbine showed that the most important loss sources were the exit losses, the losses from the jet not hitting the turbine blades and rotational losses. When the rotational losses are high at the low speed reached with experiments, they will become very high if design speed is reached. If the liquid discharge from the turbine was handled better than it is now, it should be possible to reduce the rotational losses.

Conclusion

The experimental work showed that the turbine had low efficiency. The turbine diameter was however too big, which introduced extra fluid friction losses and the principle with outflow turbine introduced extra exit losses, as well as extra disc friction losses because the principle leads to an outer tip speed higher than the recommended tip speed at the turbine blades' inlet. The concept with radial outflow turbine should not be used.

An improved design was suggested. In that design, the turbine was still a radial impulse turbine, but the flow direction was inwards. Estimations of the efficiency showed that it would be possible to achieve 39 % internal efficiency with normal turbine speed, and with reduced speed the possible internal efficiency was 45 %. Both of the calculations showed that the turbine would suffer from exit losses. If it was possible to reduce the exit losses, an impulse turbine for CO_2 expansion could be feasible. One possible way to reduce the exit losses is to use an axial impulse expander.

In order to reduce rotational losses, the turbine blades should be shielded. If this increases the speed, the exit losses are also reduced.

If it was possible to have an impules turbine with 50 % total efficiency, which might be possible with an axial turbine in this scale, Figure 2-4 and Figure 2-5 show that the potential COP for 35 °C condenser outlet temperature would be 3.3, which means that the COP would increase by 18 % as compared to the case where expansion energy was not recovered. This calculation assumes:

- Compressor efficiency 70 %
- Evaporator temperature 5 °C
- Superheat at compressor inlet 2 K

Appendix 2-5 contain the detailed experimental measurements. These are available on a CD on request. Requests can be directed to: espentondell@hotmail.com

1 Introduction

1.1 CO2 based refrigeration

Due to the environmental impact from emissions of HCFCs and HFCs from refrigeration, it is desirable to find alternative solutions with refrigerants that already occur in the nature. One obvious candidate as refrigerant is CO_2 which was used as refrigerant before the fluorocarbons were discovered. Emissions of CO_2 are less harmful to the environment than emissions of fluorocarbons, and if the CO_2 is recovered from a waste gas or exhaust gas, the net environmental impact from CO_2 based refrigeration is zero.

The use of CO_2 as a refrigerant gives challenges, as CO_2 requires high pressure in the process. As new compressors and heat exchangers have been developed some important challenges have been handled. In addition to the environmental advantages, CO_2 has good qualities for heat transfer because it has a high specific heat capacity. A CO_2 based refrigeration process also operates at high pressure, which means that the medium has high density. This gives low volume flows and compact equipment.

In a vapour compression process the refrigerant is usually throttled at constant enthalpy from high pressure at the condenser to low pressure at the evaporator. This represents a loss in every refrigeration process. With fluorocarbon processes throttling losses are small, and expansion work recovery would give small COP improvements. With trans-critical CO_2 processes the throttling losses are considerable.

It is important to be aware that the expansion process starts as a supercritical liquid or dense-phase gas. And the expansion end-point will be in the two-phase region. In a two-phase expander there are some extra challenges compared to a single-phase expander.

1.2 Research focus

The primary focus for this thesis is the expansion of supercritical CO_2, in a two-phase impulse expander. This is interesting because it can improve the efficiency of refrigeration processes that use CO_2 as refrigerant.

One important subject is the evaluation of previous work within CO_2 expansion. This forms the basis for selecting work principle for the machine in this study. Parallel with the evaluation of different work

principles, design rules will also be considered, because the design affects the performance.

The main focus of this thesis is to investigate the work recovery from CO_2 expansion, and how the expansion performance depends on different design and process parameters. The losses in the expansion process will be given special attention as the improvement of a performance depends on the knowledge of losses. This means that losses in each expander component must be traced and characterized.

As the expansion ends in the two-phase region, special challenges regarding two-phase expansion must be considered. For an impulse expander consisting of a nozzle and a turbine wheel, the two-phase expansion gives some extra challenges compared to single-phase expansion.

The experimental basis of the thesis is limited to one refrigerant, CO_2. It is also limited to one work principle, impulse expander. The expansion process evaluation will be focused on, but not limited to, process conditions that are relevant for use in mobile or residential air conditioning.

2 Literature review and theoretical background

2.1 Principle of refrigeration processes

2.1.1 Refrigeration cycle

Heat flows spontaneously from a source with high temperature to a sink with lower temperature. By the use of a vapour compression process the direction of the heat flow can be turned as shown in Figure 2-1.

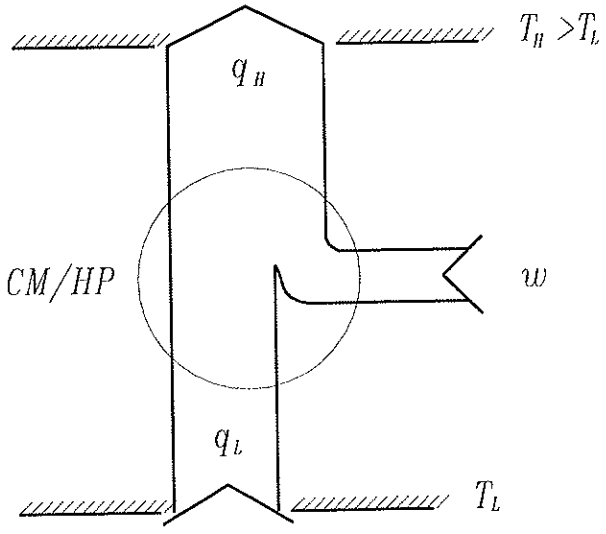

Figure 2-1: The principle for heat-pumping from a cold source to a hot sink. The notation CM/HP denotes that the figure is valid for Heat pumps and cooling machines

The idealized form of this process is represented by the reversed Carnot cycle consisting of:
1-2: Reversible heating of the refrigerant
2-3: Isentropic compression
3-4: Reversible heat emission
4-1: Isentropic expansion

This is shown in Figure 2-2.

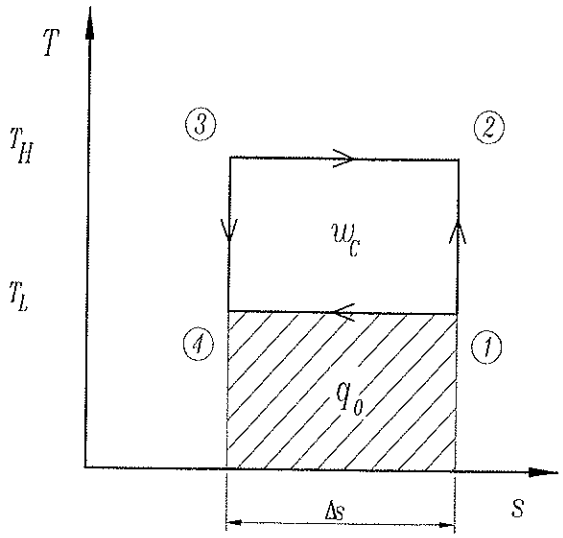

Figure 2-2: The reversed Carnot cycle

Real processes contain losses due to irreversibilities. The most important losses are heat exchanger losses, compressor losses, superheating loss and the throttling loss. As shown in Figure 2-3 these losses increase the compressor work W_{th} compared to the Carnot work W_C.

2.1.2 Throttling contra expansion work recovery

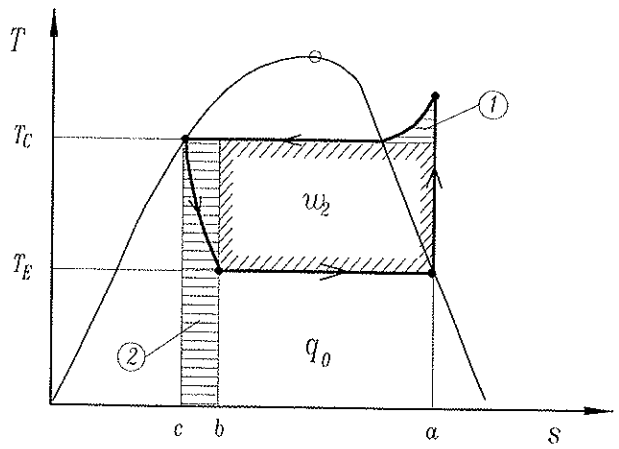

Figure 2-3. Losses in the vapour compression process

As shown in Figure 2-3, the throttling loss equals the product of the ambient temperature and the throttling entropy formation. The work W_2 corresponds to the work W_C shown in Figure 2-2 when there are no losses in the heat exchangers, and when all heat is rejected isothermally.

The throttling loss increases the compressor work and reduces the refrigeration capacity. In a throttling process, the enthalpy is constant. As shown in Figure 2-3, the temperature decreases in the throttling process, and the entropy depends on the amount of vapour formed in the throttling. A medium with a low heat capacity and high vaporization enthalpy will have a low vapour formation and hereby a low entropy formation, whereas a medium with high heat capacity and low vaporization enthalpy will have a high entropy formation.
The heat capacities and the vaporization enthalpies are compared for various refrigerants in Table 2-1. The table shows that the vaporization enthalpies are comparable, whereas the heat capacity for CO_2 is much higher than the fluorocarbon heat capacities. This explains why the throttling loss is considerable for CO_2 and not so important for fluorocarbons.

Table 2-1. Comparison of heat capacity and vaporization enthalpy for various refrigerants at T = 278 K. Data from the in-house facility Rn-lib.

Refrigerant	R11	R12	R22	R717	R744
C_p [kJ/kgK]	0,86	0,93	1,19	2,76	2,66
Δh_{vap} [kJ/kg]	187	149	201	1244	216

For ammonia (R717), the vaporisation enthalpy is much higher than for all the other refrigerants. Because of this, the throttling loss for ammonia is low. As the throttling loss reduces the refrigeration capacity and increases the compression work, the potential for COP improvement by expansion work recovery is considerable when CO_2 is the refrigerant.

If the throttling is replaced by a work extracting expander, the process will not have a constant enthalpy as the enthalpy decreases with the work performed. The reversible, adiabatic expansion will have constant entropy, but in real processes there will be some losses due to friction, leakages and incomplete expansion giving an entropy rise. Still, the entropy formation in the work extracting expansion will be smaller than the throttling entropy formation. The work extracting expansion will hereby give higher cooling capacity and reduced need for compressor work.

2.1.3 COP for process

For a cooling process where a work is done in order to transfer heat the Coefficient of Performance (COP) is defined as

$$\varepsilon = \frac{Q}{W} \tag{2-1}$$

Here Q denotes the cooling capacity, and W denotes the compressor work. In a heat pump the COP is defined as

$$\varepsilon = \frac{Q + W}{W} \tag{2-2}$$

Here the compressor work is emitted in the condenser

Expansion work recovery affects the process efficiency. For a refrigeration process with expansion work recovery, the COP becomes

$$\varepsilon = \frac{Q + \eta_{i,\exp} \cdot \Delta h_{\exp}}{W - \eta_{\exp} \cdot \Delta h_{\exp}} \tag{2-3}$$

Where $\eta_{i,exp}$ denotes the expander internal efficiency and η_{exp} denotes the total expander efficiency including bearing losses. Equation (2-3) shows that there is a potential for efficiency improvement if the expansion enthalpy is high, and the expander efficiency is sufficient.

The COP improvement potential with use of expansion work recovery in a trans-critical cycle is shown in Figure 2-4. Here the optimal COP is plotted vs. gas cooler outlet temperature. For a trans-critical cycle it is possible to optimize the high-side pressure as this is supercritical. The optimal pressure is recognized as the point where

$$\left(\frac{\partial \varepsilon}{\partial p}\right)_{T_C, p_E} = 0 \tag{2-4}$$

at constant gas cooler outlet temperature and evaporator pressure. The optimal pressures were estimated by numerical differentiation.

Figure 2-4 and Figure 2-5 are valid for trans-critical CO_2 cycles. They are interesting with regards to evaluating the impact of expansion work recovery on a refrigeration process. In Figure 2-4, the COP is plotted vs. High side outlet temperature, and with expander efficiency as parameter. The figure shows high COP-values for the lowest temperatures, and the COP decreases quickly with increasing temperature. At high temperature the COP becomes so low that expansion work recovery has a high relative impact.

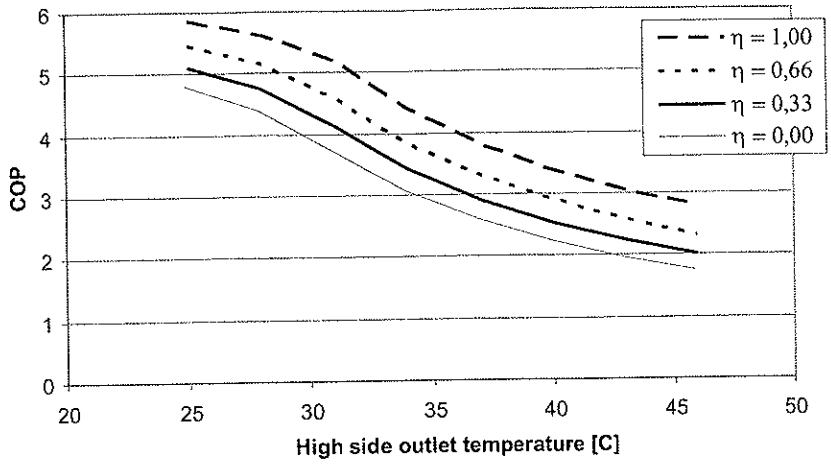

Figure 2-4: COP improvement potential at different expander efficiencies @ 5°C evaporator temperature, with expander efficiency as parameter

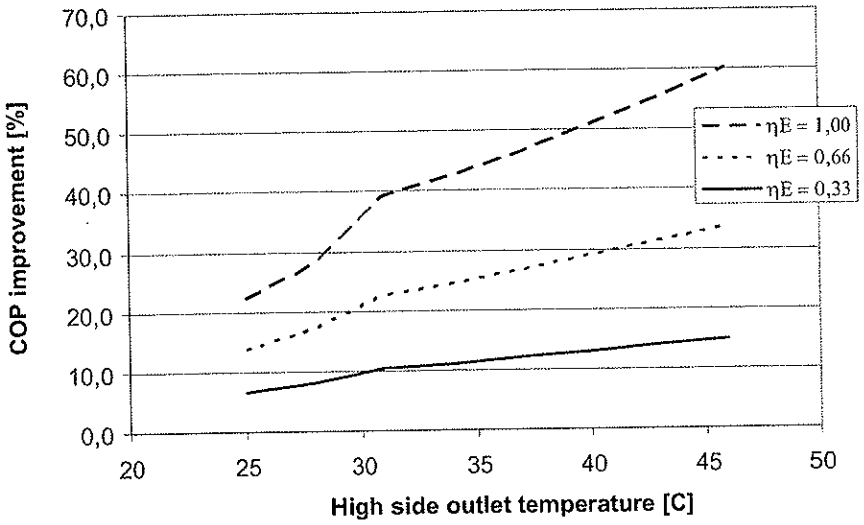

Figure 2-5. Relative COP improvement potential@ 5°C evaporator temperature, with expander efficiency as parameter

Figure 2-5 shows the relative COP improvement potential at various expander efficiencies and gas cooler temperatures. The figure shows that the improvement potential is highest at high gas-cooler temperatures, and

that the use of an expander is justified even at moderate expander efficiencies.

The curves in Figure 2-4 and Figure 2-5 were calculated by use of the following assumptions

- Compressor efficiency 70 %
- Evaporator temperature 5°C
- Superheat at compressor inlet 2 K

2.2 Expander working principles

Expansion machines can be categorized according to their working principle. This is done in Figure 2-6

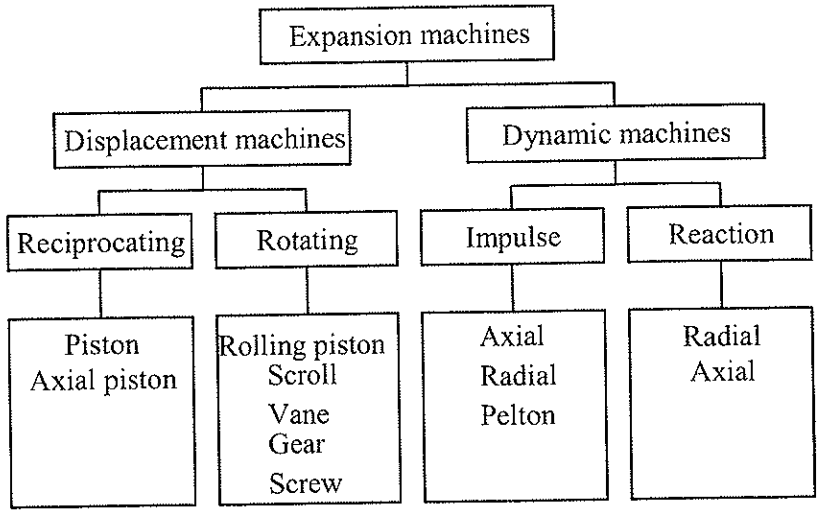

Figure 2-6. Expansion machines sorted by working principle.

On the first level, there are the positive displacement machines and the dynamic machines. The displacement machines close a chamber containing the working medium at high pressure. Then the working fluid expands as the volume increases and the machine performs work. Displacement machines are then organized as reciprocating machines or rotating machines in the second level. The dynamic machines are organized as impulse and reaction machines, and they work according to different principles. In the impulse machines the energy is converted to velocity in a nozzle. The jet from the nozzle is then deflected in the rotor blades or buckets. In the reaction machines, part of the energy is converted to velocity before entering the rotor. In the rotor, both pressure and velocity is converted into shaft work in the rotors.

2.3 Choice of working principle for experimental turbine

Although this study is not focused on displacement machines as the studies in this state of the art, it is important to evaluate earlier work in order to set a standard for expander performance.

2.3.1 CO2-Expansion state of the art

Piston

When CO_2 is used as refrigerant in a circuit with maximum cooling capacity around 10 kW, as in mobile air conditioning, relatively small volume flows of CO_2 are used at high pressure. For a compressor-expander Heyl et al. (1998) chose a piston machine due to its' simple design and working principle.

Heyl & Quack (1999) showed how a piston compressor-expander unit would look. The unit, compressing and expanding in one step has one fundamental energetic disadvantage. If the expansion work shall be used to compress a gas, the forces on the expansion side must be higher than the contra forces on the compression side. If the expansion work is to be completely utilized, the forces in the expansion chamber will at some point be lower than the forces in the compression chamber. Because of this, the unit had to be operated according to the full pressure principle, and hereby only the displacement work at constant pressure was used.

Some experimental results were presented in Heyl et al. (2000). They showed that the expander could have a high mechanical efficiency, but the frequency was only 0.38 Hz. The author reports that the two phase CO_2 is removed from the expansion chamber without big problems after the expansion. However, the low frequency gives a high volume compared to machines working at frequencies up to 1000 Hz.

In Heyl & Maurer (2002) the possibilities for a process with two compression steps is discussed. Here the expansion work will be used in the second compression step. The authors also discuss the possibility of cooling the gas between the compression steps, which will improve the efficiency of the process.

Heyl (2001) pointed out that it would be possible to utilize up to 98 % of the expansion work with more expanders working in series even though each of them worked according to the full pressure principle. In Nickl et al. (2003) the third generation compressor-expander using a piston machine is presented. Here there are three expansion steps, and hereby the

machine is expected to achieve 80 % efficiency, but three steps make a very complex system. And because the frequency will still be low, it will give a high-volume system. The principle of the third generation compressor-expander is shown in Figure 2-7.

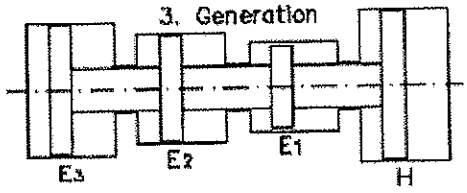

Figure 2-7: Principle of Third generation compressor-expander, copied from Nickl et al (2003)

Nickl et al (2003) says nothing about vibrations and noise from the combined compressor-expander. The machine must however be expected to have some vibrations and noise because a large piston is moving inside of it. But the low frequency will reduce the strength of the noise and the vibrations.

Axial piston

Heidelck & Kruse (2000) suggests the use of an axial piston expander for CO_2 expansion. Compared to a standard hydraulic pump, the control disc must be modified so that only part of the cylinder is filled with CO_2 before the expansion, and hereby the expansion work can be fully utilized. In Heidelck & Kruse (2001), the first referred result is that the leakages between the cylinder and the control disc must be investigated closer. Figure 2-8 shows a compressor-expander unit based on the axial piston principle. The compressor part is in the top, and the expander part in the bottom. Maurer & Zinn (1999) tested various axial piston machines, and the highest reported efficiency was around 0.5 and with a machine suffering from high internal leakages.

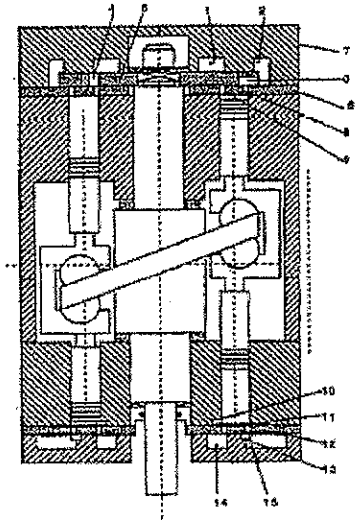

Figure 2-8: Axial piston compressor-expander unit, copied from Heidelck & Kruse (2001)

Gear

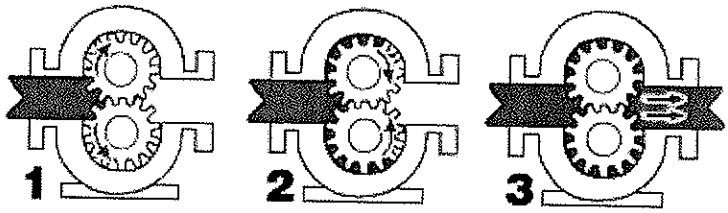

Figure 2-9: Principle of gear compressor or expander, copied from http://www.pumpschool.com/principles/external.htm

Figure 2-13 shows the principle how a gear compressor or expander works. For an expander, high-pressure fluid enters the machine. The fluid is then transported to the low-pressure side without volume change, and enters the low-pressure side with an isenthalpic throttling, and hereby the volume change work is not utilized in this kind of machine.

Maurer & Zinn (1999) investigated both gear and axial piston expanders. The reason was that displacement machines are used in hydraulics at equal pressures and volume flows. The axial piston machine gave a lot of noise, and both machines had maximal isentropic efficiency around 0,5. For the axial piston machine the main losses were due to leakages and dead volumes. The main losses in the gear expander were leakages and the throttling loss because only the displacement work could be utilized.

Försterling et. al (1999) investigated a gear compressor for CO_2. The results showed isentropic efficiencies between 0.6 and 0.8 dependent on the pressure ratio, with the lowest efficiencies at the highest pressure ratios. The volumetric efficiency based on the PV-diagram varied between 0.7 and 0.9 with the lowest efficiencies at the highest pressure ratios. This supports the conclusion that leakage losses are high in a gear expander.

Gear compressor was tested in a student project, Jonassen (1991). Here a three step gear compressor was tested.

Rolling piston

Zha et al. (2003) suggested the use of a roller piston expander due to its' simple construction and low cost. A loss analysis was made, and the most important losses are due to leakage and friction. Calculations showed that an isentropic efficiency of 0.5 could be reached, and that the friction losses dissipate 24 % of the ideal expansion power, whereas the leakage losses dissipate 25 %. For control of inlet and outlet flows, electrically controlled valves were suggested. Figure 2-10 shows the principle of the rolling piston expander.

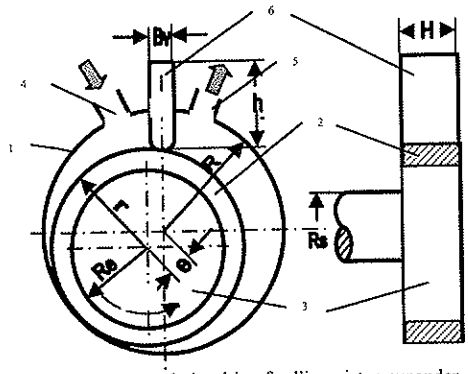

The cylinder parameters relationship of rolling piston expander
1-cylinder 2-rolling piston 3-eccentric shaft 4-suction 5-discharge 6-vane

Figure 2-10: Principle of rolling piston expander, copied from Zha et al. (2003)

Scroll

An experimental investigation of a scroll expander was presented by Huff et al. (2003). A scroll compressor for R134a was modified by cutting the walls. This of course gave a wrong relationship between the wall height and the axial clearings, which in turn led to a very low isentropic efficiency. The maximum efficiency was reported to 0.28. Tests were also made with an unmodified scroll compressor. This expander had maximum efficiency of 0.42, and a maximum volumetric efficiency of 0.68, increasing with the speed. Figure 2-11 shows the internals of a scroll expander. One part is rotating, and the other one is static.

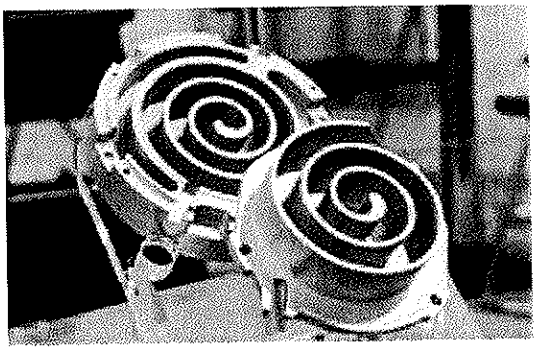

Figure 2-11: Internals of scroll expander, copied from http://www.affordair.com.au/images/whatisaircon/scroll%20compressor.JPG

Vane

Fukuta et al. (2000) made a feasibility study for a vane compressor for CO_2. The study showed that the leakages are critical for the compressor performance. They also evaluated the possibility for a compressor-expander combination where the expander helps a one-step compressor. The results showed that combining the compressor and the expander can increase the volumetric and internal efficiencies of the compressor, but the mechanical efficiency is lowered because the rotational torque is lowered due to torque recovery in the expander. The results also showed that there are large torque fluctuations in this machine.

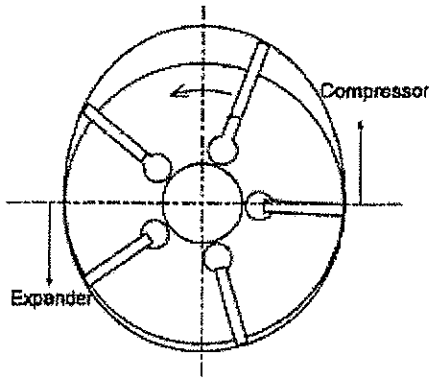

Figure 2-12: Principle of Vane compressor-expander combination, copied from Fukuta et al. (2001)

The combination of a compressor and an expander for expansion work recovery is discussed by Fukuta et al. (2001). The principle of the compressor-expander unit is shown in Figure 2-12. The study shows that this machine has a simple structure, and that there is no need for control valves at inlet and outlet from the machine. Furthermore the study shows that this machine will suffer from under-expansion because the expanding gas exits before it is completely expanded due to a small expansion volume.

A mathematical model was developed by Fukuta et al (2003). This model takes flow restriction; internal leakages and heat transfer into account. Calculations based on the model showed that the internal leakages had the biggest influence on the performance. A prototype expander was also built. The performance of this increased with the speed, and the best value achieved was a total efficiency of 0.43, and a volumetric efficiency of 0.64 at a rotational speed of 2000 rpm.

2.3.2 Criteria for selection of expander

The following criteria were used for the selection of the working principle of the expander

Efficiency (Maximum and off-design performance)
This is the key criterion as this decides the process COP improvement, and hereby the competitiveness of the process towards other processes with other refrigerants. The maximum (design point) and off-design performance is however difficult to predict. The selection is then based on the performance of CO_2 expanders reported in the literature, and available knowledge about losses in the chosen type of expander.

Constant shaft torque
A constant shaft torque makes it easy to use the energy in a compressor on the same shaft. With a compressor on the same shaft, no shaft sealing will be needed, and the energy can be used directly without conversion to electricity by a generator. This means that the use of a compressor on the same shaft will be the most efficient solution. If the shaft torque has variations, there are methods to store the energy temporarily, but the use of such methods also represents extra complexity and possible losses. It is also important to note that the expander shaft torque may have variations as long as they match the required compressor torque.

Simple work principle and simple geometric shape
With a simple work principle it is easy to understand and describe the function of the expander, and it is easier to manufacture a machine with high reliability. With a good understanding, it is then less challenging to improve the function. A simple geometric shape is also connected to this, and it makes the production less challenging, which again means a lower price both for the model expander and an expander in practical use.

Suitability for small volume flows
The work is directed towards use in mobile and residential air conditioning. This means that relatively small cooling capacities will be needed, and hereby the volume flows will be small. Some kinds of expansion machines are better suited for small volume flows than others.

Compactness/speed
If the expander shall be used in mobile air conditioning in the future, compactness and weight will be very important. If the equipment is less compact, the weight will also be high. In mobile air conditioning, a high weight will reduce the total energy saving potential.

2.3.3 Reciprocating machines

The piston expander is well suited for small volume flows because of small leakages. With the 3rd generation expander, Nickl et al. (2003), where the CO_2 is expanded in three steps and the expanding CO_2 is used to compress CO_2, the efficiency is reported to be 0.80. The piston type of machine also has a simple work principle. However, the expansion in three steps makes the solution very complex, and the machine has a very low frequency, around 6 Hz, which means that the machine requires a big volume and has a high weight. With a heavy piston moving inside the compressor-expander unit, noise and vibrations might also be a challenge. Regarding efficiency however, the 3rd generation expander of Nickl et al. (2003) is the best one presented until now.

The axial piston expander is a good idea with regards to utilization of the volume change work, as there are more parallel pistons where CO_2 is expanded, and the pistons are always on different places in the expansion cycle. Because of this, the fluctuations in expander shaft torque would be expected to be small. The tests however showed that the machine suffers from internal leakages and effects from dead volumes. With more parallel cylinders, the friction losses would also be expected to be considerable because there will be a large contact area between the piston and the housing. With many parallel pistons, each requiring precise manufacture, the costs might be high, and there will be many moving parts.

2.3.4 Rotating machines

Gear expander

The gear expander is interesting due to its simple work principle. The expander tested by Maurer & Zinn (1999) showed an efficiency of 0.5, which is one of the best results reported in the literature review. One very important loss in this machine is the unrestrained expansion loss that occurs because the machine has a constant volume and hereby the volume change work is not utilized. This kind of loss can never be reduced by improvements in design and manufacture.

Rolling piston and vane

In the literature review it was shown that the roller piston and vane expander suffer from considerable internal leakages, and hereby the efficiencies of these machines will be low. Probably it is also difficult to improve the sealing of these machines without increasing friction-related losses. For a rolling piston machine, the working principle leads to an unstable shaft torque, and a need for control valves both on the inlet and the outlet. For the vane expander no control valves will be needed, but also here there are large fluctuations in the shaft torque. For the roller piston, calculations showed that an isentropic efficiency of 0.5 could be

reached, and for the vane expander a maximal total efficiency of 0.43 was achieved in experiments.

Scroll

The scroll expander is interesting because of low fluctuations in shaft torque, and because of relatively good match between the expander shaft torque and the compressor shaft torque. Another advantage with this machine is the absence of control valves. The machine however has a complicated geometry, and it has a long gap between the rotating and the non-rotating part, that is difficult to seal. The gap could possibly be reduced by more precise machining of all the parts in the expander, but there will still be a need for some gap in order to allow for thermal expansion. High requirements for precise machining would also increase the costs of the unit. The scroll expander reported by Huff et al. (2003) showed a maximum measured efficiency of 0.42.

2.3.5 Selection of expander working principle

The literature review shows that previous work has been concentrated on expanders working by the displacement principle. Displacement machines are well covered although a screw expander has never been tested. The screw expander has a complex geometry, and would not be suitable in the relevant dimensions, mainly due to internal leakage. In general the tested machines suffer from internal leakages, which cause the losses and the low efficiencies.

Except from the scroll expander, the displacement machines show a bad correspondence between available momentary shaft torque in the expander and the required momentary torque for a compressor on the same shaft. This increases the challenges with the further utilization of the expansion work by driving a compressor on the same shaft. For the piston expander and the roller piston expander, one possible solution to this problem is to run the machine as a full-pressure machine, and accept that the volume change work is lost. This solution introduces a 20 % loss, so it is not a desirable solution. The third generation piston expander, Nickl et al. (2003), solved this problem, and gave an acceptable efficiency. This solution however requires many moving parts and many control valves. So the solution is too complex.

The reciprocating expanders and the roller piston expander require control valves on the inlet and outlet of the expansion chamber. This causes losses, it makes the machine more complex and it introduces challenges with process control.

A summary of the displacement machines is presented in Table 2-2. The column with efficiencies also contains information about whether the efficiency is calculated or measured, and which efficiency is contained.

Table 2-2. Summary of the displacement machines' properties

Machine	Efficiency Basis/type	Torque	Control valves	Remarks
Piston *)	0.80 isentropic/ predicted	Stable	Yes	High complexity
Axial piston	0.50 isentropic/measured	Stable	Yes	High leakages
Rolling piston	0.50 isentropic/predicted	Unstable	Yes	High leakages
Gear	0.50 isentropic/measured		No	Unrestrained expansion
Scroll	0.42 isentropic/measured	Stable	No	Complex geometry
Vane	0.43 total/measured	Unstable	No	

*) 3rd generation compressor-expander of Nickl et al. (2003)

Due to the challenges discovered by previous research on various CO_2 expanders working by the displacement principle, it is desirable to try something new. Although dynamic machines with various dimensions are used for two-phase expansion work recovery in other kinds of processes, like LNG (Liquid Natural Gas) production, there are no references to researchers testing this with CO_2. Therefore this work will focus on the recovery of expansion work from CO_2 expansion in a dynamic machine.

A dynamic machine will have the following advantages

- Constant shaft torque
- Compactness
- Only one moving part
- Control valves may be needed for control of mass flow and high side pressure, but they are not as important as for piston, axial piston and rolling piston expanders.

The use of a dynamic machine introduces the following challenges

- As volume flows will be low, the dimensions will be small and the machine will rotate at high speed.
- High speed gives challenges regarding bearings and power utilization
- Small dimensions give challenges regarding manufacture, geometry and tolerances
- Two-phase flow. This gives some challenges in all CO_2 expanders, but requires special attention in a dynamic machine
- Maintaining low losses and high efficiency although some compromises might be made regarding the construction

It is difficult to predict the efficiency of such a machine, so it must be tested in order to evaluate the performance.

2.4 Theory for impulse turbines

2.4.1 Energy conversion in nozzle

The working principle of an impulse expander is to reduce the pressure in the medium through a nozzle and hereby convert pressure energy into velocity. The nozzle process is shown in an hs diagram in Figure 2-13.

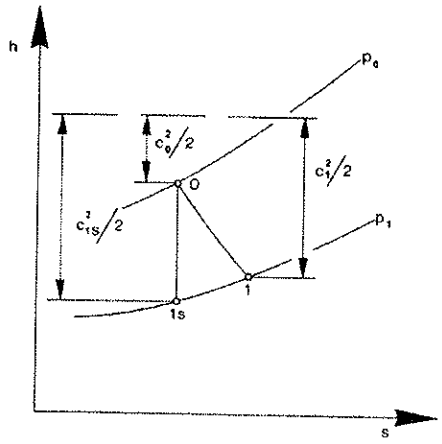

Figure 2-13: hs-diagram for nozzle pressure release, figure copied from Øverli (1992)

In a fluid flow between the states 0 (nozzle inlet) and 1 (nozzle outlet), the following energy balance applies

$$h_0 + \frac{c_0^2}{2} + g \cdot z_0 = h_1 + \frac{c_1^2}{2} + g \cdot z_1 + q \qquad \textbf{(2-5)}$$

When nozzle flow is considered, the height difference is very small compared to the other parts of the equation, so this is neglected. The flow is also assumed to be adiabatic, so the following equation results

$$h_0 + \frac{c_0^2}{2} = h_1 + \frac{c_1^2}{2} \qquad \textbf{(2-6)}$$

The maximal jet velocity leaving the nozzle is represented by the isentropic pressure reduction, where all the available energy is transferred into velocity

$$c_{1s} = \sqrt{-2 \cdot \Delta h_s + c_0^2} \qquad \textbf{(2-7)}$$

And the real velocity out of the nozzle is

$$c_1 = \varphi\sqrt{-2 \cdot \Delta h_s + c_0^2} \tag{2-8}$$

Where φ is the velocity coefficient of the nozzle. The nozzle isentropic efficiency is

$$\eta = \frac{c_1^2}{c_{1s}^2} = \varphi^2 \tag{2-9}$$

And the total energy losses in the nozzle are given by

$$\Delta Y = \left(1 - \eta_{nozzle}\right) \cdot \Delta h_s \tag{2-10}$$

As the nozzle flow is flashing, it is also compressible, and the energy balance becomes

$$\frac{1}{2} \cdot \left(c_1^2 - c_0^2\right) = \int_0^1 dh = -\int_0^1 v dp \tag{2-11}$$

The differential form of this energy balance is

$$d\left(\frac{c^2}{2}\right) = cdc = -vdp \tag{2-12}$$

Combining this with the differential form of the continuity equation yields

$$\frac{dA}{A} = -\frac{d\rho}{\rho} + \frac{vdp}{c^2} \tag{2-13}$$

A stepwise integration of this equation gives the desired internal shape of a nozzle without losses. This equation also applies for nozzles with supersonic flow.

For a two-phase nozzle the principal expansion path in a pressure-enthalpy diagram is shown in Figure 2-14. At entering, the fluid is in the single-phase region. The pressure is then reduced until the two-phase region is reached. Here, there is saturation temperature when the flow is at equilibrium. Then the pressure is further reduced until the outlet state is reached.

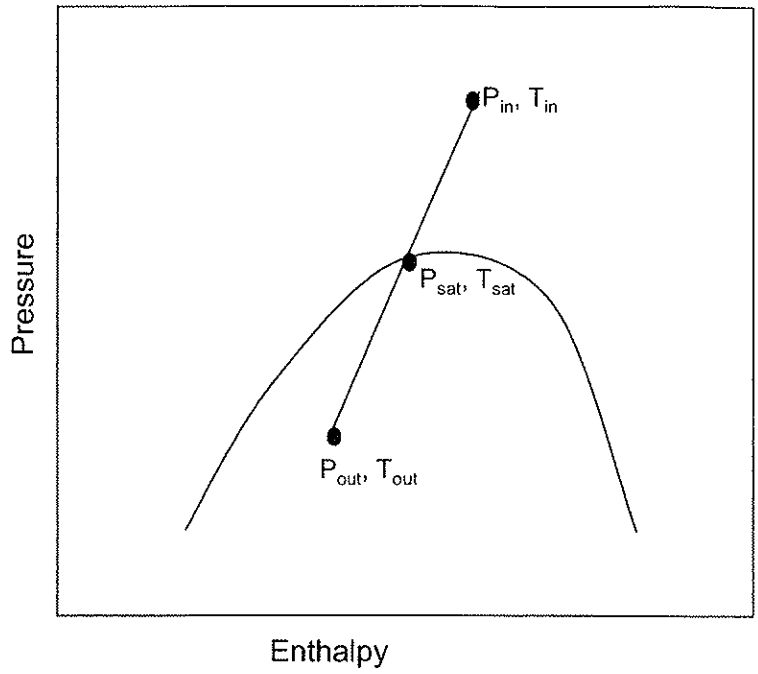

Figure 2-14. Principal two-phase expansion path

Figure 2-15 shows in a PV-diagram the expansion process in a two-phase nozzle. From the inlet, the depressurization follows the isentropic path, or close to it. Then at some point the process starts departing from equilibrium because the kinetic of the flashing process is too slow, and hereby the pressure will decrease more than it would by following the isentropic path. The deviation from the isentropic path due to departure from equilibrium causes a loss called the flashing loss in this study.

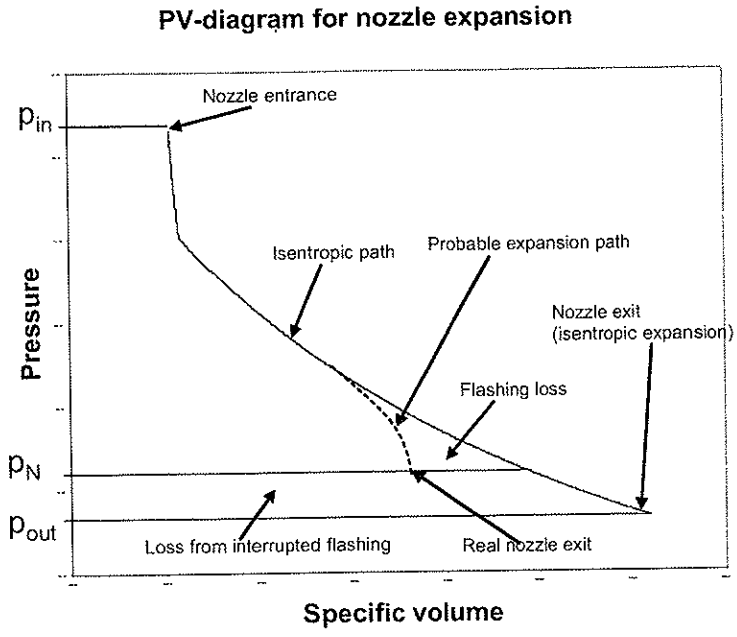

Figure 2-15. Flashing losses in nozzle

Figure 2-15 also shows that there are two important losses in addition to the friction losses; the flashing loss and the loss from interrupted flashing. The loss from interrupted flashing can be explained by the fluid not reaching the possible exit pressure because the nozzle geometry is not matched with the critical flow conditions in the nozzle. When this occurs, there is a shock on the nozzle outlet, and the nozzle jet is divergent. When the jet leaves the nozzle, it will experience a lower pressure, and the available pressure energy is not utilized. The indicated pressure p_N is the calculated end pressure for the nozzle expansion, whereas p_{out} is the measured surrounding pressure.

2.4.2 Work extraction in an impulse turbine wheel

Figure 2-16 shows jet deflection in a Pelton turbine, which gives rise to work extraction in such a turbine. In every impulse turbine, pressure energy is converted to velocity in a nozzle, and then the nozzle jet is deflected in the turbine wheel. A Pelton turbine has a high efficiency because the jet is deflected almost completely in this turbine.

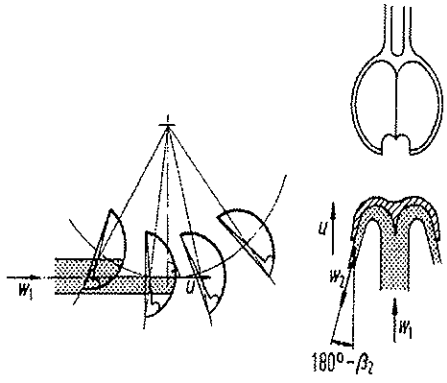

Figure 2-16: Deflection process in Pelton turbine buckets, copied from Fister (1984)

Figure 2-17 shows the principal velocity triangles at entrance and exit of a radial outflow impulse turbine rotor. A real rotor is moving, so that the velocity diagrams are not representative for a whole cycle.

Properties of the velocity diagram

- c_2 represents energy that has not been extracted in the runner wheel, the discharge loss. The discharge loss is minimized by optimizing β_2
- For the tip velocities $u_1 < u_2$
- The relative velocities, w_1 and w_2 are nearly constant
- The angle between the nozzle jet and the tip velocity is represented by α_1 and the angle between relative velocity w_1 and turbine blade is represented by β_{1u} in the velocity diagram.
- For a Pelton turbine α_1 and β_{1u} are zero which means that the nozzle jet hits the bucket parallel with the tip velocity.

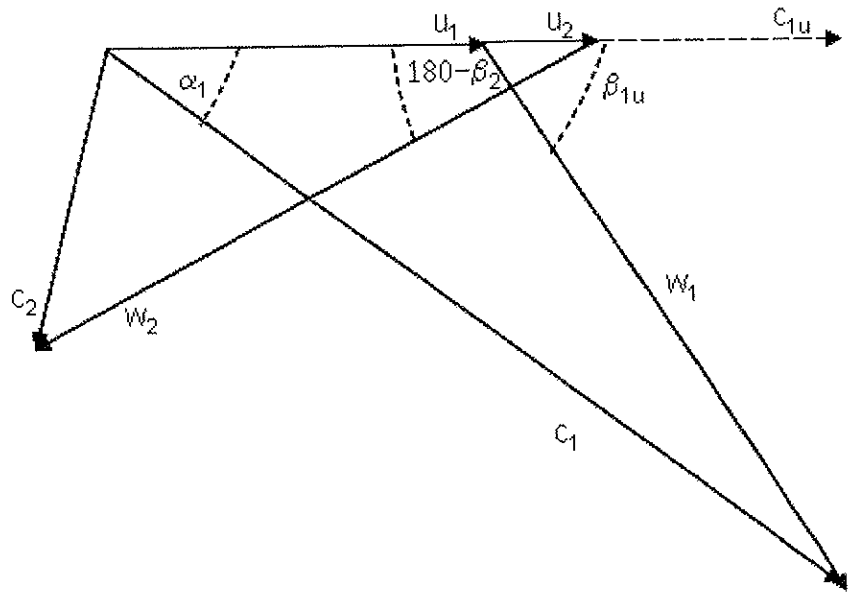

Figure 2-17: Velocity diagrams for general impuls turbine rotor.

The power from the free jet, or the maximal energy to be extracted from the jet in a general impulse turbine is given by

$$P = \frac{1}{2} \cdot \dot{m} \cdot c_1^2 \tag{2-14}$$

Whereas the turbine shaft power is

$$P = M \cdot \omega \tag{2-15}$$

And the turbine hydraulic efficiency is

$$\eta = \frac{M \cdot \omega}{\frac{1}{2} \cdot \dot{m} \cdot c_1^2} \tag{2-16}$$

The theoretical turbine rotary torque is

$$M = \dot{m} \cdot \left(r_2 \cdot c_{2u} - r_1 \cdot c_{1u} \right) \tag{2-17}$$

Where

$$c_{1u} = c_1 \cdot \cos \alpha_1 \tag{2-18}$$

$$c_{2u} = u_2 - w_2 \cdot \cos(180 - \beta_2) \quad \textbf{(2-19)}$$

r_1 and r_2 are radii at rotor blade inlet and outlet.

The maximal turbine torque at optimal speed is then

$$M = \dot{m} \cdot c_1 \cdot \cos\alpha_1 \cdot \left(r_2 \cdot \left(\frac{r_2}{2r_1} - \frac{\cos(180 - \beta_2)}{2\cos\beta_{1u}} \right) - r_1 \right) \quad \textbf{(2-20)}$$

For a non-rotating turbine Eq 2-17 transforms to

$$M = \dot{m} \cdot (r_2 \cdot c_1 \cdot \cos(180 - \beta_2) + r_1 \cdot c_1 \cdot \cos\alpha_1) \quad \textbf{(2-21)}$$

Using Eq 2-18 and 2-19, with $u_2 = 0$

Measuring the torque for a non-rotating turbine gives information about nozzle efficiency and losses in the turbine blade. Rotational losses are not included in such measurements, as they can only be measured with a rotating turbine.

As can be seen from Figure 2-17 there is an angle α_1 between nozzle jet and rotor tip velocity. The highest energy utilization is achieved by minimizing this angle.

2.4.3 Losses

Nozzle flow resistance losses

The main flow resistance losses in the nozzle occur due to flow resistance in the nozzle, and due to turbulence at sudden contractions or enlargements in the entrance- and exit sections of the nozzle. Nozzles for test purposes will for simplicity be manufactured with abrupt contractions. These losses can be estimated by correlations for pressure drop taken e.g. from Idel'cik (1994). One correlation for the coefficient of local resistance to an abrupt contraction at $Re > 10^4$ is

$$\xi_{loc} = \frac{\Delta p_{loc}}{\left(\rho c_0^2 / 2\right)} = 0.5 \cdot \left(1 - \frac{A_0}{A_1}\right) \tag{2-22}$$

Where A_0 is the cross section area after the contraction, c_0 the velocity after the contraction and A_1 is the cross section area before the contraction. There are also other correlations for resistance in abrupt contractions. They will not be considered in this work because the contraction loss is expected to have low importance.

The single phase friction pressure loss in the nozzle can be calculated by

$$\Delta p = \xi \cdot \rho \cdot \frac{c^2}{2} \cdot \frac{\Delta l}{d} \tag{2-23}$$

Where ξ is the friction factor dependent on the relative surface roughness and Reynolds number.

Incomplete and nozzle flashing losses

When supercritical CO_2 is depressurized enough, vapour formation starts. This also happens in a convergent-divergent nozzle. In the flashing process, there will not be equilibrium between gas and liquid. And if equilibrium is not reached at the nozzle exit, the energy potential is dissipated after the nozzle exit, causing turbulence. These losses are shown in Figure 2-15. If the expansion is stopped before the surrounding pressure is reached, the interrupted flashing loss occurs.

Hydraulic losses due to tilting, friction and exit

In the turbine blade, there are losses due to inlet geometry, friction and deflection. The loss due to inlet geometry arises if the nozzle jet velocity contains a component in one direction that will not be deflected, e.g. if the

nozzle is tilted. This loss is called the tilting loss in this study, and it is described by

$$P_{tilting} = \dot{m} \cdot \frac{c_1^2}{2} \cdot \left(1 - \cos^2 \lambda\right) \tag{2-24}$$

Where λ is the nozzle tilting that origin from the nozzle not approaching the turbine directly, as shown in Figure 2-18.

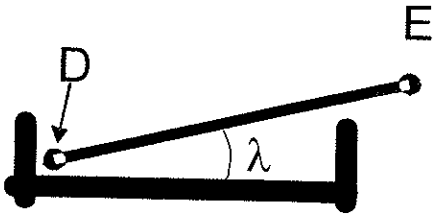

Figure 2-18. Nozzle approaching turbine wheel

As the bucket flow is instationary, the loss due to friction is hard to describe. As a best estimate, it is possible to estimate the drag loss for homogeneous fluid flow over a flat plate and use this.

At the rotor outlet, the fluid absolute velocity is c_2, this represents a non-utilized kinetic energy and hereby a loss of energy.

$$P_{exit} = \dot{m} \cdot \frac{c_2^2}{2} \tag{2-25}$$

The fluid absolute velocity, c_2, can be calculated by use of the velocity diagram for the rotor outlet, and basic trigonometry. High friction losses will reduce the exit loss because the friction reduces the fluid flow velocity.

Internal rotational losses

A rotor will be exposed to friction forces on the outer surfaces of the wheel. This causes the disc friction power loss, which according to Schlichting (2000) is described by

$$P_{disc} = C_M \cdot \frac{1}{4} \cdot \rho \cdot \omega^3 \cdot R_{rotor}^5 \tag{2-26}$$

Here C_M is a friction coefficient.

In an impulse turbine the fluid is delivered to the runner wheel through nozzles. The buckets of the turbine are filled with fluid during the rotation. As the buckets are not exposed to fresh fluid continuously, the "resting" fluid in the buckets must be accelerated and displaced when the bucket goes into the nozzle jet. And when the buckets leave the nozzle jet, there will be an under-pressure on the inlet side that causes whirling and suction of gas from the surroundings. This loss is called the windage loss, and according to Øverli (1992) it is described by

$$P_{windage} = k_V \cdot \omega^3 \cdot R_{Rotor}^4 \cdot h \cdot \rho \cdot (1-\varepsilon) \quad \textbf{(2-27)}$$

Here k_v is a friction coefficient dependent on the turbine wheel's geometrical shape, h is the turbine blade height, and ε is the fraction of the turbine perimeter covered by the nozzle.

The shaft rotating in the fluid is also exposed to friction, which causes the shaft friction loss. Compared to the bearing and windage losses, this loss is expected to be small, especially when the turbine wheel is exposed to two-phase flow, whereas the shaft is only exposed to gas.

The three losses mentioned will be difficult to isolate, so they are treated together. In extrapolation of measurements it is assumed that

$$P_{rot} \propto \omega^3 \cdot R_{rotor}^4 \cdot (R + k \cdot h)$$

k is proportionality constant because the windage loss is $\sim\omega^3 R^4 h$.

Mechanical losses in bearings

When the shaft is rotating, there is friction between the shaft and the bearings. The characteristic loss from this is measured ahead of the experiments by making the turbine rotate and measuring the speed and the rotational torque with vacuum in the turbine housing so that other friction sources are eliminated.

The bearing torque is according to Brändlein et al (1999) described by

$$M_m[Nm] = 10^{-10} \cdot f_0 \cdot (\nu \cdot n)^{\frac{2}{3}} \cdot d_m^3 + 0{,}001 \cdot f_1 \cdot P_1 \cdot d_m \quad \textbf{(2-28)}$$

Where f_0 and f_1 are factors dependent on the type of bearing, ν is the bearing lubrication viscosity, n is the bearing speed d_m is the bearing pitch circle diameter and P_1 is the load.

The bearing loss is then

$$P_m = M_m \cdot \omega \quad \textbf{(2-29)}$$

Other losses

If the jet leaving the nozzle is conical, there will be a radial velocity component that is not registered on the nozzle jet velocity measurement. This velocity component would be expected to be symmetrical around the axis, and perpendicular to the axial velocity. This is the reason why it is not detected on the nozzle jet velocity measurements. It can however be evaluated by nozzle jet flow visualization. The appearance of a non-axial jet is caused by incomplete expansion in the nozzle, as well as turbulence in the flow. As the turbine was designed for a concentrated, axial jet, part of a conical jet will not hit the turbine blade and hereby cause a loss.

As the turbine is rotating in normal operation, the jet's position compared to the rotor will be constantly changing. This causes a loss because the jet will be hitting from non-optimal positions. In addition to this some fluid might be reflected from the turbine blades when the jet hits between two blades. These losses are known as stagnation losses according to Hays & Brasz (1996).

If the two-phase nozzle flow is not homogeneous, this will cause losses due to flow separation. Liquid has higher inertia than gas. Hereby the liquid will be more difficult to accelerate than the gas, and the flow will not be homogeneous. If the liquid velocity is slower than the gas velocity, liquid droplets might hit the turbine blades' back side and hereby decelerate the turbine.

There will be a friction between the jet and the surrounding medium. This loss is however assumed to be small and have low importance.

Total internal effect of turbine

The total internal effect of an impulse turbine is described by

$$P_i = \dot{m} \cdot \Delta h_s \cdot \eta_{nozzle} \cdot (\cos\lambda)^2 - P_{not-hit} - P_{drag} - P_{rot} - P_{exit} \qquad \textbf{(2-30)}$$

- The first term denotes the available power from the nozzle jet entering the turbine wheel
- $P_{not\text{-}hit}$ denotes losses related to friction in turbine blades and jet not hitting the bucket
- P_{drag} denotes losses related to friction between the jet and the turbine blades
- P_{rot} denotes losses caused by the rotation of the turbine wheel, wuch as windage, disc friction, two-phase losses and losses due to changing angles

- P_{exit} denotes the power loss due to the kinetic energy in the fluid leaving the turbine
- λ is the tilting angle as shown in Figure 2-18.

2.4.4 Similarity parameters for turbo machines

The similarity parameters for a turbo machine define the operating and design conditions where machines of similar design geometry experience similar fluid dynamic conditions. These parameters enable the comparison of machines and the evaluation whether a machine's geometry will be suitable for a given set of operating conditions.

The most important parameters are the specific speed, Baljè (1981):

$$n_s = \frac{\omega \cdot \sqrt{\dot{V}}}{(g \cdot H_{ad})^{3/4}} \tag{2-31}$$

And the specific diameter:

$$d_s = \frac{D \cdot (H_{ad} \cdot g)^{1/4}}{\sqrt{\dot{V}}} \tag{2-32}$$

For a turbine the volume flow ($\dot{V}$) refers to the outlet conditions and for a pump or a compressor to the inlet conditions.

2.5 Efficiency

2.5.1 Nozzle

The nozzle efficiency is defined as the ratio of the measured nozzle jet kinetic energy to the possible nozzle jet kinetic energy by isentropic expansion

$$\eta_{nozzle} = \frac{c_{jet}^2}{2 \cdot \Delta h_s} \tag{2-33}$$

This efficiency includes all the losses in the nozzle.

2.5.2 Hydraulic

The hydraulic efficiency is defined as the ratio of the energy released in the turbine wheel to the possible energy release in the turbine wheel. The possible energy release in the turbine rotor is equal to the kinetic energy of the nozzle jet. The actual energy release equals the kinetic nozzle jet energy minus

- Tilting losses
- Exit losses

- Windage, disc and shaft friction losses
- Fluid friction between the jet and the surrounding
- Two-phase losses
- Losses from jet not hitting blades
- Losses from changing angles

$$\eta_h = \frac{\dot{m} \cdot \frac{c_{jet}^2}{2} - P_{tilting} - P_{not-hit} - P_{rot} - P_{exit} - P_{friction}}{\dot{m} \cdot \frac{c_{jet}^2}{2}} \quad \textbf{(2-34)}$$

2.5.3 Internal

The internal efficiency is the product of the nozzle and the turbine wheel efficiency

$$\eta_i = \frac{P_i}{\dot{m} \cdot \Delta h_s} = \eta_{nozzle} \cdot \eta_h \quad \textbf{(2-35)}$$

This means that the internal effect equals

$$P_i = \eta_i \cdot \dot{m} \cdot \Delta h_s \quad \textbf{(2-36)}$$

2.5.4 Mechanical

The mechanical efficiency is the ratio of the internal work minus mechanical losses to the internal work.

$$\eta_m = \frac{P_i - P_m}{P_i} = \frac{P_{shaft}}{P_i} \quad \textbf{(2-37)}$$

P_m represents the mechanical losses in the bearings, and P_{shaft} represents the available power on the shaft.

2.5.5 Total

The total efficiency of the turbine is the ratio of the shaft power to the shaft power achieved by isentropic expansion

$$\eta_{tot} = \frac{P_{shaft}}{\dot{m} \cdot \Delta h_s} = \frac{M_{shaft} \cdot \omega}{\dot{m} \cdot \Delta h_s} \quad \textbf{(2-38)}$$

This efficiency then equals the product of the internal and the mechanical efficiency

$$\eta_{tot} = \eta_i \cdot \eta_m \quad \textbf{(2-39)}$$

2.6 Literature survey

2.6.1 Two-phase and single-phase expanders

The principle of energy recovery from two-phase air/water flow in a Pelton-type turbine was tested by Akagawa & Asano (1986). They tested deflection of two-phase flow in a stationary impulse blade with simultaneous reactive power measurement on the blade for various gas- and liquid mass flow rates. The results showed that the hydraulic efficiency decreased very sharply at a void fraction higher than 0.8, and that power was generated from water, because water has a much higher density than atmospheric air. The results also showed that the maximal hydraulic efficiency was around 0.75 at zero void fraction, and then the hydraulic efficiency decreased linearly to around 0.6 at void fraction 0.8. The maximal power output ranged from 0 to 280 W, water flow rate from 0.167 to 2.2 kg/s. And the impulse blade corresponded to a turbine pitch circle diameter of 200 mm.

Peirs et al. (2003) reported a single-stage axial impulse turbine with rotor diameter 10 mm. Tests with compressed air showed 18.4 % efficiency at 100000 rpm speed. For efficiency testing, acceleration was measured, and then the torque was derived from the acceleration and momentum of inertia. By measuring the turbine deceleration, friction torque was also measured. A loss analysis showed that the main losses were the blade profile losses (31.6 %), and the exit losses (34.2 %). The blade profile losses arise due to friction between fluid and turbine blades.

2.6.2 Expansion work recovery from refrigerants

Brasz (1995) showed a two-phase turbo expander for use with R134a in water cooled chillers, in the capacity range 1000-2000 kW. The turbine wheel was a pure axial impulse turbine wheel as shown in Figure 2-19. The axial design was chosen to eliminate the potential negative effects of liquid re-entering the rotor

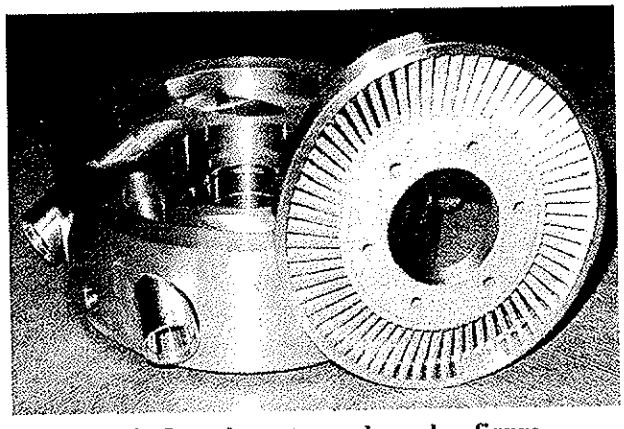

Figure 2-19. Impulse rotor and nozzles, figure copied from Hays & Brasz (1998)

after discharge. Liquid re-entering the rotor after discharge is a possible problem for other impulse expanders e. g. if the nozzle sets up a secondary flow profile or the discharge is too optimistic designed. The nozzle was convergent-divergent to allow for supersonic discharge velocities. On the nozzle entrance there was a multiple-hole orifice plate, which function was to initiate nucleation for a large number of small vapour bubbles over the whole cross section. This was done to create a uniform two-phase jet with minimum slip velocity. The turbine was incorporated in a system consisting of a compressor, motor and the turbine. The turbine effect was used to reduce the necessary motor effect. The use of a multiple-hole orifice plate at the nozzle entrance might also be interesting for expansion of CO_2.

Hays & Brasz (1996) reported results from thests of a two-phase axial impulse expander as described previously by Brasz (1995). The test results showed a total turbine efficiency of 50-55 %. The nozzle efficiency was 84 % at design conditions, so the rotor efficiency was 60-65 %. This is lower than the predicted 75 % rotor efficiency, but the predictions did not account for stagnation losses. One possible reason for stagnation losses is that liquid droplet flow is reflected from the leading edges of the blades, and hereby never makes it through the rotor. The nozzle efficiency of 84 % shows that it is possible to achieve acceptable performance on a two-phase nozzle. But for comparison to CO_2 expansion, it is important to remember that Hays & Brasz (1996) worked with R134a, and with much higher cooling capacities. Compared to CO_2, the R134a expander works under lower pressure, which means that windage and disc friction losses will be lower. With much higher cooling capacities, the relative importance of rotational losses will be lower.

Sato et al. (1983) studied an impulse steam turbine with low vapour quality. The turbine had 0.64 m pitch circle diameter and 70 blades. Experimental testing showed increasing turbine efficiency with decreasing vapour quality. The turbine was also tested for partial admission, which showed lower efficiency than full admission. At eight active nozzles the ratio of hydraulic efficiency to maximal hydraulic efficiency was 0.8, whereas 16 active nozzles gave a ratio of 0.9.

Sixsmith et al. (1990) tested a miniature Helium expander for low temperatures. The turbine was described in Sixsmith (1971), and it was a radial inflow expander with axial discharge. At the discharge there was two-phase Helium. The efficiency of the turbine was measured to 50 %, whereas the expected efficiency was 72 %. In the tests, the mass flow rate was lower than expected due to nozzle clogging. This might also have

caused the lower efficiency. The turbine rotor diameter was 4,76 mm and the design speed 384000 rpm.

Izumi et al. (1986) developed a Claude cycle helium refrigerator with a two-stage expansion micro turbine, with a radial inward flow reaction turbine wheel. The micro turbine mass flow rate was 2,8 g/s, and the expander first and second stage rotational speeds were 816000 and 519000 rpm. The turbine has been tested at inlet temperatures of -188 °C and 27 °C. At the lowest temperature the highest measured adiabatic efficiency was 0.4 at a non-optimal expander speed. From the measured data, the adiabatic efficiency at an optimal speed was estimated to 0.5.

2.6.3 Nucleation and flashing

A sub-cooled liquid can be depressurized through a convergent-divergent nozzle. In the convergent-divergent section, the cross section area decreases, the fluid flow velocity increases, and the pressure decreases. At some point, the gas-liquid equilibrium line is crossed, and the liquid is in a superheated, meta-stable state. Here the liquid might start to nucleate as the equilibrium pressure of the superheated liquid is higher than the system pressure. The start of nucleation initiates the flashing process, where gas is evaporated from the superheated liquid. Theoretically, the flashing can proceed until the gas-phase and the liquid-phase have the same temperature, and equilibrium is achieved.

Blander & Katz (1975) made a review about homogenous and heterogeneous nucleation. One of the fundamental equations in nucleation theory, the equation for the minimum work needed to form a bubble, is derived in the article:

$$W = \sigma \cdot a - (P_G - P_L) \cdot V_G + x \cdot (\mu_G - \mu_L) \qquad \textbf{(2-40)}$$

The work of bubble formation as a function of the bubble volume increases until the bubble reaches the critical volume. Bubbles smaller than the critical volume tend to collapse, whereas bubbles larger tend to continue to grow spontaneously. When the bubble gas phase pressure equals the liquid vapour pressure, the bubble critical radius (r_c) is implicitly expressed by

$$P_V = P_L + \frac{2 \cdot \sigma}{r_c} \qquad \textbf{(2-41)}$$

Such a bubble is in chemical equilibrium with the liquid by the fact that the bubble pressure equals the vapour pressure. Eq (2-41) shows that it is in mechanical equilibrium with the liquid phase. As the pressure difference and the surface tension are important parameters for nucleation,

they will also be important for the flashing and hereby for the efficiency of a two-phase nozzle.

If the nucleation is sufficiently rapid, the nucleation process can terminate itself, as the nucleation lowers the local liquid temperature, and hereby the potential for flashing is reduced. If heat was conducted through the walls, the flashing could however be maintained.

Blinkov et al (1993) presented the differential equations for calculation of the vapour fraction downstream of the throat in a convergent-divergent nozzle for expansion of sub cooled water. A method for solving the equations was also presented. Comparisons between calculations and experimental data showed that the wall nucleation dominated the bulk nucleation in nozzles with a small diameter e.g. 4 mm, whereas the bulk nucleation gained more importance in nozzles with bigger diameters e.g. 50 mm. The referred results from Blinkov et al (1993) are valid for water, and to be relevant for flashing CO_2, they have to be scaled. The general trend, that smaller diameter gives more importance to wall nucleation, should however be valid for both fluids.

Corty & Foust (1955) investigated the effects of surface roughness and contact angle on the nucleation and bubble formation. The results showed big differences in the necessary superheat to initiate nucleation, dependent on the surface roughness. The results however were achieved during boiling where heat was added to the system.

2.6.4 Critical flow models

Kim & O'Neal (1995) presented various two-phase critical flow models, and comparisons of the models to results with HFC134a and HCFC22. The general form of the critical flow equation presented in the article was

$$G_{cr}^2 = \frac{-1}{\frac{\partial}{\partial p}\left\{\frac{x\cdot k+(1-x)}{k}\cdot\left[(1-x)\cdot k\cdot v_f + x\cdot v_g\right]\right\}} \qquad \textbf{(2-42)}$$

k represents the ratio of the vapour to liquid velocity. For homogenous flow, $k = 1$. Assuming a homogenous frozen model (HFM) where the interfacial mass transfer is restricted due to insufficient time, no mass transfer between the phases ($\partial x/\partial P = 0$) yields the Wallis HFM

$$G_{cr} = \left[-\left(x\cdot\frac{\partial v_g}{\partial p} + (1-x)\cdot\frac{\partial v_f}{\partial p}\right)^{-1}\right]^{1/2} \qquad \textbf{(2-43)}$$

Measurements for comparison were made for vapor fractions < 0.2. The comparisons showed that there was good correspondence between the model and the experimental data.

3 Evaluation and design of model expander

This Chapter summarizes and evaluates various dynamic expansion machines, and selects the machine to be used in this work. Then the chapter suggests design rules for the selected expander, and shows the design of the model expander built for function testing.

State functions and other physical properties of CO_2 necessary for design were calculated by the in-house library Rn-lib, where the CO_2 data are based on Angus et. Al (1976), Fenghour et. Al. (1998), Pitzer & Schreiber (1988) and Vesovic et. al (1990).

3.1 Design basis

For evaluation of expander concepts and design of model expander with nozzle, the conditions given in Table 3-1 apply

Table 3-1. Process conditions for expander design

Property	Unit	Value
Inlet temperature	°C	30
Inlet pressure	Bara	100
Outlet pressure	Bara	40
Mass flow	kg/s	0.05

The design conditions were chosen so because they are close to the real conditions that the expander will meet in CO_2 based refrigeration e. g. in mobile air conditioning. The mass flow corresponds to a cooling capacity of about 10 kW, and 444 W isentropic expander effect at the chosen outlet (evaporator) pressure. The inlet pressure was chosen to 100 bara, which is relatively close to the optimal gas-cooler pressure with regards to gas-cooler outlet temperature, as described in Eq (2-4)

Table 3-2 contains data gained by use of Eq (2-7) together with the continuity equation, and assuming isentropic nozzle expansion and negligible inlet velocity to the nozzle.

Table 3-2. Nozzle throat and outlet conditions with isentropic expansion

Property	Unit	Value
Throat velocity	m/s	101
Throat specific volume	m^3/kg	0.00135
Throat diameter	mm	0.92
Jet velocity	m/s	133
Specific volume	m^3/kg	0.00287
Jet diameter	mm	1.17

The conditions at the throat were estimated by assuming that the equilibrium line is crossed in this point.

3.2 Selection of turbine work principle

A dynamic machine for small volumetric flow rates of CO_2 rotates with a constant shaft torque, at high speed and has a small diameter. The small diameter makes the machine compact. For the displacement machines discussed, there was a problem with match between the momentary expander shaft torque and the shaft torque of an eventual compressor in a combined compressor-expander unit. For dynamic machines, this is not a problem as the compressor will require a constant shaft torque, and the expander delivers a constant shaft torque. If the energy is utilized in a generator, the generator will also run very well on a constant shaft torque.

Control valves will not be important in a dynamic machine although they may be present for control of mass flow. This reduces the machine complexity and process losses in control valves. A total compressor-expander unit with energy recovery either by a compressor on the same shaft or by a generator can also be made hermetical, so it will be a self-contained unit without a shaft sealing.

It is important to note that the experimental turbine rotor shall be designed according to standard design rules for turbines as far as possible.

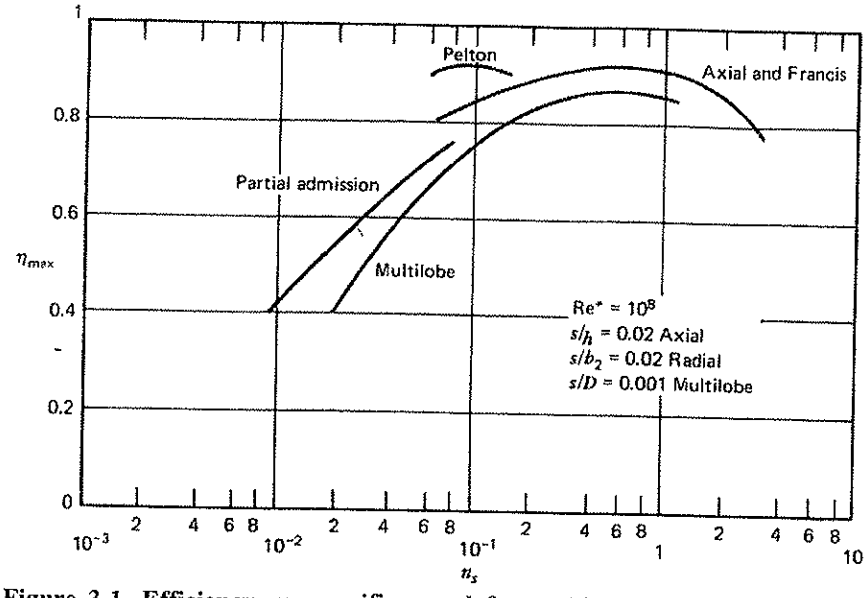

Figure 3-1. Efficiency vs. specific speed for turbines (Figure copied from Baljè (1981))

Figure 3-1 shows a correlation between specific speed and efficiency for various turbines. According to Baljè (1981), a radial turbine has the same optimal specific speed as Axial and Francis, but with a narrower speed range. As shown in the Figure, a Pelton turbine is a good choice with regards to minimizing the specific speed. A Pelton turbine is however most frequently used in water power production and high capacities. This work focuses on small capacities, and needs an expander that can handle two-phase flow. The work of Akagawa & Asano (1986) showed that a Pelton-type turbine is also applicable for two-phase flow. Especially at low vapour fractions.

Table 3-2 shows that the expected nozzle jet diameter is 1.17 mm. This is assumed to have equal gas and liquid velocity at least at the outlet. Design rules for water turbines from Brekke (1999) say that the Pitch Circle Diameter (PCD) of a Pelton turbine shall be 10-15 times the nozzle jet diameter, which implies PCD between 12 and 18 mm.

With nozzle jet velocity 133 m/s, a turbine with 15 mm PCD would rotate at 100 krpm. Using eq (2-30) and (2-31) gives specific speed $n_s = 0.13$ and specific diameter $d_s = 13$ for $H_{ad} = 1000$ m. $H_{ad} = 1000$ m corresponds to an enthalpy drop 9.81 kJ/kg, which is slightly higher than the enthalpy drop resulting from the design basis given in Table 3-1. According to Figure 3-1 this specific speed is ideal for a Pelton-turbine. Figure 3-2 also

shows that specific speed and specific diameter for the model turbine correspond well with optimal values for these parameters.

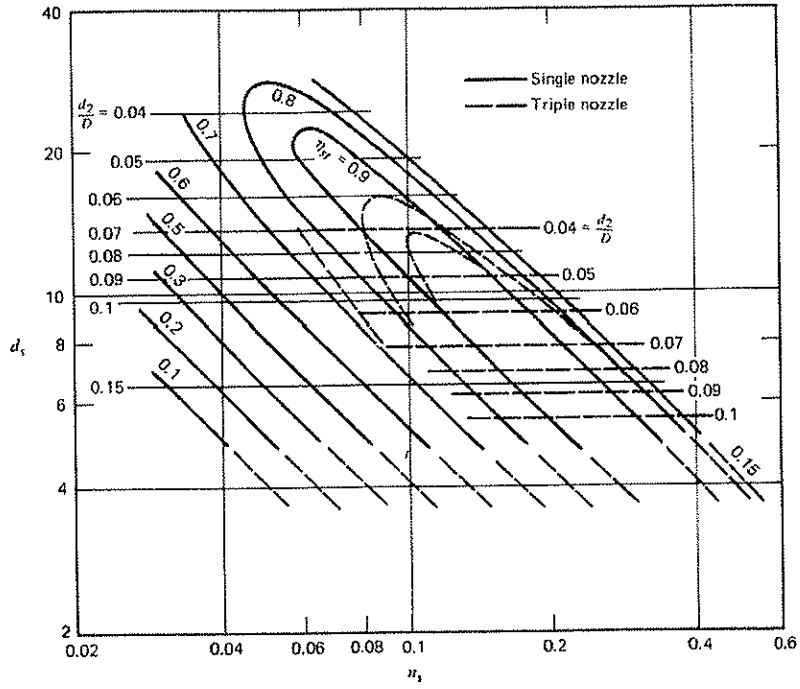

Figure 3-2. n_s-d_s diagram for Pelton turbine (Figure copied from Balje (1981))

A Pelton-turbine has a very special 3-dimensional bucket geometry that gives a high efficiency due to its ability to deflect the whole nozzle jet completely and because the nozzle jet always hits a bucket. A Pelton turbine with 15 mm PCD will be very difficult to manufacture correctly, so it is necessary to find a way to modify the details of the design without compromising the efficiency too much. If the pitch circle diameter was doubled, the dimensions would start to get into a range where it is economical to manufacture. This reduces the turbine speed by 50 %, but losses due to windage and disc friction would be increased by a factor 4 because these losses are $\sim\omega^3R^5$, where R is the rotor radius.

Figure 3-3 shows an n_s-d_s diagram for an axial impulse turbine. The diagram shows that the ideal axial impulse turbine has similarity parameters $n_s = 0.5$ and $d_s = 3.5$. For the actual process conditions shown in Table 3-1 this implies 400 krpm speed and 4 mm diameter. That would give challenges regarding manufacture of turbine and mechanical system.

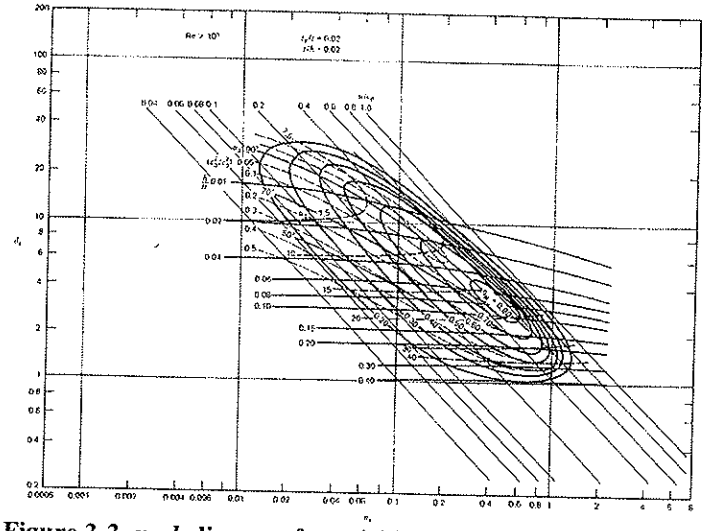

Figure 3-3. n_s-d_s diagram for axial impulse turbines (Figure copied from Balje (1981))

The chosen solution was to make an impulse turbine with roughly correct dimensions, but with a much simpler geometry in order to have a turbine wheel that was easy to manufacture. Among possible impulse turbines, a radial outflow impulse turbine was selected. The work principle of such a turbine was assumeded to be like half a Pelton turbine. And the model turbine was operated with use of one nozzle. The Pelton turbine cuts the jet and deflects, whereas the radial outflow turbine deflects the jet without cutting it. In the absence of specific design rules for this kind of turbine, the experimental turbine rotor had main dimensions as a Pelton turbine and the turbine blades were designed by use of velocity diagrams.

As the chosen turbine was a partial admission turbine, the capacity could be increased by adding extra nozzles. The fact that the experimental turbine was run with one active nozzle meant that the losses in bearings and losses due to windage and disc friction had high relative importance as compared to a full admission turbine.

3.3 Model expander dimensions

This chapter summarizes the calculation of the main dimensions for the expansion machine

3.3.1 Design of nozzle

At the nozzle inlet there will be supercritical CO_2, and at the outlet there will be two-phase CO_2. Before gas is formed, the nozzle is convergent, and the fluid flow velocity increases as the pressure decreases. When the formation of gas bubbles have started, the nozzle gets divergent, and the velocity continues to increase as the pressure decreases. This gives a convergent-divergent nozzle.

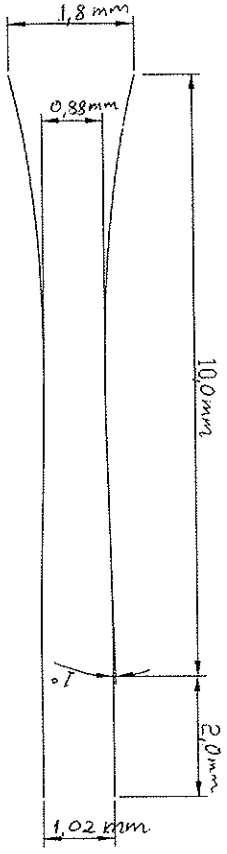

Figure 3-4. Nozzle geometry according to design

The ideal nozzle geometry is found by integration of Eq 2-12.

For design of the nozzle inner geometry, the data in Table 3-1 were used. Additional assumptions were

- Linear decrease in the pressure along the nozzle length
- 10 mm length was assumed to be enough for pressure reduction and flashing
- 2 mm straight section after the divergent part to possibly avoid conical outlet
- 100 % nozzle efficiency

The nozzle geometry calculated by this method was a convergent-divergent nozzle with curved walls, 0.88 mm throat diameter and 1.02 mm outlet diameter as shown in Figure 3-4. After manufacture of the first nozzle, the design method has been improved. The new method gives bigger dimensions. The original nozzle dimensions were however used in turbine and in nozzle characterization in order to have a consistent test schedule, and because project progress would make it difficult to go back and make the test program over again with an improved nozzle design.

shows that specific speed and specific diameter for the model turbine correspond well with optimal values for these parameters.

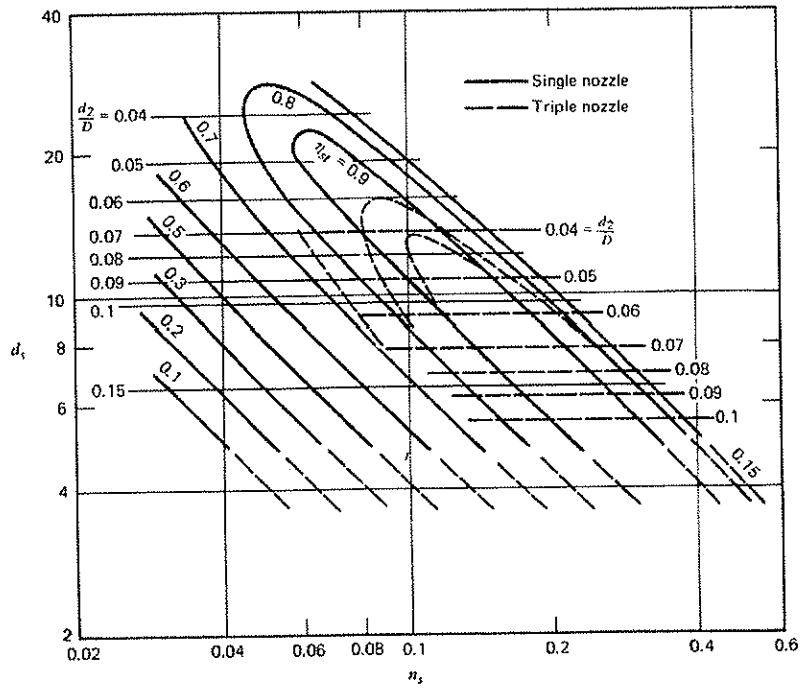

Figure 3-2. n_s-d_s diagram for Pelton turbine (Figure copied from Balje (1981))

A Pelton-turbine has a very special 3-dimensional bucket geometry that gives a high efficiency due to its ability to deflect the whole nozzle jet completely and because the nozzle jet always hits a bucket. A Pelton turbine with 15 mm PCD will be very difficult to manufacture correctly, so it is necessary to find a way to modify the details of the design without compromising the efficiency too much. If the pitch circle diameter was doubled, the dimensions would start to get into a range where it is economical to manufacture. This reduces the turbine speed by 50 %, but losses due to windage and disc friction would be increased by a factor 4 because these losses are $\sim\omega^3R^5$, where R is the rotor radius.

Figure 3-3 shows an n_s-d_s diagram for an axial impulse turbine. The diagram shows that the ideal axial impulse turbine has similarity parameters $n_s = 0.5$ and $d_s = 3.5$. For the actual process conditions shown in Table 3-1 this implies 400 krpm speed and 4 mm diameter. That would give challenges regarding manufacture of turbine and mechanical system.

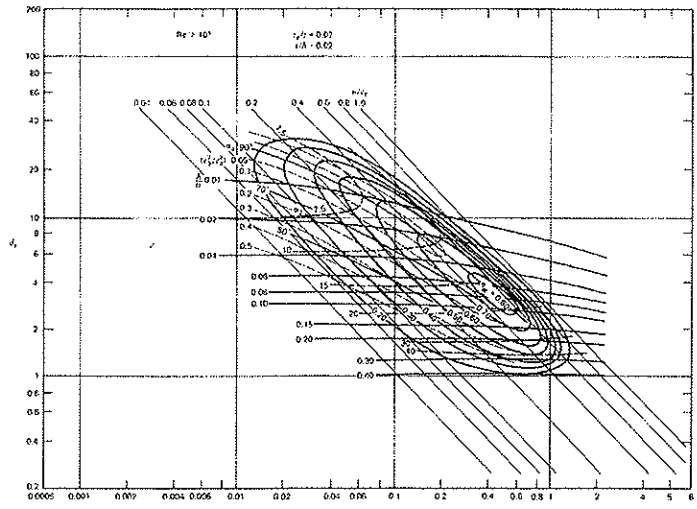

Figure 3-3. n_s-d_s diagram for axial impulse turbines (Figure copied from Balje (1981))

The chosen solution was to make an impulse turbine with roughly correct dimensions, but with a much simpler geometry in order to have a turbine wheel that was easy to manufacture. Among possible impulse turbines, a radial outflow impulse turbine was selected. The work principle of such a turbine was assumeded to be like half a Pelton turbine. And the model turbine was operated with use of one nozzle. The Pelton turbine cuts the jet and deflects, whereas the radial outflow turbine deflects the jet without cutting it. In the absence of specific design rules for this kind of turbine, the experimental turbine rotor had main dimensions as a Pelton turbine and the turbine blades were designed by use of velocity diagrams.

As the chosen turbine was a partial admission turbine, the capacity could be increased by adding extra nozzles. The fact that the experimental turbine was run with one active nozzle meant that the losses in bearings and losses due to windage and disc friction had high relative importance as compared to a full admission turbine.

3.3 Model expander dimensions

This chapter summarizes the calculation of the main dimensions for the expansion machine

3.3.1 Design of nozzle

At the nozzle inlet there will be supercritical CO_2, and at the outlet there will be two-phase CO_2. Before gas is formed, the nozzle is convergent, and the fluid flow velocity increases as the pressure decreases. When the formation of gas bubbles have started, the nozzle gets divergent, and the velocity continues to increase as the pressure decreases. This gives a convergent-divergent nozzle.

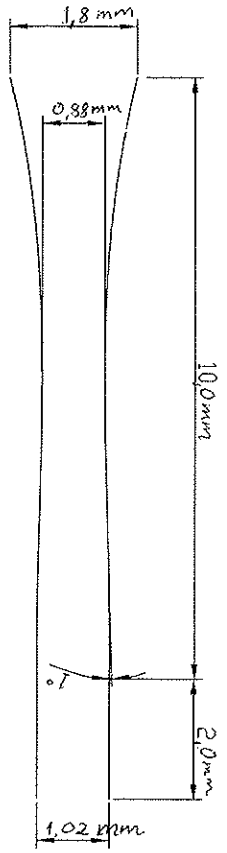

Figure 3-4. Nozzle geometry according to design

The ideal nozzle geometry is found by integration of Eq 2-12.

For design of the nozzle inner geometry, the data in Table 3-1 were used. Additional assumptions were

- Linear decrease in the pressure along the nozzle length
- 10 mm length was assumed to be enough for pressure reduction and flashing
- 2 mm straight section after the divergent part to possibly avoid conical outlet
- 100 % nozzle efficiency

The nozzle geometry calculated by this method was a convergent-divergent nozzle with curved walls, 0.88 mm throat diameter and 1.02 mm outlet diameter as shown in Figure 3-4. After manufacture of the first nozzle, the design method has been improved. The new method gives bigger dimensions. The original nozzle dimensions were however used in turbine and in nozzle characterization in order to have a consistent test schedule, and because project progress would make it difficult to go back and make the test program over again with an improved nozzle design.

3.3.2 Design of turbine rotor

A radial outflow impulse turbine was designed. In the absence of specific dimensioning rules for this kind of turbine, it was designed according to rules valid for Pelton turbines. The inlet and outlet angles of the turbine blades were designed by use of velocity diagrams. The turbine rotor geometry is shown in Figure 3-5. The line ED represents the nozzle jet, the line AB represents the tangent in the point where the nozzle jet hits the turbine wheel, and the line DC is parallel to the turbine blade profile, which means that it shows the direction of the inlet relative velocity. On the outlet, the direction of the relative velocity is shown by the line FG, and the vector C_2 shows the absolute velocity. Minimizing the angle α_1 gives a high efficiency, but as it also increases the angle λ, which in turn gives a lower efficiency.

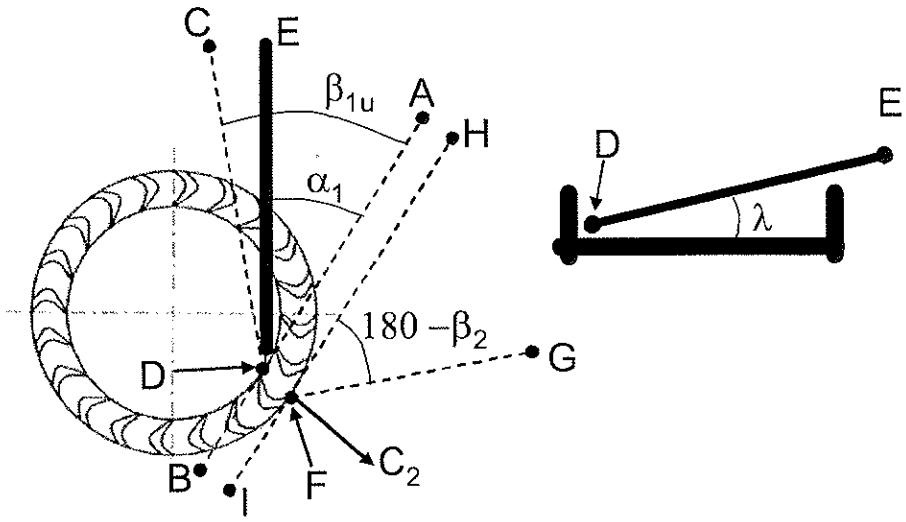

Figure 3-5. Turbine rotor geometry. Top view and side view.

Figure 3-6 shows two turbine blades for a radial outflow turbine. Such blades are placed along a circular disc. The nozzle jet is entering the blades at the diameter d_i and leaving the wheel at the diameter d_o. The inner diameter (d_i) corresponds to the turbine PCD (Pitch Circle Diameter), the height (h) corresponds to the length of a Pelton bucket's straight part, and the difference between the outer and the inner diameter corresponds to half the width of a Pelton bucket.

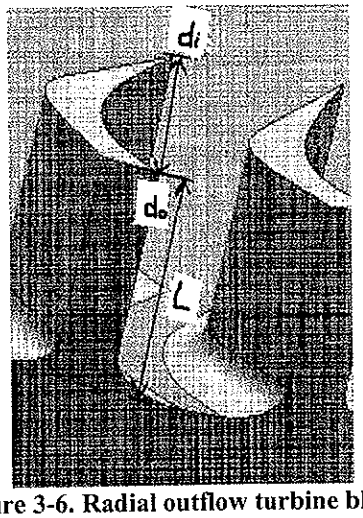

Figure 3-6. Radial outflow turbine blades

The corresponding dimensions and their values are shown in Table 3-3, where the dimensions of the radial outflow turbine refer to Figure 3-6. Turbines' design rules are based on experience. So are the rules used in this work.

Table 3-3. Principles for calculation of main dimensions

Pelton	Radial outflow	Value	Source
PCD	d_i	$10 \cdot d_{jet} - 15 \cdot d_{jet}$	Brekke (1999)
Bucket width	(d_o-d_i)	0.34 · PCD	Thake (2000)
Bucket length[1]	L	0.23 · PCD	Thake (2000)

1) Length of the bucket's straight part

The main dimensions of the turbine wheel for d_{jet} = 1.0 mm are given in Table 3-4. In order to make manufacture of the turbine rotor as easy as possible, the rotor diameter was made as big as possible without exceeding the recommended design. Hereby the turbine diameter was set to 15 mm.

Table 3-4. Main dimensions for the model expander turbine wheel

Dimension	Unit	Value
d_i	mm	15
d_o	mm	20
L	mm	3.5

Figure 3-7 shows the velocity triangles for the turbine wheel. Some decisions were made prior to the design:

- The nozzle angle α_1 was set to 35°. This made it possible to give the nozzle 0,2 mm clearance from the wheel and to have λ = 16°.

- The nozzle outlet velocity c_1 was chosen to 120 m/s. This corresponds to 80 % nozzle efficiency. According to the first tests, and preliminary analysis of the results, 80 % nozzle efficiency would be optimistic but achievable. If the nozzle jet velocity is reduced, all the other velocities are reduced correspondingly
- The outlet angle β_2 was set to 153°. A large β_2 leads to discharge CO_2 hitting the next bucket, whereas a small β_2 leads to a high discharge loss.
- Optimal inlet tip speed is 50 % of the projection of the nozzle jet speed in the direction of the tip speed. This is according to design principles for axial impulse turbines, as shown in Øverli (1992).

The diagram in Figure 3-7 results from these assumptions. From the figure, it can be seen that the optimal efficiency is achieved when β_2 is 180°. This would however give a situation where CO_2 leaving the wheel hits the back-side of the next turbine blade, which again lowers the turbine efficiency.

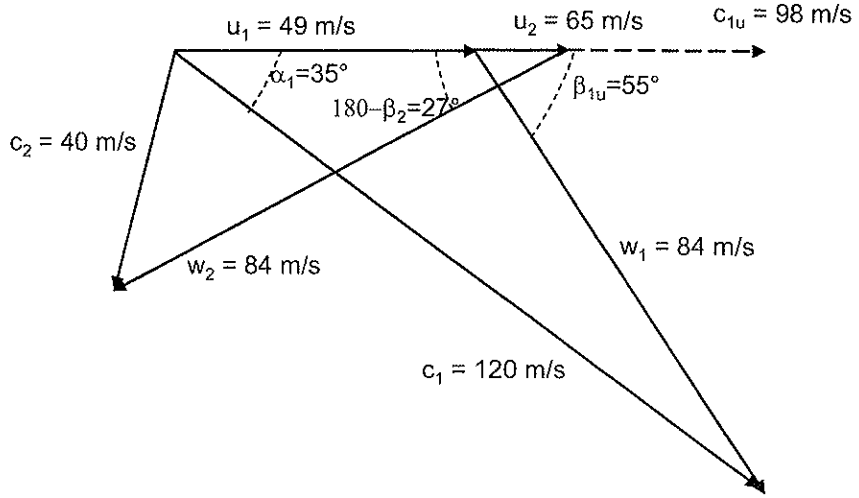

Figure 3-7. Velocity triangles for the turbine wheel

The turbine was modeled for manufacture by 5X Verkstedkompetanse AS in Trondheim, Norway. In connection with the modeling, strength computations were made for the wheel. The purpose of the strength calculations was

1) To check that the turbine blades could withstand the forces due to centrifugal acceleration at runaway, 135000 rpm.
2) To check the risk of fatigue due to the blades entering and leaving the nozzle jet.

The calculations showed that the strength of the wheel was adequate for the use.

The wheel was manufactured by spark erosion at Verkstedpartner AS in Trondheim, Norway. The rotor material was stainless steel. And the average surface roughness of the rotor blades was estimated to 2-3 μm by comparison with samples of known surface roughness.

As the turbine and its instrumentation will be in a pressurized chamber, there will be no need for a shaft seal to prevent leakages from the unit. This is a great advantage as a loss source is removed, and the complexity of the unit is reduced.

3.4 Utilization of the expansion work

This section discusses utilization of expansion work by using a compressor on the same shaft as the expander. For low-speed machines it would be possible to use the energy for all kinds of rotating equipment like fans, liquid pumps or a generator. With a high-speed machine, it would be possible to run a generator, but this causes great challenges, beyond the scope of this work.

For a compressor-expander solution there will be four possible configurations.

1. An expander-driven compressor compresses the gas delivered from the main compressor, which was the best solution according to Heyl (2001).
2. The expander-driven compressor compresses the gas before entering the main compressor, a solution for which the company Sanden has sent a patent application.
3. A part of the total CO_2 flow is compressed in the expander-driven compressor.
4. Main compressor on the same shaft as the expander, here there must be an electrical motor on the shaft as well. This solution was patented by Abdelmalek (1991)

Of these solutions, solution 2 is expected to be the easiest one to realize because the compressor inlet pressure is on the same level as the expander outlet pressure. This makes sealing between the compressor and the expander unnecessary.

Baljè (1962, Part B) gives data for designing compressors by use of specific speed and diameter at given conditions. The expander applied has a low specific speed, so the compressor must also have low specific speed.

Fig 6 in the article shows that the radial compressor requires lower specific speed than the axial. It also shows that the radial compressor efficiency is acceptable at specific speeds down to $n_S = 60$, whereas the model expander the specific speed has been estimated to $n_S = 10.5$. The model expander is however not the final model, so it will be wrong to test the match between the model expander speed and the compressor speed.

4 Experimental equipment

4.1 Test rig principles and design basis

The test rig was designed to not need oil for lubrication. This because oil can influence on the efficiency of process equipment used for conditioning of the CO_2 and because it may affect the operation of the expander tested in the facility. To increase the pressure before the expansion, a CO_2 lubricated pump is used. Because the test rig used a liquid pump, the vapour CO_2 formed in the expansion was condensed before entering the pump. This was done in glycol-cooled heat exchangers.

The test rig was built to have flexibility to test various types of expansion equipment. Here it was important to have a separate test section in the test rig, in order to avoid problems with test equipment requiring more space than available. As different types of expansion equipment require different instruments, the instrumentation of the test section must be done independently from the rest of the test rig.

The process conditions used for selection and design of equipment to be used in the test facility are given in Table 3-1. The nominal cooling capacity at design conditions was set to 10 kW.

At design of the test facility, some uncertainty calculations were made in order to identify instruments needing special attention because they would be contributing considerably to the total uncertainty in the measurements. The inlet and outlet temperatures for CO_2 and glycol were identified as critical measurements, together with the flow rates for CO_2 and glycol. For the temperatures, PT100 elements were used as they were expected to give an acceptable precision. For mass flow of CO_2 a coriolis-meter was selected, and the glycol volumetric flow rate was measured by an electromagnetic flow-meter. The glycol condition is interesting if a heat balance shall be made over the expander to control the measured expander effect. As the expander efficiency is still very low, that is not in question yet.

The temperature sensors were placed as close as possible to the expander in order to reduce heat losses before entering the nozzle. It is however not possible to measure the temperature directly at the nozzle entrance, so there would be around 0.2 m distance from temperature measurement to nozzle entrance. With 0.01 m outer diameter on the tubing, between the nozzle and the temperature transmitter, the surface area is 0.0063 m^2. With 25 K temperature difference and U = 10 W/(m^2K), the heat loss is

1.57 W. With 0.035 kg/s CO_2 mass flow, this would correspond to 45 J/kg lower inlet enthalpy. This again indicates 0.014 K lower inlet temperature, and it has minimal influence on the total uncertainty of the temperature measurement.

4.2 Laboratory test rig for expansion work recovery

4.2.1 Overview

The test rig contained 4 main parts:

- Refrigerant (CO_2) circuit,
- Test section,
- Heating circuit
- Cooling circuit

Figure 4-1 shows an overview of the test facility. Four points are marked with numbers:

- Test section inlet (1)
- Test section outlet (2)
- Sub-cooler outlet/pump inlet (3)
- Pump discharge (4)

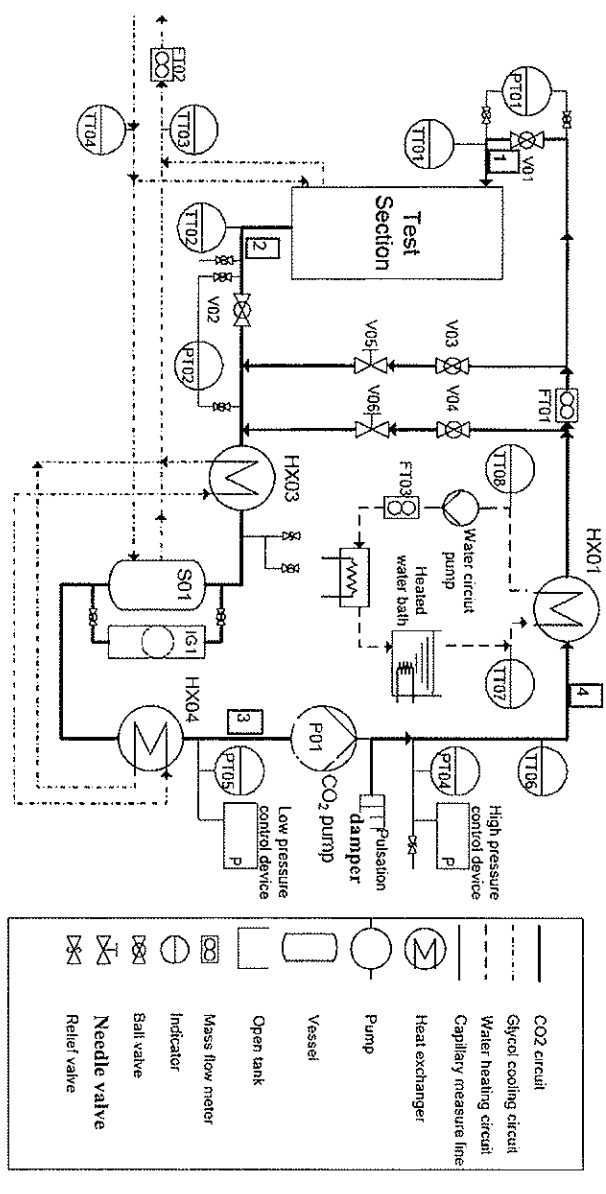

Figure 4-1. Flow chart for the expander test facility

In Figure 4-2 the theoretical CO_2-cycle of the expansion work recovery test rig is shown. The numbers on the Figure refers to the numbers given in Figure 4-1. The expansion between 1 and 2 reduces the enthalpy as work is extracted from the system. The best efficiency is achieved by isentropic expansion as shown in Figure 4-3.

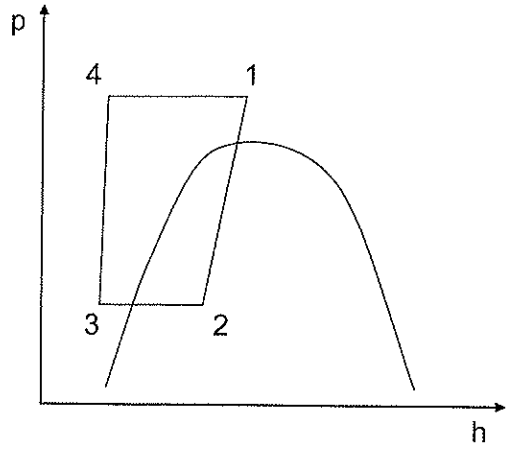

Figure 4-2. Theoretical CO2-cirquit of the test facility in a p,h-diagram

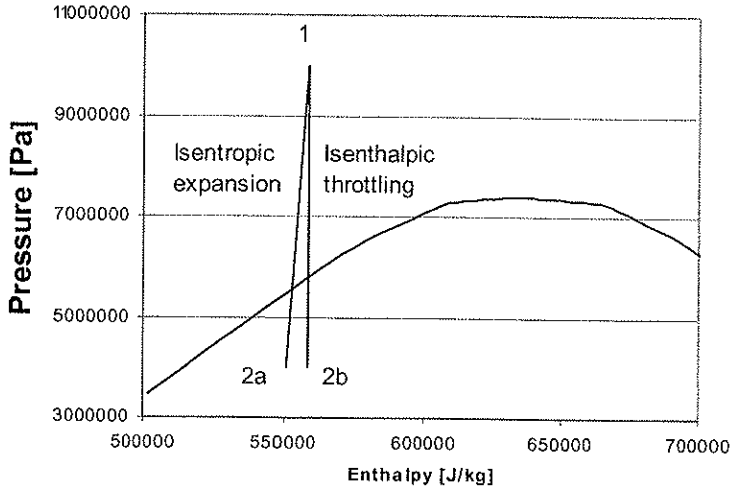

Figure 4-3. Comparison between throttling and isentropic expansion

4.2.2 Refrigerant (CO2) cycle

Liquid refrigerant CO_2 was pumped from low pressure to high pressure by a plunger pump (P01), and heated in HX01, which was connected to a heating system described in 4.2.3. Before the expansion from high pressure to low pressure (realized with an expansion machine in the test section), refrigerant flowed through a mass flow meter (FT01). The CO_2 vapour formed by the expansion was condensed in HX03, gas was separated from the liquid in the separator (S01) and the liquid was sub-cooled in order to avoid pump cavitation, in HX04.

4.2.3 Heating system

CO_2 was heat exchanged with water in a coaxial heat exchanger (HX01) to reach the desired expander inlet temperature. Water was heated by an immersion heater and a heated bath, and circulated by a Grundfos pump (Type UP 25-30N). The CO_2 temperature at the heat exchanger outlet was adjusted by regulating the amount of electric power in the immersion heater and the heated bath.

4.2.4 Cooling circuit

The glycol cooling circuit was included to remove heat from the CO_2 after the test section, so that a liquid pump could be used for pressure rise in the cirquit. The cooling system consisted of a condenser (HX03), a separator (S01) and a sub-cooler (HX04). Both heat exchangers were coaxial heat exchangers. After the sub-cooler, the CO2 entered the liquid pump.

Cool glycol was delivered from a separate glycol R-22 cooling unit. The glycol temperature was measured both on the inlet and outlet of the test facility, and before the temperature measurements there was a static mixer to ensure a homogeneous temperature in the pipe. The glycol ran in parallel through the heat exchangers in the test rig.

4.2.5 Expansion measurements' section

The test section was separated from the rest of the CO_2 circuit. It was used to test performance by expansion in nozzles and in a complete expander. By opening two ball valves and closing a bypass valve the section was opened to the circuit. The test section was only opened after the circuit had stabilized to the settings adjusted.

4.3 Test rig equipment

4.3.1 Refrigerant Pump

- Piston pump type 5CP215OBCO2 from CAT PUMPS (U.K.) LTD.
- Frequency converter for capacity control.
- Special seals for CO_2
- Lubricated by medium
- Maximum speed specified by the manufacturer to 1725 rpm.

4.3.2 Water Pump

- Centrifugal pump
- Grundfos, Type UP 25-30N
- Maximum capacity 37 liter per minute
- Maximum pressure differential 0,3 bar

4.3.3 Heat Exchanger

Principle:

The heat exchangers consisted of two stainless-steel tubes (tube-in-tube) as shown in Figure 4-4.
CO_2 flowed inside the inner tube with 10 mm OD and wall thickness of 1 mm. And glycol/water flowed on the outside. A copper thread was winded around the inner tube in order to assure good distribution of the glycol/water.

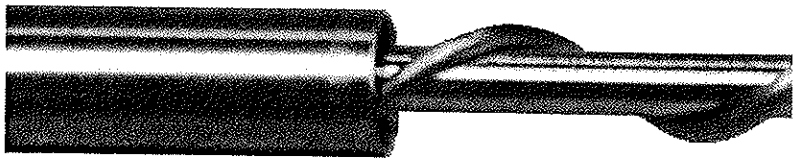

Figure 4-4. Structure of heat exchangers

Length of the heat exchanger (HX01) 4,1 m
Length of the condenser (HX03) 10,0 m
Length of the subcooler (HX04) 2,0 m

4.3.4 Electric Heater (heater with reservior)

- Name, typ, firm: / 01DT622-1/1 / Heto
- Range: 220 V / 1040 Watt

4.4 Test rig Instrumentation

4.4.1 Temperature (Thermocoax)

- Measurement principle: thermocoax
- Type: Thermocouple Type T
- Range: -100 to 400 °C
- Uncertainity: ± 0.1 K
- Output signal: mV

4.4.2 Temperature (PT100)

- Measurement principle: PT100
- Type: RTD type 85
- Range: -200 to 350 °C
- Uncertainity: ± 50 mK
- Output signal: mV

4.4.3 Pressure

- Method: Digital pressure transmitter with polysilicon sensors
- Type: Model CERAGAR S PMP 731
- Firm: Endress & Hauser
- Range: 0 to 100 bar (PT02/PT03 were adjusted to 0 to 50 bar)
- Uncertainity: ± 0.1 % of calibrated span
- Output signal: 4-20 mA
- All cells were equipped with display unit

4.4.4 Flow rates for water/glycol/CO2

Water volumetric flow

- Method: Turbine flow meter
- Name, type, Firm: FT-16W50-LB from FTI
- Signal converter: PRC-408 from FTI
- Range: 0-94.6 l/min
- Uncertainity: ± 0.5 % of reading
- Output signal: mV

CO2 mass flow

- Method: Coriolis
- Name, type, Firm: RHM 03/GET2 from Rheonik
- Signal converter: RHE 08 from Rheonik
- Range: 0.05-5 kg/min
- Uncertainity: ± 0.1 % of reading
- Output signal: mA

Glycol volumetric flow

- Method: Electromagnetic flowmeter
- Name, type, Firm: Model DM41F from Bailey Fisher & Porter
- Signal converter: Model 50XM2000
- Range: 0.25-45 l/min
- Uncertainity: ± 0.4 % of reading
- Output signal: mA

4.4.5 Data logging

The instruments/signal converters were connected to an Agilent 34970 A Data Aquistition/Switch Unit for data logging, and for monitoring of the data on a PC. The PC had a Pentium II processor, 128 MB ram and Windows 98 SE as operative system.

Digitalisation of signals in the data logger introduced an uncertainty. For the different types of signals, this uncertainty is shown in Table 4-1.

For every channel, NPLC (Number of Power Line Cycles) was set to 10, which means that each channel was scanned 10 times, and the mean value of these scans was displayed on the monitor and saved to the log file.

Table 4-1. Uncertainties in datalogger from various transmitters

Signal transmitter	Uncertainty
Thermocouple Type T	± 1.0 K
RTD (PT100)	± 60 mK
Digital pressure transmitter	± (0.0040 % reading + 0.0007 % range)
Flow measurement, CO_2	± (0.0040 % reading + 0.0007 % range)
Flow measurement, Glycol	± (0.0040 % reading + 0.0007 % range)
Flow measurement, Water	± (0.0040 % reading + 0.0007 % range)
Hall sensor signals	± (0.0035 % reading + 0.0005 % range)
Torque transmitter	± (0.0040 % reading + 0.0007 % range)

The uncertainty in the Thermocouple Type T is so high because an internal zero-point was used for this instrument.

4.4.6 Summary of instrumentation

In Table 4-2 the instruments and their uncertainties are summarized. It is important to note that these uncertainties come from the instruments, whereas the uncertainties in Table 4-1 have their origin in the digitalization in the datalogger.

Table 4-2. Summary of the instruments, their range and uncertainty

Lab. No.	Type	Tag	Range ± Uncertainty	Unit
KN08-0082	Digital Pressure transmitter	PT04	0.5-100 ± 0.1 % of span	bara
KN08-0083	Digital Pressure transmitter	PT01	0.5-100 ± 0.1 % of span	bara
KN08-0084	Digital Pressure transmitter	PT03	0.5-50 ± 0.1 % of span	bara
KN08-0085	Digital Pressure transmitter	PT02	0.5-50 ± 0.1 % of span	bara
KN04-0061	Mass flowmeter Coriolis	FT01	0.1-5.0 ± 0.1 %	kg/min
KN11-0046	Turbin meter, liquid	FT03	0-94.6 ± 0.5 %	l/min
KN11-0048	Flowmeter, electromagnetic	FT02	0.25-45.0 ± 0.4 %	l/min
Teck Instrument	Temperature transmitter, PT100	TT01	-200 – 350 ± 0.05 K	°C
Teck Instrument	Temperature transmitter, PT100	TT02	-200 – 350 ± 0.05 K	°C
Teck Instrument	Temperature transmitter, PT100	TT03	-200 – 350 ± 0.05 K	°C
Teck Instrument	Temperature transmitter, PT100	TT04	-200 – 350 ± 0.05 K	°C
Teck Instrument	Temperature transmitter, PT100	TT05	-200 – 350 ± 0.05 K	°C
	Thermocouple	TT06	-100 – 400 ± 0.1 K	°C
	Thermocouple	TT07	-100 – 400 ± 0.1 K	°C
	Thermocouple	TT08	-100 – 400 ± 0.1 K	°C
	Hall sensor signals		0.000 – 10 .000 ± 0.002	V
	Torque transmitter		0-0.07 ± 0.1 % of span	Nm

For the most interesting measurements the data in Table 4-1 and Table 4-2 give a maximal total uncertainty as given in Table 4-3, when the process

data are as the design basis in Table 3-1 and the hall sensor signal shows 10 V, while the measured torque is 0.07 Nm.

Table 4-3. Maximal total uncertainty for the most interresting signals

Signal	Value	Unit	Total uncertainty
PT01	100.0	bar	0.10
TT01	30.00	°C	0.08
TT02	5.00	°C	0.08
FT01	0.05000	kg/s	0.00005
Hall sensor	10.000	V	0.002
Torque	0.07000	Nm	0.00007

5 Experimental program, methods and data processing

This chapter contains the following sections

- Process conditions for the experiments and the reason for the choices of process conditions
- Nozzle testing equipment and methods are given detailed description
- Expander testing equipment and methods are given detailed description
- Test procedure is described briefly
- Data processing and calculations

5.1 Background, ambitions and goals

The experimental program was set up in order to characterize the performance of the expander and its individual parts, and hereby gain knowledge about losses in the expansion process. Losses in the nozzle of an impulse expander limit the total efficiency of the expander. Therefore the nozzles were tested separately before testing the complete expander. The nozzle test program was set up in order to test the nozzle at various process conditions relevant for the expansion process. Nozzles of various inner geometries and various grades of inner surface treatment were tested. In nozzle testing the following methods were used:

- Reactive power measurement to check the performance and efficiency
- Flow visualization to check the jet shape

The expander tests were made to check the performance of the complete expander at various process conditions, and to gain insight in the loss processes of the current expander. The following methods were used

- Blocked shaft measurements
- Torque and speed measurement with vacuum in the chamber
- Torque and speed measurement process pressure in the chamber
- Runaway tests
- Testing turbine with brake

5.2 Choice of process conditions in experiments

The process conditions for the nozzle testing and expander testing experiments were chosen so that they were relevant to the conditions for an expander in operation in a real refrigeration process, for instance in mobile air conditioning.

For mobile air conditioning an evaporator temperature in the interval 0-10°C was considered to be relevant. This corresponds to a nozzle- or expander outlet pressure of 35-45 bar. The relevant interval for the gas-cooler outlet (nozzle/expander inlet) temperature is considered to be 25-45°C, which corresponds to a gas-cooler pressure in the interval 75-105 bar. Because the nozzles have a fixed geometry, the CO_2 mass flow was used to adjust the expander inlet pressure to the desired value.

Experiments were made with combinations of the following nominal conditions

- Outlet pressure: 35 bar, 40 bar and 45 bar
- Inlet temperature: 25°C, 30°C, 35°C
- Inlet pressure: Below optimal, optimal and above optimal. For optimal pressure it is referred to Eq (2-4)

A full run would require 27 different experiments. Some combinations were however impossible to achieve with the available equipment.

5.3 Nozzle performance characterization

The equipment for nozzle performance characterization was built for use of two methods

- Reactive power measurements
- Nozzle jet flow visualization

Reactive power measurements were used to measure the nozzle jet velocity, and hereby the nozzle efficiency. This is a simple method, and it reduces the need for advanced experimental equipment. A disadvantage with the method is that the average nozzle jet velocity is measured, so no information about the phase velocities is gained.

Flow visualization was used to investigate the conditions at the nozzle outlet. The parameters of interest were in this case how concentrated the jet was, and secondary flow conditions. For extraction of work from a nozzle jet, it is a clear advantage to have a concentrated nozzle jet. And the secondary flow conditions will influence on the expander losses.

For all the nozzle characterisation tests, the experiments were run at stable conditions for 10 minutes. With data sampling every 10^{th} second, there were 60 observations behind every data point for these tests. With stable conditions, it is meant that the inlet glycol temperature shoed little variation, $\pm$ 0.1 K over the experiment. If the variation was higher, this made the rest of the temperatures unstable, and the experimental uncertainty became too high.

5.3.1 Equipment for nozzle performance characterisation

The nozzle test section contained

- A cylindrical metering chamber
- A force transducer
- An inspection glass
- A chilled expansion vessel

The components were joined together as shown in Figure 5-1.

High pressure CO_2 entered at pos 1, and then it proceeded through a flexible hose that ended in a u-bend, and then a pipe union elbow pointing downwards in pos 2. The elbow is in contact with a force transducer that was used for measurement of the nozzle reactive power. From pos 2, the CO2 proceeds through steel piping of OD 10 mm. At the end of the 10 mm piping, at pos 3, the nozzle hung. In the joints between the chamber

outflow and the inspection glass inlet, two linear ball bearings Type KH 1026 were mounted to assure free and absolute axial movement against the force transducer.

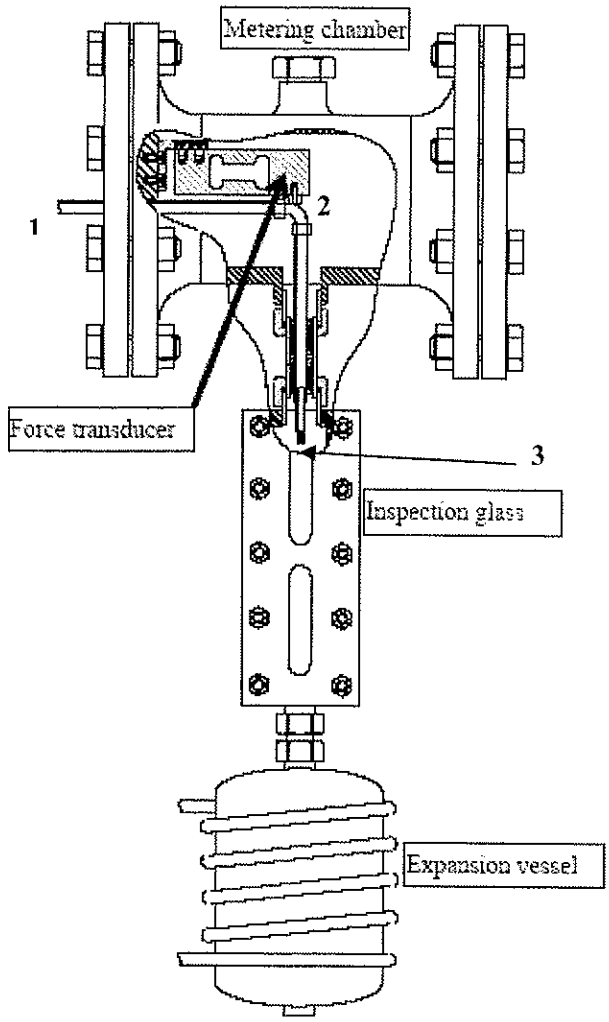

Figure 5-1. Equipment for nozzle performance characterisation

The metering chamber

The metering chamber was made of a steel tube of 130 mm length and a diameter of 155 mm. In the middle two sleeves of 33,6 mm diameter were welded on the outside tube shifted at 180 degrees. Each had a female screw thread sized ¾ in. At each end of the tube a weld neck flange DIN 2632 was welded on. The chamber was sealed by two flanges (DIN 2527). One flange had two lead-in sleeves, one for the CO_2 tubing and the second

for the connection cables to the force transducer. The force transducer was fixed on the inside surface of this flange by a mounting bracket. The other flange was used as a service hatch.

The force transducer

The force transducer was an aluminium single point load cell. It was moment insensitive and had measure platform size of 400 x 400 mm. The load capacity was 5 kg, with ± 0.001 kg uncertainty in the reading. The CO_2 pipe was connected to the load cell with a plastic strip, thus a negative value was shown on the display of the measure display. The connection cables of the load cell lead outside of the metering chamber to the display for the signals from the load cell. In this case the signal was shown as weight in kilograms.

The inspection glass

The inspection glass was made out of borosilicate glass, DIN 7081. It was 220 mm long and was especially installed be able to visualize flow conditions around the nozzle exit. The use of two glasses allowed viewing the nozzle from a front and a rear view. The glass holder cage was also made of stainless steel an had a length of 28 mm. On both ends of the cage ½" female threads, containing thread nipples, connected the gauge glass to the nozzle holder track on the upper side and an expansion vessel on the lower exit.

After the inspection glass, the pipe lead directly to second ball valve (V02) of the test section.

5.3.2 Nozzle properties

Table 5-1 gives the properties of the nozzles tested. As can be seen, two different geometries were tested, and both of them were tested before and after surface treatment by Extrude-hone.

Table 5-1. Properties of the nozzles tested

Nozzle	Shape	Length	Smallest diameter	Surface treatment	Surface roughness
		[mm]	[mm]		[μm]
N1	Straight bore	20	1.0	No	6.0
N2	Straight bore	20	1.0	Extrude-hone	1.0
N3	Convergent-divergent	21	0.88	No	6.0
N4	Convergent-divergent	21	0.88	Extrude-hone	1.0

For the nozzles tested, the following friction factors apply. The fanning friction factors were taken from Geankoplis (1993).

Table 5-2. Convergent-divergent nozzle, average roughness 6.0 μm , $Re>10^5$

d [mm]	1.80	1.34	0.88	1.02
Relative roughness	0.0033	0.0045	0.0068	0.0059
Fanning friction factor	0.0065	0.0080	0.0085	0.0080

Table 5-3. Convergent-divergent nozzle, average roughness 1.0 μm , $Re>10^5$

d [mm]	1.80	1.34	0.88	1.02
Relative roughness	0.0006	0.0008	0.0011	0.0098
Fanning friction factor	0.0045	0.0045	0.0045	0.0045

A drawing of the convergent-divergent nozzle tested is shown in Figure 5-2. The nozzle was manufactured by Günther Frey GmbH & CO KG in Berlin, Germany.

The convergent-divergent geometry is expected to be the ideal geometry for a nozzle with flashing flow. Before the flashing starts, the fluid is in the convergent part. Here the pressure is reduced by increasing the flow velocity. In the divergent part, the fluid is flashing. The increase in flow cross section allows for the increase in specific volume that takes place in

flashing flow. The nozzle with a straight bore was tested because a simple geometry will be desirable for further use of the technology, and a convergent-divergent nozzle is expected to be difficult to manufacture economically in the correct dimensions.

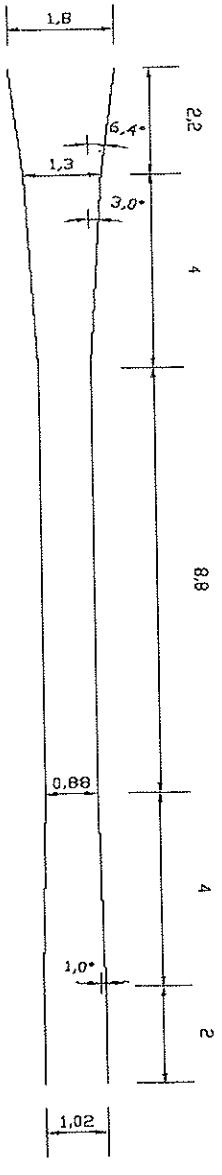

Figure 5-2.
Convergent-divergent nozzle for testing

The surface roughness on the nozzle inside is important for friction losses and nucleation in the flow. Therefore nozzles with and without polished passages inside have been tested in order to see the impact of the friction losses. The method for drilling the passage of the convergent-divergent nozzle gave, according to the supplier, an average surface roughness lower than 6.0 μm, and the use of extrude-hone was expected to decrease the roughness by a factor 5 to 10, that means, the polished nozzle would have an average surface roughness around 1.0 μm. The properties of the nozzles are shown in Table 5-1.

5.3.3 Nozzle inlet

The effect of using a multiple-hole orifice plate on the nozzle inlet was tested for the convergent-divergent nozzle. According to Brasz (1995) the plate was crucial for the opportunity of getting a homogeneous nozzle jet, as the use of this plate would initiate the formation of a large number of small flashing vapour bubbles. The plate was produced by Günther Frey Precision GmbH in Berlin, Germany. The geometry of the distribution plate is shown in Figure 5-3.

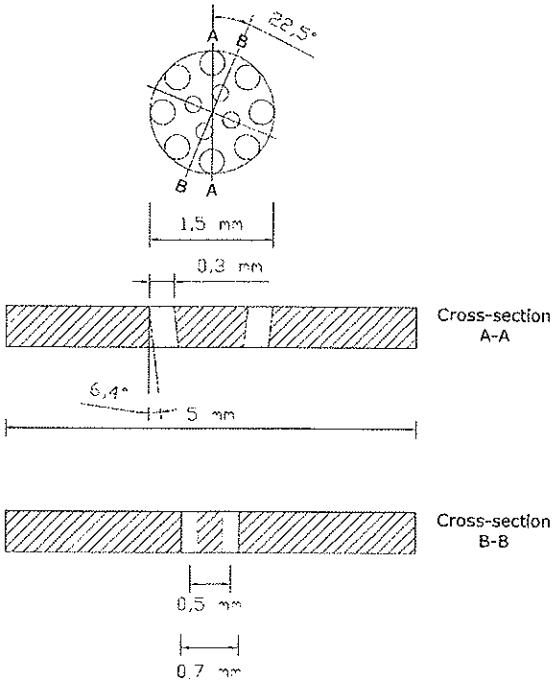

Figure 5-3: Distribution plate on nozzle inlet

5.4 Expander test methods and equipment

The objective of the expander tests was to gain insight in the function principles of the chosen machine, and hereby characterize the loss mechanisms. The nozzle was investigated individually, so the expander tests were made to gain insight in the processes appearing downstream of the nozzle outlet. The expander tests contained four components; blocked shaft testing, bearing loss characterisation, rotational loss characterisation and expander performance tests.

Blocked shaft testing

The blocked shaft tests were made in order to measure the losses on a non-rotating turbine, such as losses due to friction and losses due to jet not hitting the turbine blade.

For the tests with blocked shaft, the uncertainties and mean values are calculated using series of length 100 s because of instability in the process conditions. With sampling every 10^{th} second, this means that there are 10 samples behind every point.

Bearing loss characterisation

The bearing losses were measured by measuring the brake-motor shaft torque at various rotational speeds with vacuum in the expansion chamber.

Rotational loss characterisation

The rotational losses occur due to rotation of the expander wheel, shaft and motor-rotor in the atmosphere of pressurized CO_2. Characterisation of this loss was made by measurement of the brake-motor shaft torque at various rotational speeds and at various chamber pressures. The shaft torque due to bearing friction must be subtracted from the measured values in order to find the rotational losses.

Expander performance tests

In addition to the expander power measurements, the expander outlet enthalpy was measured by a heat balance over the cooling system downstream of the expander. With the expander outlet enthalpy, the internal efficiency of the expander can be calculated, and hereby it is possible to control the other measurements.

5.4.1 Expander test setup

The expander test unit as shown in Figure 5-4 was designed to measure expander speed and shaft torque. As a rotating torque measurement for the desired speeds would be very expensive, the torque was measured by a static torque transducer connected to the chamber wall and to the static part of the brake motor (pos 27). The torque measured is then the reaction torque between the stator and the torque transducer. According to Websters (1999), this torque is equal to the expander shaft torque minus parasitic torques related to losses e.g. in bearings and motor under equilibrium conditions.

Table 5-4. Most important positions on Figure 5-4

Pos	Description
1	Outer tube
2	End flange
3	Front bearing plate
4	Rear bearing plate
5	Torque transducer housing
6	Torque transducer plate
13	Shaft
14	Stator Cooling body basis
17	Spring ring
18	Nozzle holder
24	High speed bearing
25	Bearing (stator)
26	Labyrinth seal
27	Motor
28	Torque transmitter
37	Torque transmitting rods

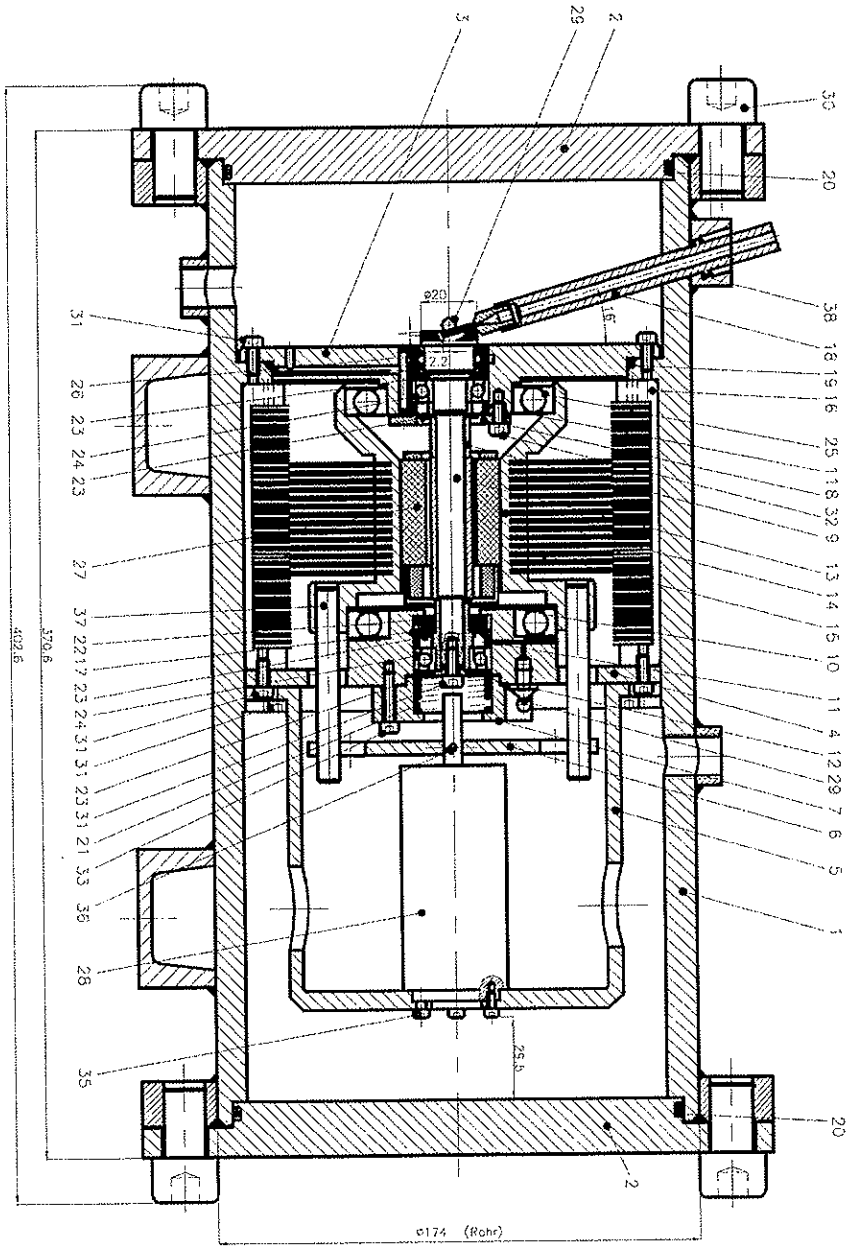

Figure 5-4. Expander test section

The most important positions of Figure 5-4 are described in Table 5-4.

The nozzle was placed at the end of the nozzle carrier (Pos 18) and spraed two-phase CO_2 directly into the turbine wheel. The turbine shaft (Pos 13) went backwards from the turbine wheel, and on this shaft the rotor magnets of the brake motor were placed. On both sides of the rotor magnets there were high-speed ball bearings, and between the turbine wheel and the first bearing there was a non-contact seal to protect the bearings from liquid CO_2. The stator of the brake motor was equipped with cooling ribs to allow for transport of excess heat from the brake motor. The stator was also equipped with bearings on both sides. The stator was connected via two rods (Pos 37) and a plate (Pos 6) to a torque transmitter (Pos 28), which was placed symmetrically to the motor, for static torque measurement. The torque transmitter was connected to the chamber outside-wall.

The motor and its control system was delivered from Maccon GmbH in Munich, Germany. The system consisted of the following components:

- Motor-kit BH02301-XOX, with hall sensors and temperature sensor
- Controller SWM300-12-R-CT
- SWM Testbox
- Powersupply PS-ET-050-150
- Surge diverter

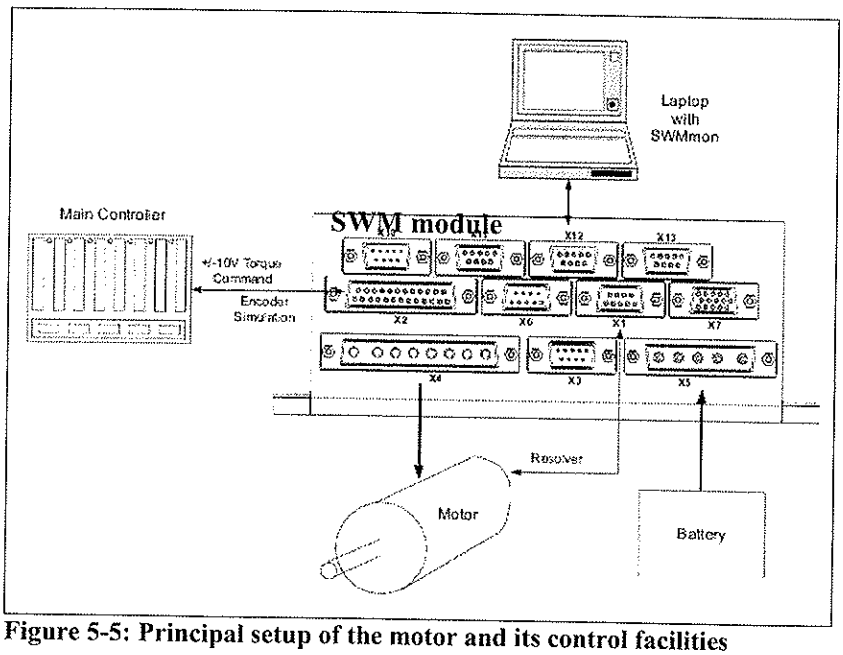

Figure 5-5: Principal setup of the motor and its control facilities

The principal setup of the motor and its control facilities is shown in Figure 5-5. The motor cables are connected to the SWM (Sine-Wave Servo module). From the motor to the SWM, electrical current is exchanged, and signals for the temperature measurement in the stator, as well as the hall sensor signal for monitoring of the motor speed.

The SWM is also connected to a power-supply called "battery" in Figure 5-5. When the motor is used to drive the turbine, electrical current is delivered from the power supply. When the motor is used for regeneration, the produced electrical current is dissipated in a surge diverter connected to the power supply.

The SWM test-box called "Main controller" in Figure 5-5 can be used to drive the motor manually, using a ± 10 V signal. And it can be used for encoder simulation in connection with optimization of the motor controller.

The motor can also be controlled via a PC with SWMmon software installed. The software SWMmon is also used for monitoring of the operational conditions for the motor, and for setting all parameters necessary for running the motor.

S. Himmelstein & Co. in Illinois, USA delivered the RTM1810S (1-1) Precision Reaction Torquemeter (Serial number 1810-4448), modified for operation at 60 bar:

- Range: 0.00-0.07 Nm
- Uncertainty: ± 0.1 % of full scale.
- Display unit: Model 708 Strain Gage Conditioner

5.4.2 Turbine configuration

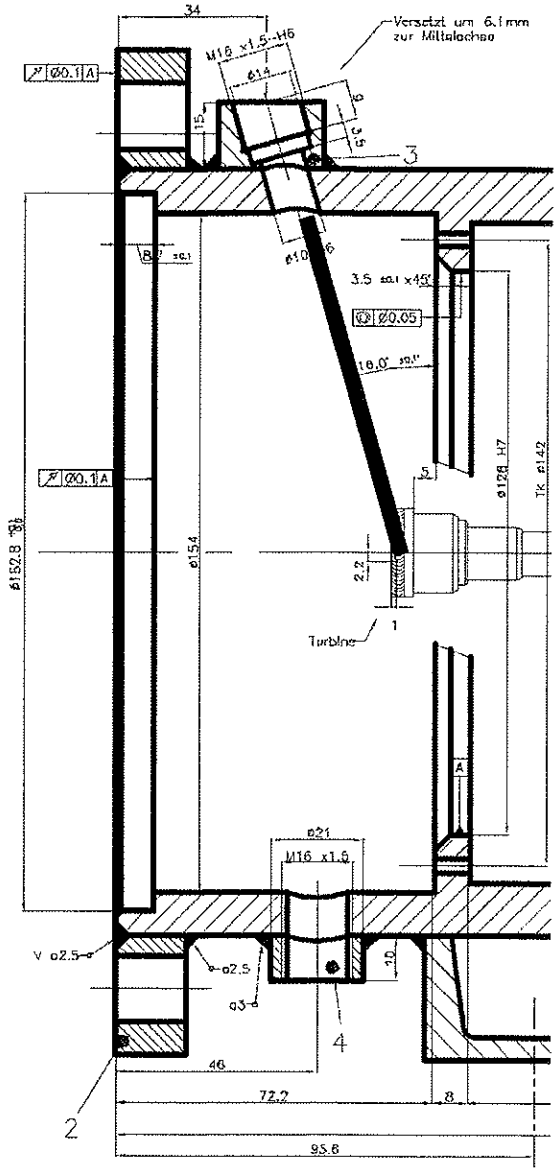

Figure 5-6. Turbine chamber

The key components of the turbine were the turbine wheel, the nozzle and the turbine chamber.

Figure 5-6 shows that the turbine chamber had around 154 mm diameter and 64 mm depth. With such dimensions the influence from the housing on the turbine performance was expected to be limited. The turbine

chamber had CO_2 outlet in the bottom (pos 4), and from here CO_2 gas and liquid entered the test rig condenser (HX03, ref Figure 4-1). After being deflected in the turbine wheel, the fluid was discharged at the wheel periphery.

The nozzle approached the turbine wheel from above. The nozzle holder enters the chamber through the connection (pos 3), and it approached the turbine rotor as indicated by the thick, black line. The nozzle internal geometry was convergent-divergent as shown in Figure 5-2. The nozzle used in the test turbine was not polished, and it did not include a distribution plate on the inlet.

5.5 Test procedure

The experiments were conducted by the following actions

General

1. Start the separate cooling circuit by starting the internal and the external pump, and then turning on the liquid valve.
2. Adjust the glycol outlet temperature from the separate glycol unit. To stabilise the glycol temperature may take some hours.
3. Start the CO_2 pump in the test facility, by-passing the test section.
4. Start the CO_2 heating to reach the desired inlet temperature.
5. Wait until the process conditions are stable.
6. Pay attention to the CO_2 level in the sight glass, so that the pump never runs dry. If the level gets too low, supply with extra CO_2.

A. For nozzle tests

1. Equalize the pressure in the nozzle outlet chamber and the rest of the low-pressure side of the test facility.
2. Write down the value of the force measurement before CO_2 is circulated through the nozzle.
3. Open the outlet valve from the nozzle chamber.
4. Open the nozzle inlet valve.
5. Close the by-pass valve.
6. Stabilise the process conditions
7. Select storage file-name and start logging
8. Log the process conditions for 10 minutes and observe the force measurement
9. Write down the process conditions and the force measurement after 9,5 minutes
10. Stop logging
11. Close the nozzle and open the by-pass

B. For expander tests

1. Equalize the pressure in the turbine chamber and the rest of the low-pressure side of the test facility.
2. Open the turbine outlet valve
3. Open the turbine inlet valve
4. Close the by-pass valve gradually
5. Stabilise the process conditions
6. Log the process conditions for 10 min.

Stop logging, open the by-pass valve and close the turbine inlet and outlet valves

5.6 Calibration and quality assurance

5.6.1 Load cell

The load cell was calibrated by the factory. Compared to the uncertainty in no-load value, the instrument uncertainty for the load cell was however negligible.

After maintenance or modifications, when the load cell was mounted and before the pressure chamber was shut off by the end flange, the following was checked on the load cell and nozzle testing system

- Stable no-load value (zero point)
- Correct measurement, little friction in linear ball bearings
- Free axial movement of the nozzle

If during testing new friction forces occurred e.g. in the linear ball bearings, the experiment was discharged and the test setup was modified until absolute axial movement of the nozzle tubing was assured.

After changes in the position of the flexible hose, tension forces in the flexible hose were measured for various internal pressures in the hose.

Correction of the data because of

- Chamber temperature
- Mass of CO_2 in the piping upstream of nozzle
- Tensions in the flexible hose

The zero-point measured when there was no flow through the nozzle was checked before every experiment. The zero points showed correlation with the chamber pressure, but with high grade of scattering that it was impossible to explain. The reason for differences in starting point might be tensions in the flexible hose, but as clear correlations were found except from the chamber pressure correlation. The start point was correlated to the chamber pressure by a regression analysis made in MS Excel. From this analysis the uncertainty in the nozzle zero-point was retrieved. Details are shown in Appendix 1.

5.6.2 Torque meter

The torque meter was factory calibrated before delivery.

Before blocked shaft tests, the torque meter was checked against known torques produced by weights of known mass. Check that the measured torque returned to the starting point after being exposed to a load.

In tests with rotating turbine, the zero point was logged. Cables from the stator caused a small, extra torque. By assembly it was paid much attention to preventing the cables from causing high torques, by keeping the cables as straight as possible. The bearings used for the stator (Figure 5-4, pos 25) were also carefully kept clean and lubricated by very thin oil in order to reduce the bearings' friction as much as possible.

5.6.3 Other instruments

Pressure transmitters were calibrated at the factory before delivery.

Temperature transmitters (PT100) were calibrated at the Institute.

Rheonik mass-flow meter was calibrated at the factory before delivery

5.7 Data processing

This chapter presents the methods used for analysis of the experimental data in order to

- Estimate turbine losses and identify the reasons why the losses occurred
- Estimate the efficiencies of the individual parts
- Estimate the efficiencies of the complete turbine

For processing of experimental data, the state functions and other physical properties of CO_2 were calculated by the in-house facility Rn-lib, where the CO_2 data are based on Angus et. Al (1976), Fenghour et. Al. (1998), Pitzer & Schreiber (1988) and Vesovic et. al (1990).

The corresponding uncertainty calculations for measured and estimated values are presented in Appendix 1.

5.7.1 Nozzle jet velocity, efficiency and outlet state

For an impulse turbine, where the pressure energy is converted to velocity in a nozzle, and then work is extracted from the nozzle jet in a turbine runner wheel, the nozzle efficiency determines the potential for further conversion of energy into work. The average nozzle velocity can be measured via the nozzle reactive power, which arises because of the difference between the outlet jet velocity and the inlet flow velocity.

$$F = \dot{m} \cdot (c_1 - c_0) \tag{5-1}$$

Assuming that c_0 is negligible ($c_0 \approx 0$) compared to c_1, and reorganizing, we get

$$c_1 = \frac{F}{\dot{m}} \tag{5-2}$$

With equation (5-7) it is possible to calculate the outlet jet velocity. For this, the following instruments are necessary

- FT01 for CO_2 mass flow
- Weight sensor for reactive power measurement
- TT01 and PT01 for CO_2 inlet conditions

The isentropic nozzle efficiency is shown in Eq (2-32). The mass flow of CO_2 is contained both in the numerator and the denominator, so the quotient between the squared nozzle jet velocity and the squared isentropic nozzle jet velocity must be evaluated. The isentropic nozzle jet velocity is shown in Eq 2-6. Hereby the isentropic nozzle efficiency is

$$\eta = \frac{c_1^2}{-2 \cdot \Delta h_s} = \frac{c_1^2}{-2 \cdot \left(h_{out}(s_{in}, p) - h_{in}(p,T)\right)} \quad \textbf{(5-3)}$$

The following measurements are needed to find the nozzle efficiency

- FT01 for CO_2 mass flow
- PT01 and TT01 for inlet conditions
- PT02 for nozzle outlet pressure
- Nozzle jet velocity

The nozzle jet specific volume at the nozzle exit was calculated by use of the law of mass conservation

$$\dot{m} = \frac{c_1 \cdot A}{v_1} = \frac{c_1 \cdot \left(\frac{\pi}{4} d^2\right)}{v_1} \Leftrightarrow v_1 = \frac{c_1 \cdot \left(\frac{\pi}{4} d^2\right)}{\dot{m}}$$

And the exit vapour fraction by use of

$$v = v_{liq} + x \cdot \left(v_{gas} - v_{liq}\right) \Leftrightarrow x = \frac{v - v_{liq}}{v_{gas} - v_{liq}}$$

The state functions h_{in}, h_{out} and s_{in} are calculated by use of the in-house facility Rn-lib.

The measured nozzle jet velocity, c_1 represents the average velocity in the cross section. This means that the specific volume estimated by use of this velocity is also an average density.

5.7.2 Nozzle losses

To follow the energy flow in the nozzle, the following steps were made
Start conditions:
$v_0 = v_0(t_{in}, p_{in})$
$h_0 = h_0(t_{in}, p_{in})$
$s_0 = s_0(t_{in}, p_{in})$
$\Delta h_s = h_0 - h_{end}(s_0, p_{out})$

The nozzle exit velocity (c_1) was calculated on basis of reactive power measurements as shown in 5.7.1. From this measurement the specific volume at the outlet was calculated. The specific volume was assumed to decrease linearly in the convergent nozzle part, then it was assumed to be constant in the straight part, and finally it was assumed to vary linearly in the divergent part.

At every point in the nozzle, the flow velocity was estimated by

$$c_n = \frac{\dot{m} \cdot v_n}{A_n}$$

The enthalpy was then estimated by

$$h_n = h_0 - \frac{c_n^2}{2}$$

In the convergent part, where there was only liquid CO_2 present, the pressure was estimated by Bernoulli.

$$p_n = p_{n-1} - \frac{0.5}{v_n} \cdot \left(c_n^2 - c_{n-1}^2\right) + \Delta p_f$$

In the straight and divergent parts, where CO_2 gas was present and a flashing flow would be expected, the pressure was estimated by a reorganised version of Eq (2-13)

$$p_n = p_{n-1} + \left(\frac{A_n - A_{n-1}}{A_n} + \frac{v_{n-1} - v_n}{v_{n-1}} \right) \cdot \frac{c_n^2}{v_n} + \Delta p_f$$

The nozzles tested had an inlet loss due to sudden contraction of the flow cross section. This was estimated by use of Eq (2-22).

$$\Delta p_{loc} = 0.5 \cdot \left(1 - \frac{A_0}{A_1}\right) \cdot \left(\frac{1}{2 \cdot v_0} \cdot \left(\dot{m} \cdot \frac{v_0}{A_0} \right)^2 \right)$$

The contraction loss was estimated by

$$\Delta p = \xi \cdot \rho \frac{c^2}{2}$$

Density and velocity for the smallest cross section were used in calculations. This loss was subtracted from the total pressure at the end of the convergent section. ξ was extracted from Idelchick (1994), diagram 5-23.

Nozzle friction losses were estimated by use of the routine dpdlFriedel, in the local facility dp-lib. This routine is based on Friedel (1979).

The equilibrium temperature of the two-phase mixture was calculated by $t_n = t_n(h_n, p_n)$

and from that the gas fraction was estimated

$$x = \frac{v_n - v_{liq}(t_n)}{v_{gas}(t_n) - v_{liq}(t_n)}$$

The isentropic expansion path was estimated by
$h_{s,n} = h(s_0, p_n)$
$x_{s,n} = x(t_n, h_{s,n})$
$v_{s,n} = v(t_{sat}, p, x_{s,n})$

The flash loss is then

$$\Delta e_{flash} = \frac{(v_{s,n-1} - v_{n-1}) + (v_{s,n} - v_n)}{2} \cdot (p_{n-1} - p_n)$$

The loss due to interrupted flashing is then calculated by
$\Delta e_{interrupt} = h(s_0, p_N) - h(s_0, p_{out})$

Where p_N is the calculated end pressure, and p_{out} is the measured pressure in the outlet chamber. The losses from flashing and interrupted flashing are shown in Figure 2-15.

The losses due to incomplete expansion are then

$$\Delta e_{incomplete} = \Delta e_{flash} + \Delta e_{interrupt}$$

5.7.3 Expander shaft power and total efficiency

As shown in Eq 2-17 the turbine shaft power equals the product of the turbine shaft torque and the angular velocity. The turbine shaft torque and the turbine speed are measured directly. The speed is measured as a voltage signal (0-10 V) in the Tach Monitor of the SWM software for supervision of the brake motor. The voltage signal is then converted as follows

$$n[rpm] = \frac{U_{Tach\_monitor}}{U_{Tach\_Monitor,max}} \cdot n(U_{Tach\_Monitor,max})$$

The turbine speed is then converted to angular velocity by

$$\omega = \frac{n \cdot 2\pi}{60}$$

The following measurements are needed to find the turbine shaft power

- Turbine shaft torque measurement
- Tach monitor signal

The isentropic expander efficiency is the quotient of the shaft power to the isentropic enthalpy change, as shown in Eq 2-27. With experimental measurements the equation takes the following form

$$\eta_{tot} = \frac{M \cdot \omega}{\dot{m} \cdot \Delta h_s} = \frac{M \cdot \omega}{\dot{m} \cdot \left(h(s_{in}, p_{out}) - h(T_{in}, p_{in})\right)}$$

5.7.4 Critical bubble radius

For characterisation of turbine performance it is desirable to be able to estimate the nozzle jet speed based on the nozzle process conditions. One possible parameter that can be used for characterising the nozzle inlet conditions is the critical bubble radius as defined in Eq (2-40)

$$r_c = \frac{2 \cdot \sigma(t_{sat})}{p_{sat} - p_{out}}$$

t_{sat} represents the fluid temperature in the point when the two-phase line is crossed. This was found found by goal seek in MS Excel as the temperature giving $s_{sat} = s(TT01,PT01)$

Measurements needed: TT01, TT02 and PT02

The correctness of using the measured outlet pressure can be questioned because the pressure that actually will affect the critical bubble radius is the local pressure in the nozzle. This was however the closest available approach to plotting the nozzle test results as function of process conditions.

5.7.5 Nozzle jet velocity as function of experimental inlet conditions

c_1 is estimated as

$$c_1 = \sqrt{2 \cdot \eta_{nozzle} \cdot \Delta h_s(t_{in}, p_{in})}$$

The geometrical parameters are extracted from Figure 3-7 and Table 3-4. The nozzle efficiency is extracted from relevant experimental data as a function of r_c, as defined in 5.7.4.

5.7.6 Blocked shaft optimal torque

The blocked shaft optimal torque is estimated by

$$\tau = \dot{m} \cdot \left(r_2 \cdot c_1 \cdot \cos(\lambda) \cdot \cos(180 - \beta_2) + r_1 \cdot c_1 \cdot \cos(\lambda) \cdot \cos \alpha_1 \right)$$

Where c1 is estimated as described in 5.7.5.

The ratio of measured to optimal torque is

$$Ratio = \frac{M_{meas} + M_{start}}{M_{ideal}}$$

5.7.7 Sum of losses at static shaft

Geometrical measurements before testing showed that the turbine rotor was positioned so that only 90 % of the nozzle jet could hit the turbine blade if the jet was 100 % cylindrically shaped. For calculation of losses this was taken info account. With the ratio between measured torque and ideal shaft torque as defined in 5.7.7, a sum of losses is indicated. The sum consisted of the following losses

- Drag between jet and turbine blades
- Back flow through non-active blades due to secondary flow set up by the nozzle
- Jet not hitting or hitting non-optimally

The drag is estimated by using drag between a flat plate and a homogeneous jet.

Losses due to back flow through non-active blades were assumed to be small because most of the possible secondary flow profiles would not go through other turbine blades, and because the nozzle was placed 0.4-2 mm from the turbine blade inlet, which means that there little space available to set up secondary fluid flows.

The rest of the losses were then assumed to be caused by that the jet was not hitting the turbine blade. This means that the torque deviation is caused by reduced mass flow through the turbine blade.

5.7.8 Losses at rotating turbine

Bearing losses were measured with the turbine driven by the motor, with vacuum in the turbine chamber. The power loss is then calculated as

$P_m = [\omega \cdot (M + M_{start})]_{p=0}$

Other rotational losses were measured with process pressure in the turbine chamber, and with the turbine driven by the motor
$P_{rot} = [\omega \cdot (M + M_{start})]_{p>0}$

The internal effect is calculated by use of Eq (2-37), which can be reorganized to

$$P_i = P_m + \eta_{tot} \cdot P_s$$

When the turbine is rotating without resistance from the motor, the total efficiency is 0, and the internal effect is used to overcome the bearing friction

The sum of losses in rotating turbine can then be estimated by eq (2-30), which reorganizes to

$$P_{rot} = P_{jet} - P_{tilt} - P_{exit} - P_{not-hit} - P_{drag} - P_i \qquad \textbf{(5-4)}$$

P_{rot} is a sum of losses due to

- 2 phase
- Windage losses
- Disc friction losses
- Changing angles
- Stagnation because some part of the jet hits the turbine blade at the end and is reflected.

The losses were described in 2.4.3.

The exit loss is calculated by use of velocity diagrams assuming no losses due to friction, and correcting for the fraction of the mass flow not hitting the turbine blade.

5.7.9 Principles for estimation of uncertainties

Details about the uncertainty calculations are given in Appendix 1.

For the uncertainties of a value calculated on basis of measured values, the uncertainty is calculated by the following general method described by Moffat (1988)

If the calculated value R is a function of the measured velues X_1, X_2, ..., X_n

$R = R(X_1, X_2, ..., X_n)$

Then the resulting uncertainty in R is then

$$\delta R = \left\{ \sum_{i=1}^{N} \left(\frac{\partial R}{\partial X_i} \delta X_i \right)^2 \right\}^{1/2}$$

δX_i here represents the uncertainty in the measurement of the variable X_i. The equation applies as long as

- Each of the measurements was independent
- Repeated observations of each measurement, if made, would display Gaussian distributions
- The uncertainty in each measurement was initially expressed at the same odds

In δX_i effects of uncertainty in the instrument and uncertainty in the data-logger due to digitalisation of an analog signal is contained.

$$\delta X_i = \sqrt{\left(\delta X_{i,instrument}\right)^2 + \left(\delta X_{i,\log ger}\right)^2}$$

For uncertainties related to instability in the process parameters, the standard deviation is estimated and used in the same place as the uncertainty. The total uncertainty is then

$$U = \sqrt{\left(\delta R\right)^2 + \left(t \cdot S_R\right)^2}$$

Where t is the student-t multiplier based on the number of observations in the sample.

The uncertainty calculations presumed that uncertainty in geometrical parameters will have negligible effect on the total uncertainty of the experiment.

5.8 Extrapolation of data

For evaluations of the general potential of an impulse expander in CO_2 expansion, and for evaluation of the experimental work, it might be necessary to extrapolate some data from a known state denoted by subscript 0. This might be due to lack of data for the desired speed, and due to lack of data for the desired geometry. The most important losses that will be extrapolated are bearing losses, disc friction losses and windage losses.

5.8.1 Bearing losses

Bearing losses were extrapolated from experiments, and for use in loss analysis in expander performance tests. With basis in the bearing loss measurements made with vacuum in the chamber, a trend line was developed. This was used to predict the bearing losses in the experiments.

5.8.2 Disc friction losses

The disc friction loss for an axial turbine is described by Eq (2-26), which shows that

$P_{disc} \sim \omega^3 R^5$

The disc friction loss is also proportional to the fluid density, but the real density will be roughly equal to the density from the experiments.

As the model turbine is a radial outflow turbine, the given expression is not 100 % correct for this case. In extrapolation however it is assumed that this can be compensated by changing the turbine blades' height with the same relative amount as the turbine radius.

In extrapolation it is assumed that

$$P_{disc} = P_{disc,0} \cdot \left(\frac{\omega}{\omega_0}\right)^3 \cdot \left(\frac{R}{R_0}\right)^5$$

5.8.3 Windage losses

The windage losses are described by Eq (2-27), which shows that

$P_{windage} \sim \omega^3 \cdot D^4 \cdot h \cdot (1-\varepsilon)$

$$P_{windage} = P_{windage,0} \cdot \left(\frac{\omega}{\omega_0}\right)^3 \cdot \left(\frac{D}{D_0}\right)^4 \cdot \frac{h}{h_0} \cdot \frac{1-\varepsilon}{1-\varepsilon_0}$$

Here it is important to note that the windage losses extracted from experiments on the model turbine will be high because the turbine blades are not shielded against the effects from windage.

6 Experimental results

6.1 Chapter overview

This chapter summarises experimental results gained in expansion of CO_2 with a two-phase turbine and various two-phase nozzles.

The nozzle test results are presented as plots of nozzle efficiency vs bubble critical radius, as defined in 5.7.4. The bubble critical radius gives the opportunity to correlate the results with a parameter that is dependent on the process conditions, and that affects the nozzle performance. Some visualisation pictures are also presented.

For the turbine, tests were made with blocked shaft and with rotating turbine. The blocked shaft test results were plotted as shaft torque vs mass flow, whereas the turbine performance test results were presented in a table.

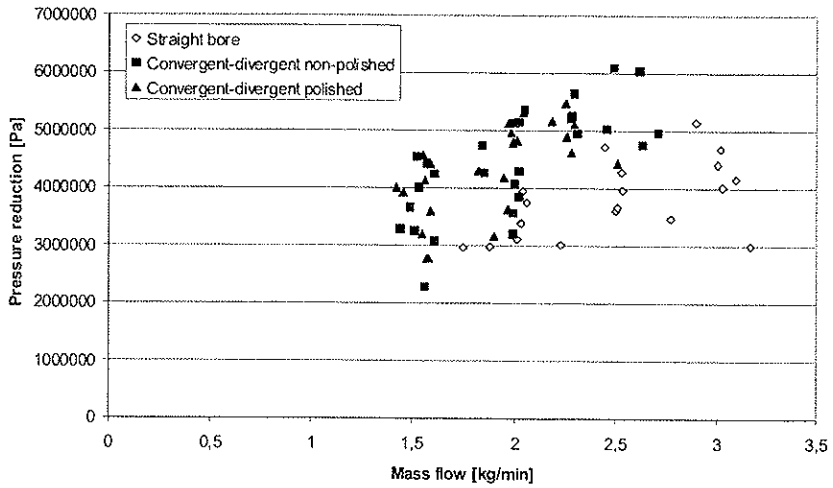

Figure 6-1. Pressure reduction vs mass flow for the three nozzles

The pressure reduction vs mass flow shows a lower pressure reduction for the straight-bore nozzle than the other nozzles. For the convergent-divergent nozzle, the difference between polished and non-polished was small. For the straight-bore nozzle compared to the convergent-divergent

nozzle, the shape seems to have important influence. The scattering in the data was caused by differences in the process conditions.

6.2 *Nozzle jet velocity*

6.2.1 Straight bore, polished

Figure 6-2 shows nozzle efficiency plotted vs. bubble critical radius for the straight bore polished nozzle.

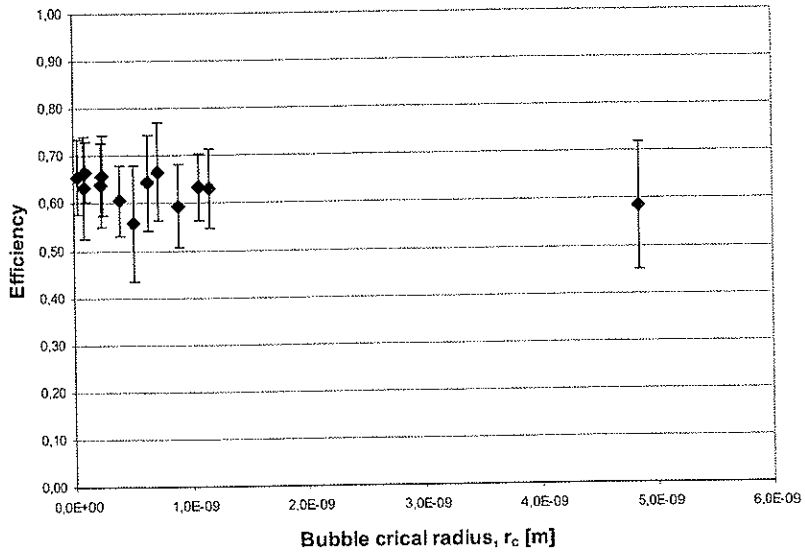

Figure 6-2. Nozzle efficiency vs bubble critical radius for straight bore nozzle

The main results from the straight-bore nozzle show that the efficiency is between 0.6 and 0.7. There seems to be no correlation between the bubble critical radius and the efficiency. This indicates that flashing is not important for this nozzle. The uncertainties are calculated by use of the principles as shown in Appendix 1. Two of the results with $\eta < 0.6$ are also the results with highest uncertainty. Differences in uncertainty range occur because some experiments had unstable process conditions.

6.2.2 Convergent-divergent nozzle

Figure 6-3 and Figure 6-4 show comparison between the performance of the convergent-divergent nozzle before and after polishing. Figure 6-4 shows all the tests that were made, whereas Figure 6-3 shows a shorter range of critical radii. This was made to see the details in the low range better. The efficiencies were estimated as shown in 5.7.1, and the uncertainty estimations as shown in Appendix 1.

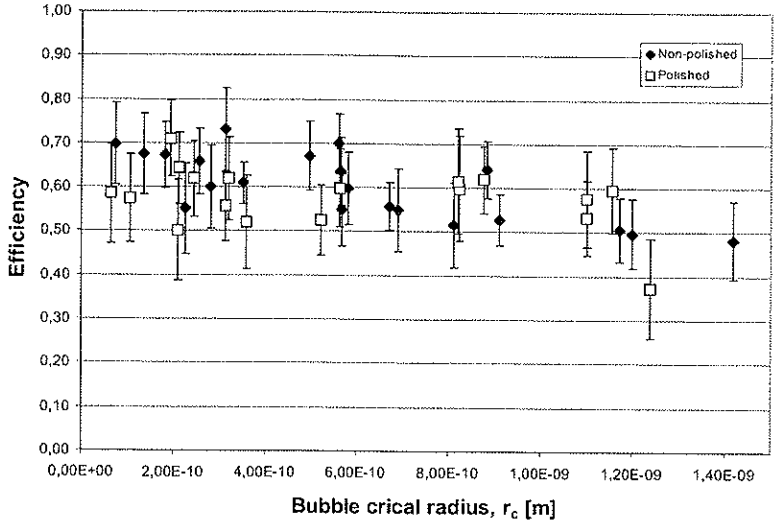

Figure 6-3. Nozzle efficiency vs bubble critical radius for convergent-divergent nozzle, $r_c < 1.5 \cdot 10^{-9}$ m

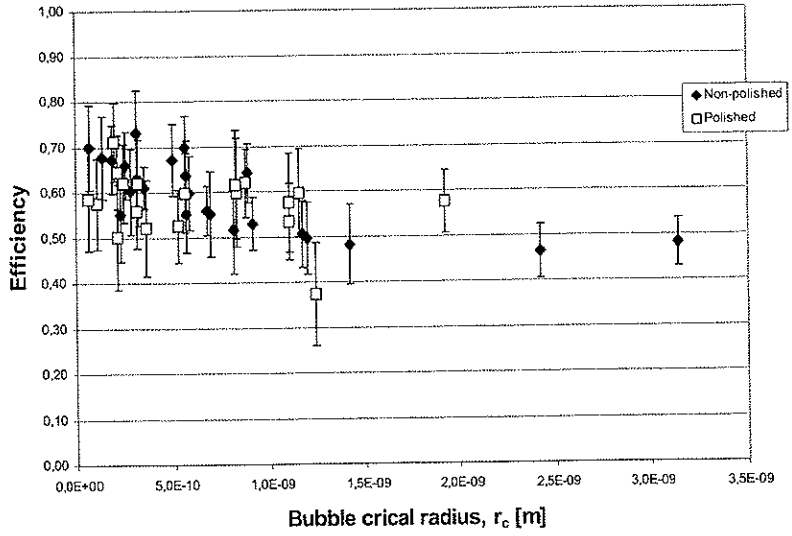

Figure 6-4. Nozzle efficiency vs bubble critical radius for convergent-divergent nozzle, all tested r_c

In Figure 6-4 the nozzle efficiencies are plotted vs. the calculated bubble critical radius. The relevance of this plot might be questioned as the critical radius depends on process conditions inside the nozzle. It was however necessary to find some way of plotting the results on basis of properties estimated by the inlet conditions. As shown in Figure 6-3 and Figure 6-4 a weak correlation between bubble critical radius and efficiency may be observed. This is as expected because a low estimated r_c gives better conditions for flashing. Because of uncertainties in the measurements and scattering in the results there is no significant difference between the two nozzles' performances, and the correlation between nozzle performance and bubble critical radius is weak.

6.2.3 Inlet multiple hole orifice plate

Figure 6-5 shows the results obtained by use of a multiple hole orifice plate, as described in 5.3.3, on the nozzle inlet.

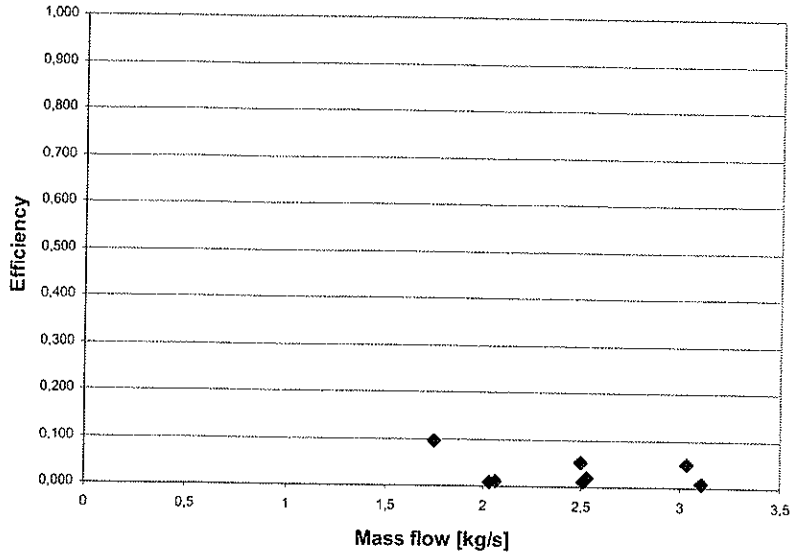

Figure 6-5. Efficiency vs mass flow for polished convergent-divergent nozzle, with multiple hole orifice plate on the inlet

As discussed in 2.6.2 the multiple hole orifice plate was expected to improve the nozzle efficiency. The experiments showed a poor efficiency. Because of this, few tests were made with this configuration. One possible reason for the poor efficiency might be pressure drop in the plate and chaotic fluid flow conditions between the inlet plate and the nozzle throat. By disassembly of the nozzle with multiple-hole inlet plate, clogging of the plate was detected. Although it looked like the outer ring of holes was free, the clogging might have contributed to the result. When this was discovered, it was too late to make new measurements. With the dimensions used in this work, a multiple holes orifice plate will have thin passages. It is important to remember that this can cause big problems with clogging in real use, as well as in laboratory testing.

6.3 Nozzle flow visualisation

Because of flow conditions inside the see-through glass, nozzle flow visualisation was impossible at process conditions equal to the process conditions for other expansion tests. In order to gain insight into the expected nozzle jet shape and fluid dynamic conditions around the nozzle jet, high-speed filming was made at process conditions where it was possible to visualise a nozzle jet behind recirculation flow profiles.

6.3.1 Jet shape

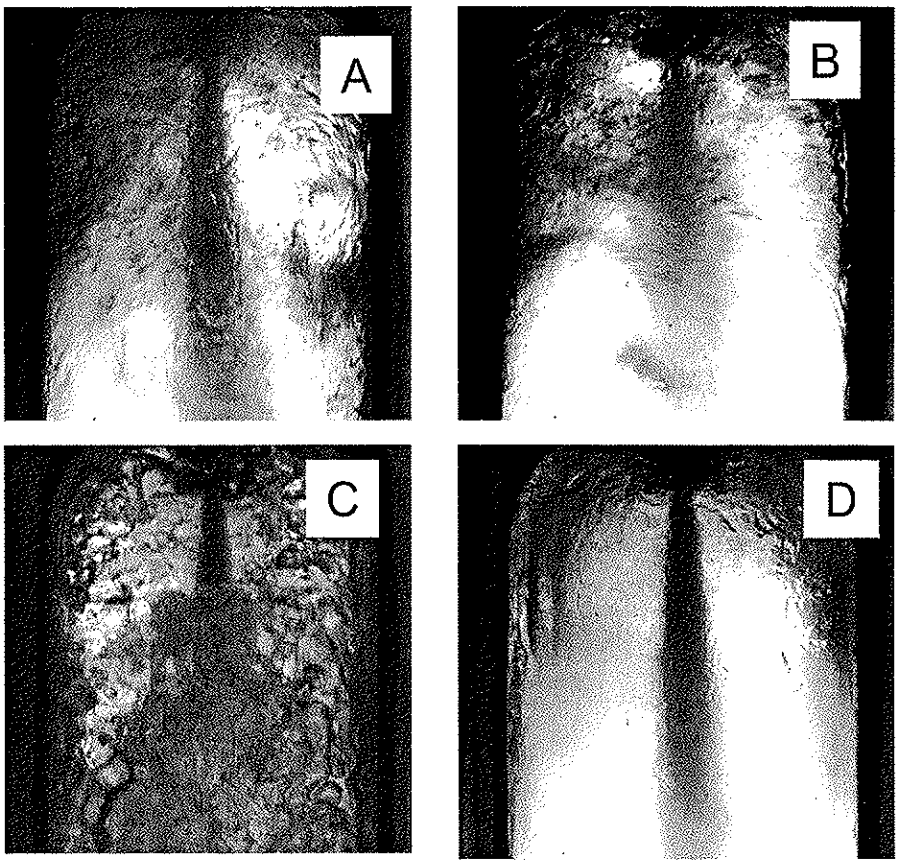

Figure 6-6. Jet shapes for various process conditions

Figure 6-6 shows jet shapes for various process conditions as shown in Table 6-1. All the pictures show a conical jet shape. The ideal shape for the impulse expander is however straight and these pictures show that considerable fractions of the nozzle jet would miss the turbine blade if

these conditions were applied on the turbine wheel. The conical jet shape might indicate an incomplete expansion in the nozzle, and a probable reason for that is mismatch between nozzle design and process conditions. Picture A and B show relatively violent conditions, although these experiments have flow rates and inlet pressures below the expander and nozzle performance test conditions. In picture A it is possible to see a swirl, and in picture B, the nozzle jet seems to be concentrated only in a short distance. Picture C shows non-violent process conditions, which also explains why the jet is very clear here. The film however showed turbulent and quickly changing conditions here. In picture D, the expansion started with CO_2 gas. The consequence of this is less liquid available, which also explains why the nozzle jet is so clear.

Table 6-1. Process conditions for nozzle flow visualisation

	TT01	PT01	PT02	m
	[°C]	[bar]	[bar]	[kg/s]
A	19,6	57,0	42,3	0,012
B	25,6	63,1	42,4	0,013
C	4,6	39,4	35,9	0,010
D	28,7	61,1	42,7	0,012

Table 6-1 gives the process conditions for nozzle flow visualisation tests. Comparing this to the design basis as given in Table 3-1, shows that these tests have only 25 % of the design basis' mass flow.

6.3.2 Secondary flow profiles

Downstream of the nozzle outlet, the flow profile was very turbulent and unstable. From Figure 6-7 however, a swirl can be seen clearly. Behind the swirl, it is possible to see the nozzle jet.

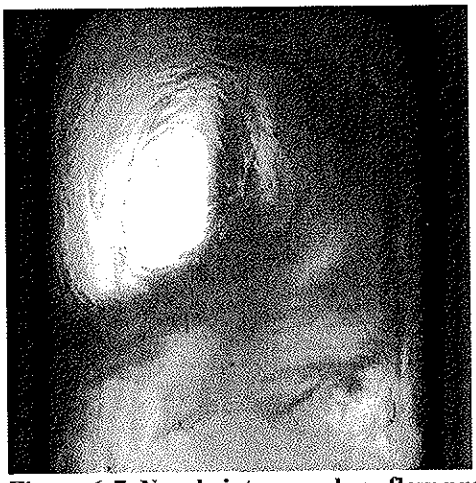

Figure 6-7. Nozzle jet, secondary flow profile

The secondary flow profiles might have some influence on the turbine efficiency. With the current turbine configuration, the secondary flow profiles may lead to discharged fluid re-entering the turbine rotor through the turbine blades, which contributes to increasing the windage losses described in 2.4.3.

6.4 *Expander testing*

6.4.1 Blocked shaft torque measurement

Before the testing with blocked shaft was conducted, the nozzle position in relation to the rotor position was measured to check whether the jet could hit the turbine blade. The measurement was made by two different operators, who came to the same answer, that max 90 % of the jet could hit the turbine blade in that position.

Figure 6-8 and Figure 6-9 show the ratio of ideal shaft torque to measured shaft torque. Estimation of the ideal shaft torque is shown in 5.7.6.

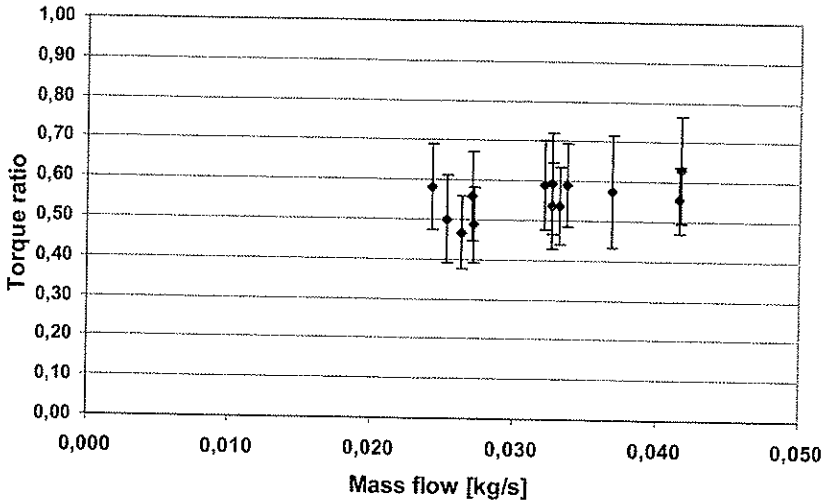

Figure 6-8. Actual to ideal shaft torque vs. mass flow for blocked shaft turbine measurements. Inlet temperature 20-25 °C, Inlet pressure 62-75 bar, Outlet temperature 2-10 °C

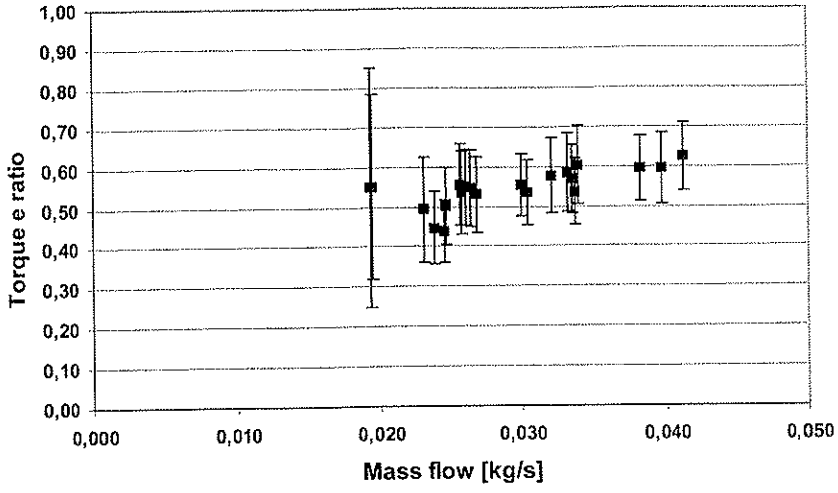

Figure 6-9. Actual to ideal shaft torque vs. mass flow for blocked shaft turbine measurements. Inlet temperature 30-35 °C, Inlet pressure 84-100 bar, Outlet temperature 2-11 °C

The blocked shaft torque measurements shown in Figure 6-8 and Figure 6-9 indicate that the ratio of actual to ideal shaft torque is improved by increasing mass flow. One possible reason is that a higher mass flow gives better filling of the turbine blades. The jet with higher mass flow contains more energy, which reduces the relative importance of the losses. This also indicates that the turbine blades might be optimal for higher flow rates than the flow rates tested. Comparing the two figures, there are no considerable differences in Figure 6-8 compared to those in Figure 6-9. The measurements in Figure 6-9 had the highest inlet temperatures. These data also have lower uncertainty. The reason for the lower uncertainty is probably that the process conditions were more stable.

Figure 6-10 and Figure 6-11 show actual and ideal shaft torque vs. mass flow. The results seem to be linearly dependent on the mass flow, which would be expected according to Eq (2-21) for ideal shaft torque. The data show that the relative deviation is highest at the lowest mass flow rates although the absolute deviation is higher at the highest mass flow rates.

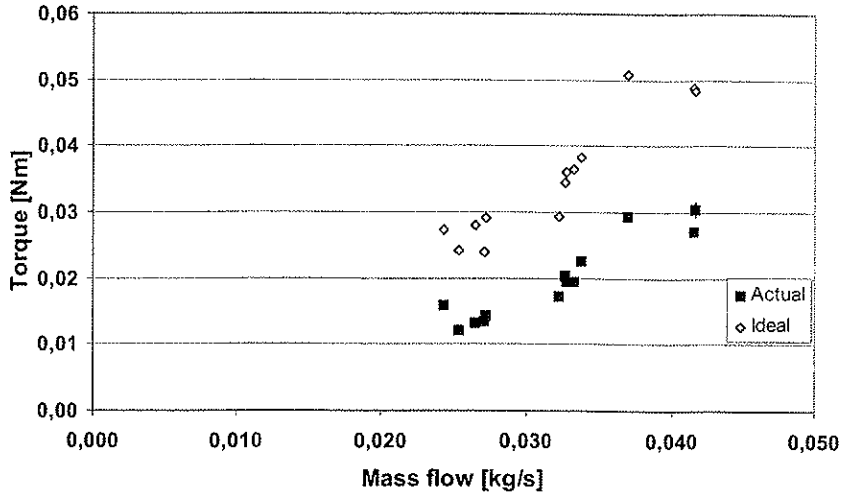

Figure 6-10. Actual and ideal shaft torque vs. mass flow for blocked shaft turbine measurements. Inlet temperature 20-25 °C, Inlet pressure 62-75 bar, Outlet temperature 2-10 °C

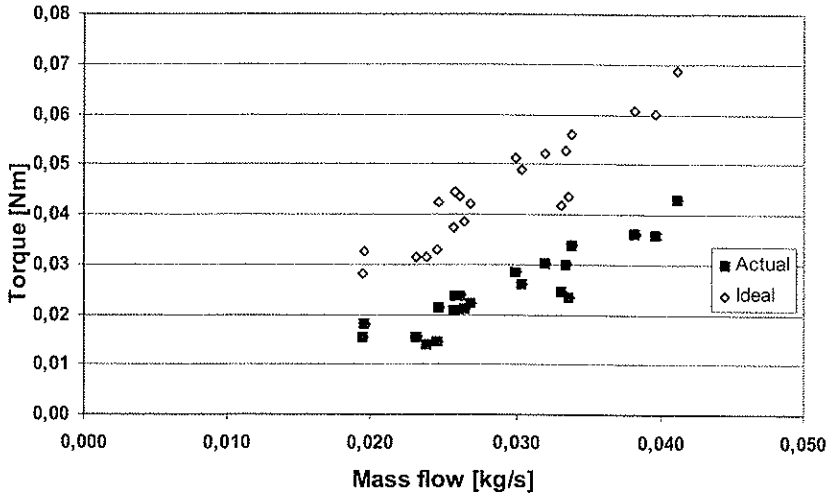

Figure 6-11. Actual and ideal shaft torque vs. mass flow for blocked shaft turbine measurements. Inlet temperature 30-35 °C, Inlet pressure 84-100 bar, Outlet temperature 2-11 °C

6.4.2 Bearing loss characterisation

The results from bearing loss testing are shown in Table 6-2. The measurements have very high standard deviations because it was impossible to run on a stable speed. Comparing these standard deviations to the instrument uncertainties as given in Table 4-3 shows that the instrument uncertainties are negligible compared to the standard deviations.

Table 6-2. Results from bearing loss tests

Exp. No	ω	S_ω	M	S_M	P	S_P	N	U
t002[1)]	5083	676	0,020	0,009	104	48	13	108
t008	6045	157	0,010	0,003	60	18	12	41
t003	2122	233	0,0100	0,001	21	3	12	7
t004	3294	117	0,0164	0,0003	54	2	11	5
t015	3680	562	0,014	0,001	52	9	12	21

1) Atmospheric pressure

The results of Table 6-2 are plotted in Figure 6-12. The results given at the highest speeds have the highest uncertainties, so these are not included in calculation of the trend-line indicated in the diagram. The trend line equation shows that the bearing loss is $\sim\omega^{1,77}$.

Eq (2-30) for bearing torque says that the bearing torque is on the following form

$$M = A \cdot (\omega \cdot \upsilon)^{2/3} + B$$

Where A is a constant dependent on the bearing geometry and the bearing type, B is dependent on the load and υ is the lubrication agent viscosity. The bearings were exposed to minimal load, only due to the mass of the turbine shaft and motor-rotor, so it can be shown that B is negligible towards the other term. When the Bearing torque is $\sim\omega^{2/3}$, the bearing loss would be expected to be $\sim\omega^{5/3}$, which is not far away from the proportionality indicated in the trend line.

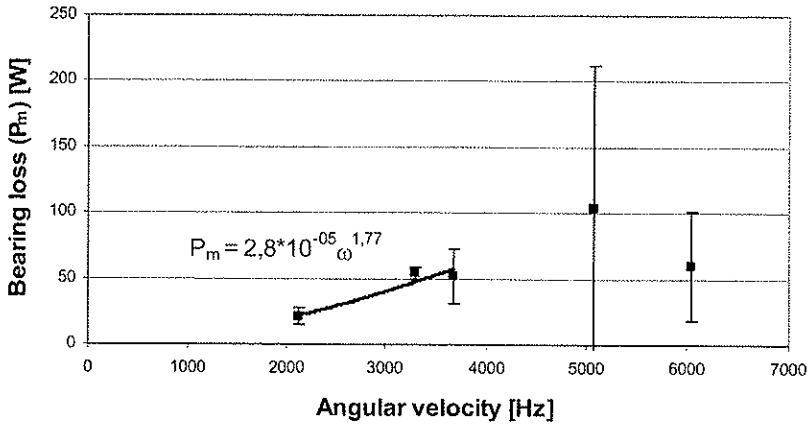

Figure 6-12. Bearing losses vs angular velocity

The lubrication agent viscosity is dependent on the temperature. One major uncertainty in the bearing tests is the lubrication agent viscosity because there is no temperature monitoring around the bearings. After experiment t002, the temperatures of shaft and front plate (Ref: Figure 5-4 pos 13 and 3) were measured. The shaft temperature was measured to 47 °C and the front plate to 31 °C, and before the experiment they were expected to be around 23 °C. Table 6-2 shows that t002 had high speed, and hereby high bearing losses. With lower speed, the bearing losses are reduced, and the temperature increase in and around the bearings should be expected to be smaller than the measured values. For the use of the bearing losses in turbine performance calculation on the other hand, the chamber will be cooled by liquid CO_2 when turbine tests are run. Hence the front bearing will rather have lower temperature than the bearing characterisation tests. This means that the bearing losses estimated on basis of the trend line indicated in Figure 6-12 might be slightly underestimated.

6.4.3 Rotational loss characterisation

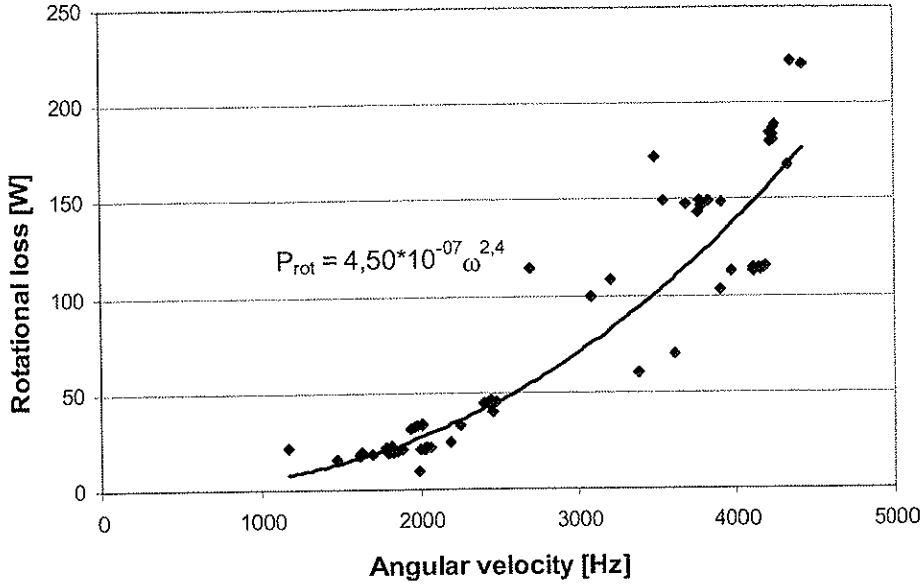

Figure 6-13. Bearing losses + disc friction losses vs angular velocity

The total rotational losses were measured at chamber pressure around 40 bara. The results seem to fit to the indicated trend line, but with considerable scatter.

At low speeds there are some clear deviations from the trend line. These deviations occur in the series' first measurements and show losses lower than the indicated trend line. This might be caused by the average building in the data logger or by a delay in the torque measurement due to friction in the bearing where the torque is measured (Ref: Figure 5-4, pos 25). The values that are higher than the trend are typically the last measurements before deceleration. This is probably caused by the same effects.

The instrument and logger uncertainties are given in Table 4-3, and compared to the variations in torque and angular velocity (as shown in Table 6-3), those uncertainties are negligible. As shown in Table 6-3, the experiments were performed with considerable variations in the angular velocity as. This also gave variation in the measured torque. The standard deviations of measured torque and speeds are high. Estimating uncertainties in these data according to the principles in 5.7.9 would give very high uncertainties because the standard deviation is so high.

Table 6-3. Experimental data for rotational loss characterisation

Exp. No	ω	S_ω	M	S_M	P	S_P	U_P
t001	1799	46	0,0109	0,0001	19,6	0,5	1
t007	2210	441	0,014	0,009	32	20	40
t009	3703	757	0,023	0,008	86	33	66
t014	3872	469	0,039	0,002	150	20	40
t016	3225	1006	0,034	0,014	109	56	112
t019	2108	365	0,014	0,005	31	12	24

The data of Table 6-3 are plotted in Figure 6-14. Some of the values have high uncertainty. This is due to instability in the angular velocity, which also leads to unstable shaft torque. Comparing the equations for the trend-lines in Figure 6-13 and Figure 6-14 shows that they have the same shape, but the trend line in Figure 6-13 has more than double the coefficient of the trend-line in Figure 6-14. The difference probably arises because the trend-line of Figure 6-14 uses mean values from data that vary over a wide range.

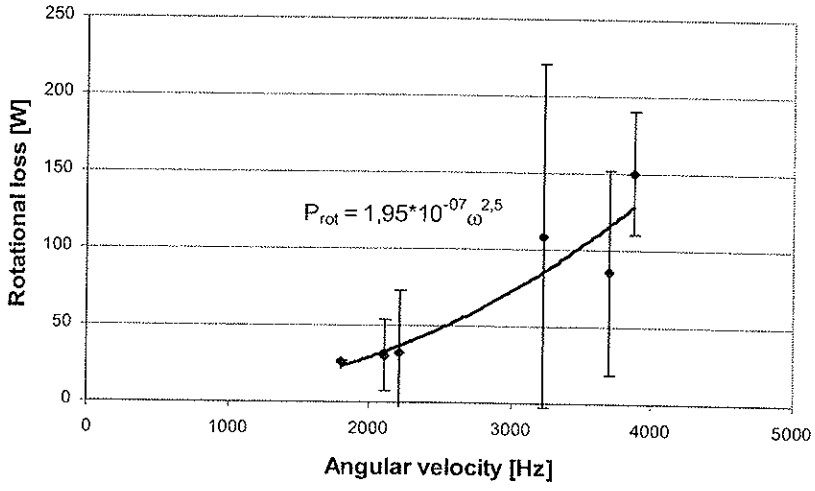

Figure 6-14. Average values and uncertainties for the series of rotational loss measurements

6.4.4 Expander performance testing

The tests shown in Table 6-4 were made with a turbine without brake. The turbine is then rotating at the maximal velocity. When the turbine rotates at maximal speed, the internal effect is used to overcome bearing losses. As the bearings were grease lubricated, the bearing losses were also relatively high.

Table 6-4. Results from turbine tests where the brake was not working. N is number of samples in each experiment

Exp	TT01	TT02	PT01	PT02	m	ω	N
	[°C]	[°C]	[bara]	[bara]	[kg/s]	[Hz]	
t010 ±	33.82	10.71	99.31	45.92	0.0390	1669	5
St. dev	± 0.20	± 0.01	± 1.39	± 0.01	± 0.0010	± 30	
t011 ±	18.60	6.40	98.71	41.29	0.0538	1482	7
St. dev	± 0.08	± 0.01	± 0.23	± 0.01	± 0.0002	± 19	
t012 ±	18.66	6.07	99.97	40.96	0.0543	1513	3
St. dev	± 0.06	± 0.05	± 0.36	± 0.05	± 0.0001	± 40	
t013 ±	18.36	5.59	91.41	40.46	0.0498	1455	4
St. dev	± 0.14	± 0.08	± 0.46	± 0.07	± 0.0003	± 30	
t005 ±	27.91	7.97	86.76	42.92	0.0374	1379	7
St. dev	± 0.13	± 0.14	± 0.30	± 0.14	± 0.0002	± 67	
t006 ±	28.29	7.33	87.27	42.25	0.0373	1437	19
St. dev	± 0.09	± 0.05	± 0.24	± 0.04	± 0.0002	± 51	
t017 ±	28.60	9.24	86.17	44.28	0.0354	1422	9
St. dev	± 0.42	± 0.06	± 0.18	± 0.05	± 0.0003	± 9	
t020 ±	33.41	11.00	99.28	46.30	0.0396	1584	8
St. dev	± 0.12	± 0.04	± 0.15	± 0.04	± 0.0001	± 19	

Table 6-5 shows the results from tests where the brake was used. The experiments in this table have the same experiment numbers as two of the experiments without use of brake. That is because the turbine was stabilized at the maximal velocity before the brake was used.

Table 6-5. Results from turbine tests where the brake was used

Exp	TT01	TT02	PT01	PT02	m	M	ω	P	η
	[°C]	[°C]	[bara]	[bara]	[kg/s]	[Nm]	[Hz]	[W]	[-]
t017	29,8	9,0	87,3	44,0	0,035	-0,008	850	-7,0	0,030
t020	33,6	10,9	99,4	46,2	0,040	-0,009	927	-8,4	0,026

The test results show that the turbine did not reach the intended speed, and the efficiency measurements show low values. Optimal speed for this

expander, at the tested conditions, would be expected to be around 60000 rpm which corresponds to $\omega \approx 6000$ Hz. Probable reasons why the intended speed was not reached are various losses discussed in 2.4.3, including

- Bearing losses
- Rotational losses due to friction between rotor and surrounding medium
- Windage losses
- Two-phase losses

7 Discussion

7.1 Chapter overview

This chapter evaluates the impact of the experimental results. That is done in the following steps.

The nozzle test performance results will be evaluated by explaining which physical relations that caused the results.

The expander performance will also be evaluated. The results showed that the current model expander is having a poor efficiency. It is important to point out possible reasons for this, and also show the relationship between the results and the expander design, and to show the contribution of each component to the expander performance.

The methods used will also be evaluated and weak points identified. Another important point is to identify the main sources for uncertainty, and if possible suggest possible improvements.

In evaluation of the expander performance, relationships between turbine design and performance will be explained. As a consequence of this, an improved design for a model expander will be suggested in order to reduce the identified loss sources of the expander. The proposed improvement of design also contains a prediction of efficiency for the improved machine.

Finally the chapter includes suggestions for further work related to the identified weak points of the current expander design.

7.2 *Nozzle performance*

7.2.1 Flashing losses and their consequences

The length of the nozzles tested was 0.02 m. If an average flow velocity around 100 m/s inside the nozzle is assumed, the fluid will be through the nozzle in 0.2 ms. In the flashing process, there will always be a delay from the point where the potential for flashing appears to the point where the flashing actually starts. When the fluid exits the nozzle so quickly as in these tests, there is a high probability that the flashing process will not reach equilibrium inside the nozzle.

Another important issue is critical flow. As shown in Figure 7-1, the critical flow velocity is around 100 m/s at exit conditions. The critical flow velocities were calculated by eq (2-43). This tells that the exit fluid flow is probably critical, which might cause the expansion process to be incomplete if the divergent part of the nozzle has too low outlet diameter. This again gives a conical nozzle jet, where a high fraction will not hit the turbine blade and hereby cause a loss. A conical jet would also have a higher probability of hitting the turbine blade from the back and hereby brake the turbine.

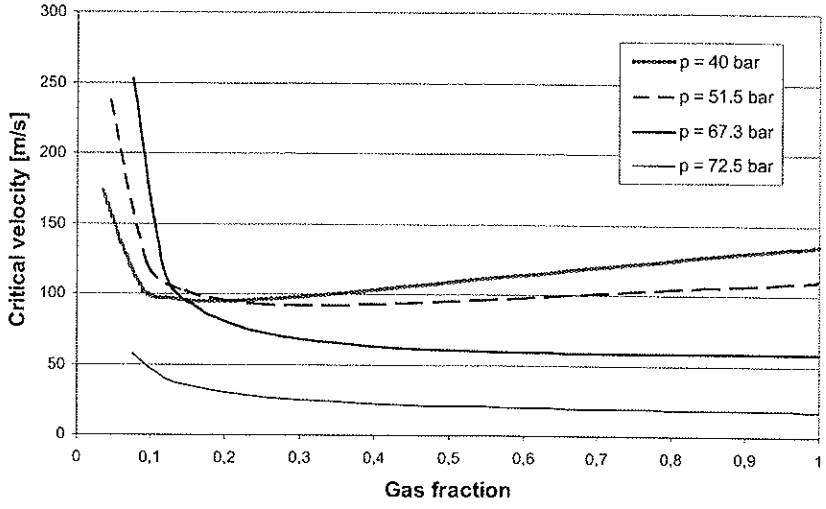

Figure 7-1. Shows the critical velocity plotted versus gas fraction for various process conditions

Ideally, the nozzle jet shall be completely expanded when it leaves the nozzle and enters the turbine rotor. From flow visualisation tests shown in

6.3 there were clear indications that the nozzle jet was not completely expanded because it had a conical shape.

If the nozzle fluid is boiling violently because of incomplete flashing after the turbine discharge, this may lead to small liquid droplets being shot back into the turbine wheel. This increases the windage losses. For the experimental turbine, where the fluid was discharged at the turbine periphery without any means for handling the discharge flow afterwards, deceleration effects because of liquid hitting the turbine blades will probably occur. In a real turbine, it will be very important to account for this and include some means for handling discharge flow in the construction.

The incomplete expansion losses presented in Figure 7-2 were calculated according to the method described in 5.7.2.

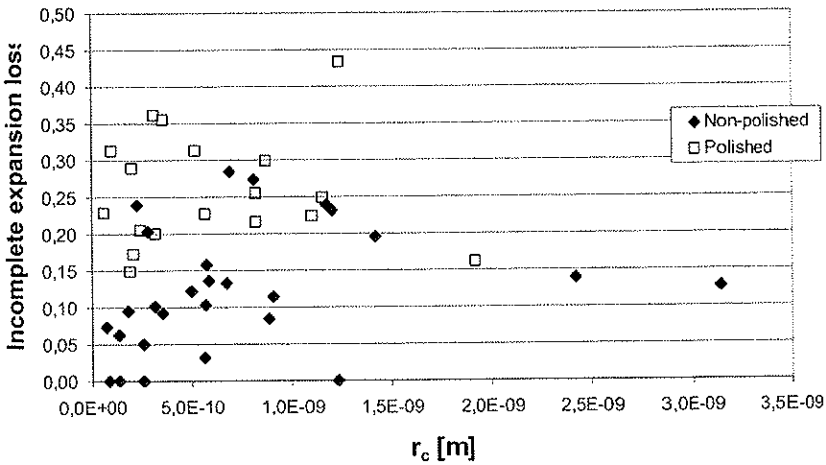

Figure 7-2. Incomplete expansion loss vs r_c for the convergent-divergent nozzles

As shown in Figure 7-2 the highest incomplete expansion losses are calculated for the polished nozzle. One possible reason is that differences in the surface roughness give differences in the vaporisation rate. Another possible explanation is that the extra pressure drop in the non-polished nozzle creates extra potential for flashing.

7.2.2 Distribution of losses in the nozzles

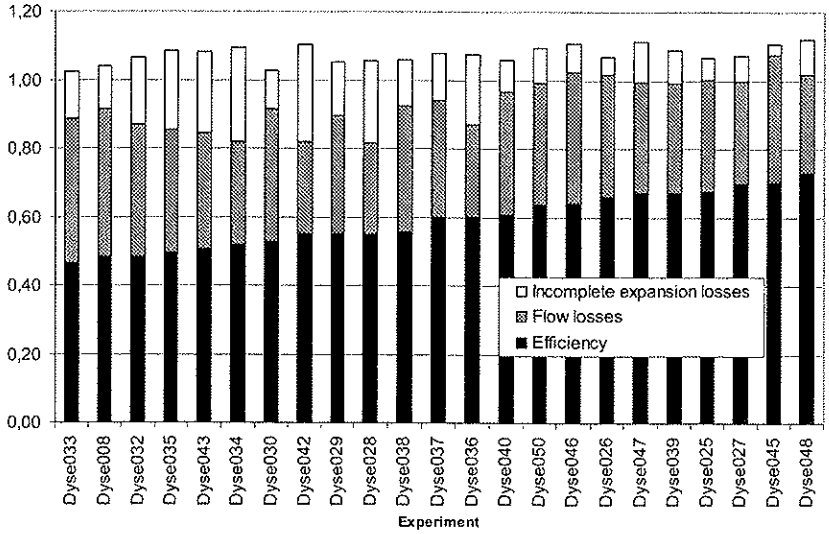

Figure 7-3. Losses and efficiency in non-polished nozzle

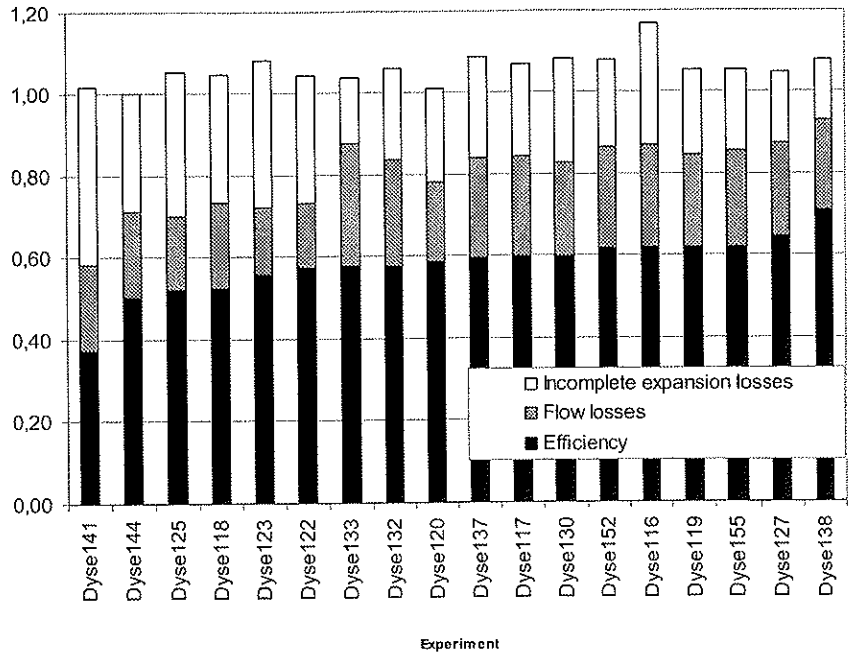

Figure 7-4. Losses and efficiency in polished nozzle

Figure 7-3 and Figure 7-4 show the distribution of losses in the two versions of the convergent-divergent nozzle. These losses were calculated according to the principles described in 5.7.2. All the results show sum of losses and efficiency higher than 1. This means that the losses and the efficiencies are overestimated. The deviation is however not high. The results are not plotted vs. experimental conditions, but the same experimental program was run on the different nozzles. The figures show that the efficiencies achieved are roughly similar, and differences are well within the uncertainty of the method. The losses due to friction and incomplete expansion were calculated by the method as shown in 5.7.2. As the polished nozzle has a lower surface roughness, the friction pressure drop is lower, and hereby the flow losses are lower than the flow losses in the non-polished nozzle. Comparing the calculated incomplete expansion losses on the other hand shows that they are much higher in the polished nozzle than in the non-polished. Because of lower friction losses, the polished nozzle must be expected to have a higher end-pressure than the non-polished one, this is in accordance with the differences in losses due to incomplete expansion. One possible improvement for the polished nozzle is to manufacture a unit with bigger outlet diameter because this might give the opportunity to avoid losses due to interrupted flashing.

7.3 Blocked shaft tests

The blocked shaft test reported in 6.4.1 were analysed as described in 5.7.7. Figure 7-5 shows that the drag losses in the turbine blade cause a small fraction of the total losses, considering the torque ratios presented in Figure 6-8 and Figure 6-9. The rest of the losses are then assumed to be caused by the jet not hitting the blades.

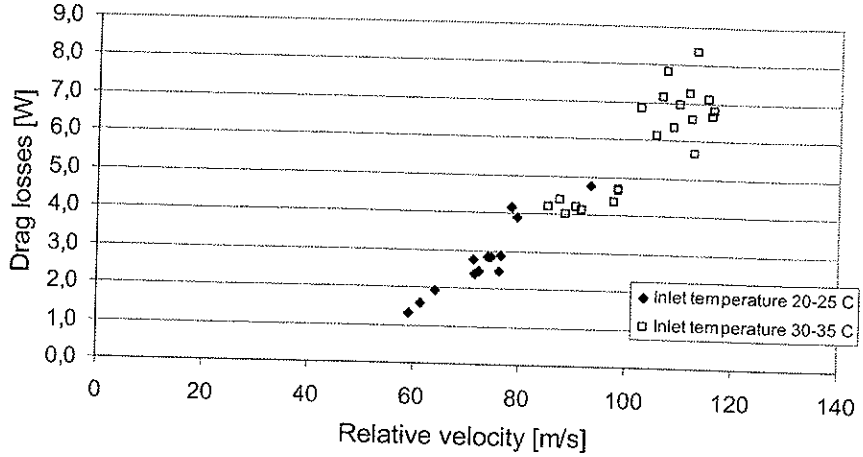

Figure 7-5. Drag losses in turbine blades

Figure 7-6 and Figure 7-7 show the fraction of the nozzle jet not hitting the turbine blade. The results show a weak tendency for the fraction to decrease by increasing mass flow.

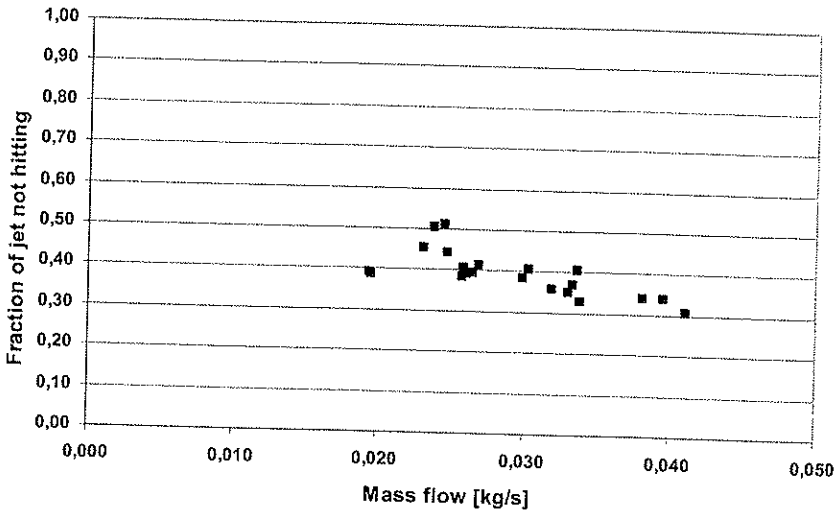

Figure 7-6. Fraction of jet not hitting vs mass flow. Inlet temperature 30-35 °C, Inlet pressure 84-100 bar, Outlet temperature 2-11 °C

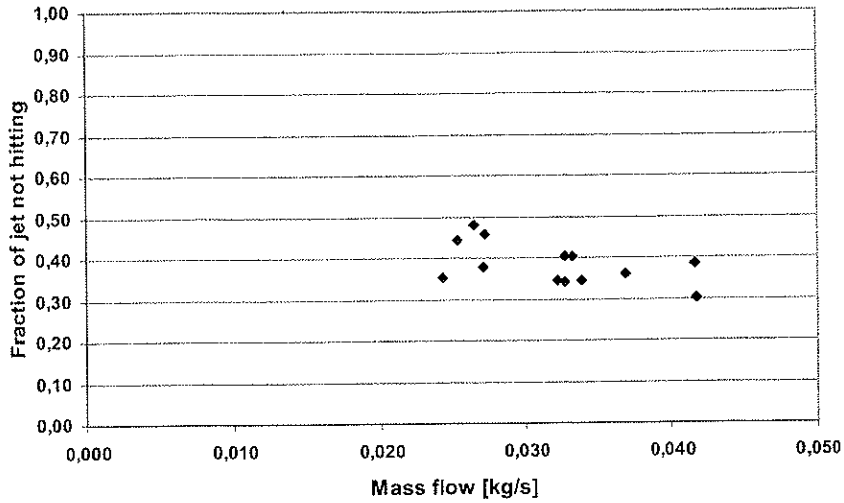

Figure 7-7. Fraction of jet not hitting vs mass flow. Inlet temperature 20-25 °C, Inlet pressure 62-75 bar, Outlet temperature 2-10 °C

The nozzle jet visualisation tests reported in 6.3 support the assumption that high fractions of the jet are not hitting the turbine blade.

Figure 7-5 shows that the turbine will have low losses due to friction between the turbine blades and the flowing fluid.

The indications that a high fraction of the jet is not hitting the turbine blade are also consistent with an incomplete expansion in the nozzle and a shock at the nozzle outlet.

7.4 Expander performance

7.4.1 Loss analysis

The input energy to the expansion wheel is the nozzle jet power (P_{jet}). The nozzle jet power is calculated as shown in Eq (2-14). The nozzle jet velocity was estimated as shown in 5.7.5.

For the loss analysis, the following losses were considered.

- Drag
- Jet not hitting
- Exit
- Tilting
- Bearings
- Rotational

The losses are discussed in 2.4.3, and the data reduction for estimating losses is shown in 5.7.7 and 5.7.8. Velocity diagrams for the turbine, assuming no friction losses, were set up as shown in Figure 2-17, and with geometrical dimensions as given in Table 3-4.

The non-rotational loss due to drag friction was estimated by assuming homogeneous fluid flow over a flat plate. With the relative velocity as estimated by turbine velocity diagrams, the drag loss was extracted from Figure 7-5. With the measured mass flow, the fraction of the jet not hitting the turbine blades was extracted from Figure 7-6 or Figure 7-7, dependent on the process conditions.

The exit loss was estimated as the kinetic energy in the fluid leaving the turbine blade. The estimate used the exit, absolute velocity (c_2), and the fraction of the mass flow that entered the turbine wheel.

The tilting loss is the loss caused by the nozzle approaching the turbine wheel in an angle of 16° compared to the radial plane, as shown in Figure 2-18. The uncertainty in this value was estimated together with the uncertainty in power from the jet (P_{jet}).

The bearing losses were estimated by extrapolation of the data in Figure 6-12, with uncertainties given in Table 6-2.

The rotational losses were calculated as the difference between the estimated jet energy and the sum of the other losses.

Table 7-1. Loss analysis for the turbine performance tests

	P_{jet}	P_{exit}	$P_{tilting}$	$P_{not-hit}$	P_{dragt}	P_m	$P_{rotational}$	N
	[W]	[W]	[W]	[W]	[W]	[W]	[W]	
t010	196.4	76.0	14.9	64.8	4.5	14.1	22.0	5
S	31.1	23.2					4.2	
δ	31.5	23.6		16.0		7	11.1	
t011	171.7	71.0	13.0	42.9	2.5	11.5	30.8	7
S	7.7	5.6					1.4	
δ	32.5	23.4		14.0		7	11.6	
t012	178.2	73.5	13.5	44.5	2.5	11.9	32.2	3
S	5.8	4.5					1.1	
δ	33.7	24.2		14.5		7	12.0	
t013	142.2	56.3	10.8	38.4	2.5	11.1	23.1	4
S	11.8	8.5					2.2	
δ	27.1	19.2		11.7		7	10.5	
t005	133.2	51.9	10.1	44.0	2.5	10.1	14.6	7
S	12.8	9.8					1.7	
δ	23.5	17.7		11.0		7	9.2	
t006	139.0	53.8	10.6	45.9	2.5	10.9	15.4	19
S	8.4	6.5					1.2	
δ	24.5	18.3		11.5		7	9.4	
t017	133.6	52.0	10.2	40.7	2.5	10.7	8.1	9
S	41.0	30.9					5.6	
δ	22.0	16.6		10.2		7	9.1	
t020	194.5	76.5	14.8	59.3	3.5	12.9	13.9	8
S	12.5	9.5					0.0	
δ	31.1	23.6		14.7		7	9.1	

Table 7-1 shows that the losses and the jet energy have high uncertainties. The rotational losses are calculated as described in 5.7.8. As it is estimated as a sum of the other losses, it would be logical to assume that the rotational losses have an uncertainty higher than its own value. The uncertainties in the losses origin from uncertainty in nozzle efficiency that again gives uncertainty in the nozzle jet velocity and in the ratio of measured to optimal torque as measured in the blocked shaft testing. It is therefore possible that the uncertainties in discharge and non-rotational losses cancel out against the uncertainty of the jet energy.

Summing equation (5-4) gives an equation dependent on ω^2 and c, and with some dependency on c^2. As the highest uncertainties origin form the uncertainty in the nozzle jet velocity, this means that the rotational losses can be estimated with a fair grade of precision based on the experimental data. This is also seen in Table 7-1.

The losses summarised in Table 7-1 are shown in Figure 7-8. Here it can be seen that the most important losses are

- Exit loss
- Loss from jet not hitting the blade
- Rotational losses

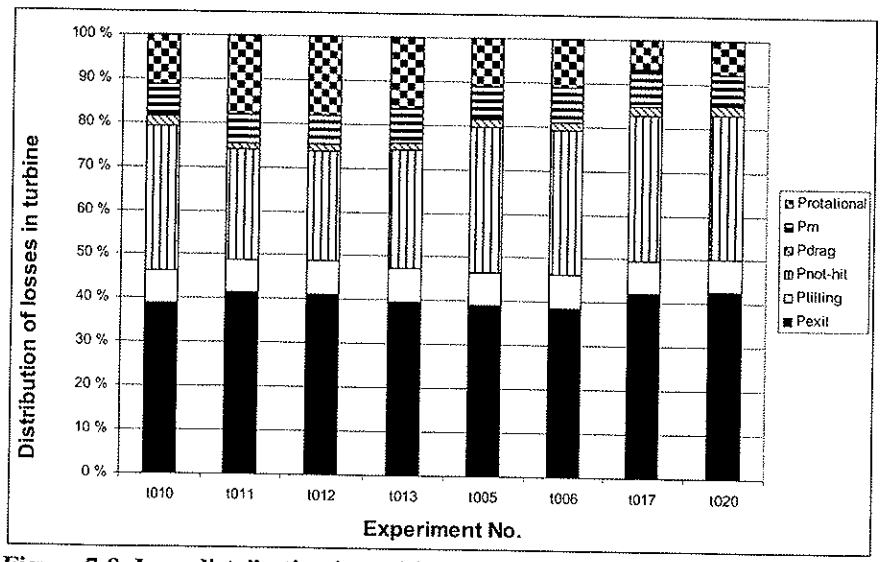

Figure 7-8. Loss distribution in turbine

The rotational losses will also be bigger with higher speeds, so this must be handled in the future. It is not surprising that the rotational losses are high, because there is no shielding of the turbine blades.

7.5 *Evaluation of methods*

7.5.1 Experimental methods

The experimental program was set up to extract as much information as possible about the energy conversion processes in the turbine as total, and in the individual components. The experimental program consisted of three parts

- Nozzle characterisation
- Turbine tests with blocked shaft
- Turbine tests with rotating turbine

With this program it should be possible to follow the losses through the machine and identify the weak points in the machine design.

Nozzle reaction power measures the average jet velocity, not measured is the flow homogeneity, and the radial velocity components in the nozzle flow. The nozzle jet visualisation tests were intended to give indications about the non-axial velocity components as the jet shape would be seen. Fluid dynamic conditions in the inspection glass made it impossible to see the nozzle jet at relevant process conditions, but at less violent conditions the jet shape could be seen. The flow homogeneity is important because differences in gas- and liquid velocities will lead to losses in the turbine because the liquid velocity will have an optimal turbine velocity lower than the average jet velocity.

The nozzle pressure profile was not measured either. Because of this, a fluid density profile was assumed through the nozzle, and the pressure profile was calculated by use of friction and conversion to velocity. A measurement of the pressure profile would have given more certain information about the nozzle energy conversion processes.

The turbine blocked shaft testing made it possible to investigate the turbine blade efficiency. Before turbine blades were tested, nozzle characterisation had been made. Therefore it was possible to have an impression about optimal values for the measured torques. When the rotating turbine is tested, losses due to friction between the rotating wheel and the surrounding medium are included. This makes it difficult to isolate the losses in the turbine blades.

Shaft power and expander efficiency were measured by expander performance testing. Some tests were also made in order to characterise frictional resistance in bearings and between rotor and fluid. For the bearing friction tests it is important to note that complete vacuum was not achieved, and according to the pressure cell, the chamber pressure was

0.09 bara. As tests for rotational friction were made at 40 bara, and the rotational friction is proportional to the pressure, it can safely be assumed that the small chamber pressure would not contribute considerably to the resistance. The measured bearing losses also corresponded well to the bearing friction losses quoted by the bearing supplier.

When the rotational resistance was measured with pressurised chamber, the whole rotational resistance due to shaft friction, bearing friction and turbine rotor friction was measured. The bearing friction was measured independently in vacuum, so the effect from shaft and rotor friction could be isolated. It was however not possible to isolate the rotor or the shaft friction as they were mounted in one piece.

7.5.2 Uncertainty in measurements

Instability in the glycol temperature entering the test facility was another important source of uncertainties, because instabilities here affected all process conditions in the rest of the test facility, and variations in the process conditions affected the uncertainty of the measured data. To have an acceptable uncertainty in the measurements, it was also important to have a relatively stable glycol-temperature entering the test facility. This was assured by allowing the glycol inlet temperature to have lower variations than ± 0.1 K during the experiments. For tests with blocked shaft, the glycol temperature was allowed to vary more than that. This lead to relatively high uncertainties, so the logging period was reduced in order to reduce the estimated uncertainty.

The uncertainty in the nozzle testing had consequences estimation of the nozzle jet velocity in the tests with blocked shaft, and in the turbine performance tests.

7.6 Potential for CO2 impulse expander

With acceptable turbine efficiency, and a convenient method for using the recovered expansion energy, impulse expander for CO_2 is a good idea because of simple geometry and compactness as discussed in 3.2.

Although the experimental results from testing of the current expander showed a poor efficiency, there is much room for improvement:

- The nozzle efficiency was around 60 %
- The nozzle jet was probably conical, which caused considerable fractions of the jet to by-pass the turbine blades.
- There were high bearing losses because they were grease lubricated
- The geometry gives high losses at inlet and discharge at normal conditions
- As the turbine did not reach the intended speed, the exit loss became high. This can be shown by evaluating the velocity diagrams at inlet and outlet as shown in Figure 3-7. When the turbine speed is low, the relative velocity (w) is high, and then the absolute velocity (c_2) at the outlet becomes high.

7.6.1 Radial impulse expander with improved design

The most obvious weak points of the current turbine design are

- Nozzle design was not ideally matched to the turbine size
- Outwards flow creates extra losses due to the energy equation
- Outwards flow gives too high tip speed and hereby friction losses
- Outwards flow causes non-optimal inlet angles
- Bearings had high losses

As a consequence of the identified weak points, following improved turbine design is suggested

- Nozzle design matched to the turbine size and correct outlet conditions, and with optimal nozzle geometry
- Nozzle inlet is starting at outer tube diameter to reduce loss because of sudden contraction
- Turbine wheel diameter is set to 10 mm, this will correspond to a turbine speed around 100000 rpm at normal operation conditions
- Discharged CO_2 must lead away from the turbine wheel in a controlled way, and turbine blades must be shielded.
- Inlet angle is set to 18°. This angle is chosen because it is impossible to achieve a completely tangential inlet on this kind of turbine.

- Outlet angle is set to 41°. This allows some rotation on the outlet, but it should not destroy the turbine efficiency too much.

7.6.2 Predicted efficiency for improved expander

For the efficiency predictions, the following assumptions are made:

- Design basis as given in Table 3-1
- A nozzle efficiency of 0.85 is assumed to be possible. Hays & Brasz (1996) used a nozzle with 84 % efficiency, but in a process with much higher expander effect. The nozzle loss analysis also showed some room for improvements.
- 10 mm turbine rotor diameter.
- 1.5 mm height of turbine blades
- The turbine will be a partial admission turbine with one nozzle.
- The nozzle must deliver a homogeneous jet in order to reduce two-phase losses as much as possible. This might require some development work on the nozzle.
- The discharged CO_2 must be evacuated from the turbine rotor so that the turbine is rotating in gas. Here some development work will be needed

With the inlet angle as given in 7.6.1, and the design basis as given in Table 3-1, this gives 111 krpm turbine speed, which means angular velocity $\omega = 11661$ Hz.

Velocity diagrams are shown for inlet and outlet in Figure 7-9. As shown, the chosen outlet angle will not give a completely radial outlet. At the same time the chosen outlet angle would not be expected to give a situation where discharged fluid hits the next turbine blade. But flashing in the discharged fluid could cause small droplets to hit the next turbine blade.

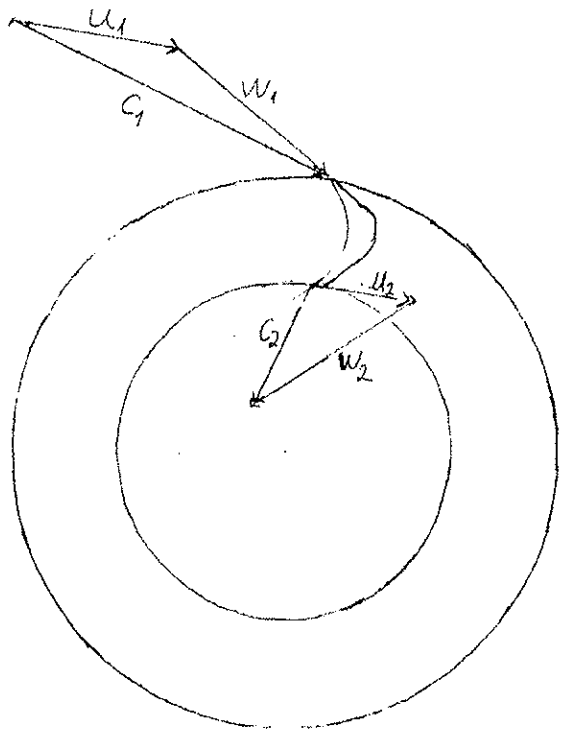

Figure 7-9. Inlet and outlet velocity diagram for radial inflow turbine

Based on experimental measurement of rotational losses at ω = 4000 Hz for turbine rotation in gas as given in 6.4.3, and reducing the value by the measured bearing loss as given in 6.4.2, the rotational losses for the improved turbine is by use of Eq (2-25) for extrapolation of the speed and correcting for the reduced dimensions, estimated to 96 W.

Windage losses are estimated by use of Eq (2-26), with k_v = 0.015 as recommended in Øverli (1992) for estimates, the following results were gained

- Density as two-phase fluid gives 105 W windage losses
- Density as saturated gas gives 43 W windage losses

In Øverli (1992) shielding of the turbine blades is also recommended in order to reduce windage losses.

Stagnation losses must be considered in the turbine operation. These losses can be minimized by making the turbine blades' inlet as sharp as possible.

Evaluating inlet and outlet velocity diagrams for the jet shows that the turbine construction causes 60 W exit loss. This loss is caused by a desire

for a high outlet angle so that the expanded fluid can be discharged near to radially into the middle of the turbine wheel as shown in Figure 7-9. The reason for this is that the discharge fluid must be handled; which requires some space. Shielding of turbine blades to reduce windage losses would also require some space.

This summarises to

Table 7-2. Loss analysis for improved turbine

P_{jet}	377,7
Disc friction loss	96
Windage loss	43
Drag loss between jet and blade	5,0
Exit loss	60
Hydraulic efficiency	0,46
Internal efficiency	0,39

The windage loss was calculated as for the turbine to rotate in pure gas.

7.6.3 Efficiency at reduced speed

Normally the optimal turbine speed is assumed to be the speed giving a tip speed

$$u = \frac{c_{1u}}{2}$$

This relationship is based on optimising the speed without accounting for losses related to rotation, such as rotational friction losses and windage losses. And it is strictly spoken valid only for a turbine where inlet and outlet diameter are equal. Using Equation (2-15) together with Equation (2-17) and adding losses due to rotation gives

$$P = \dot{m} \cdot \left(\frac{r_2}{r_1} \cdot \left(\frac{r_2}{r_1} + \frac{\cos(180-\beta_2)}{\cos\beta_{1u}} \right) \cdot u_1^2 - \left(1 + \frac{r_2}{r_1} \cdot \frac{\cos(180-\beta_2)}{\cos\beta_{1u}} \right) \cdot u_1 \cdot c_1 \cdot \cos\alpha_1 \right)$$
$$+ \left(k_R \cdot \rho \cdot R^2 + k_v \cdot D \cdot 8 \cdot h \cdot \rho \cdot (1-\varepsilon) \right) \cdot u_1^3$$

Differentiating the equation, setting equal to zero and using the following values

Table 7-3. Design data for reduced speed turbine

β_2	β_{1u}	α_1	$\dot{m}$	c_1	ε
41°	29 °	18°	0,05 kg/s	125 m/s	0,03
h	D	K_V	R	k_R	ρ
0,0016 m	0,01 m	0,015	0,005	0,17	100 kg/m^3

By using the values given in the table the optimal tip velocity becomes 49,6 m/s, which corresponds to ω = 9920 Hz . Using the same design basis as in the previous example, gives

Table 7-4. Performance data for reduced speed turbine

P_{jet}	377,7
Disc friction loss	59
Windage loss	25,5
Friction loss	5,0
Exit loss	86,3
Hydraulic efficiency	0,53
Internal efficiency	0,45

The rotational losses were both reduced by lowering the turbine speed. But the unpleasant consequence is that the exit loss increases and becomes very high. The internal efficiency of 0.47 does not include the following losses

- two-phase losses
- stagnation losses
- losses due to changing angles
- bearing losses

When the mentioned losses are added, the machine would be expected to have a lower efficiency than the estimated one.

If it is desirable to increase the efficiency further, one possible way is to reduce the discharge loss. One possible way of doing that is to use an axial impulse turbine, because it will be much easier to have small angles on inlet and outlet on such turbines. Using an axial impulse turbine would also make the handling of discharge CO_2 easier, and hereby allow for better control of the fluid dynamic conditions at the outlet.

7.7 Recommendations for further work

7.7.1 Prototype compressor-expander unit

As the expander is meant to work together with a high-speed compressor, it will be necessary to build a model compressor-expander unit to show that the expansion energy can be utilized by a high-speed compressor, and to show the total potential of energy recovery by high-speed equipment.

7.7.2 Pressure measurement along nozzle

The internal processes in the nozzle are of high importance to the function of the expansion machine. The experiments showed that there are challenges connected to designing an efficient nozzle. The calculations showed that some assumptions must be made regarding the nozzle pressure profile. If knowledge was gained regarding the nozzle pressure profile, it would give a deeper understanding of the energy conversion taking place in the nozzle. The experiments require a nozzle with internal diameter around 1 mm. For measuring the pressure profile, it would be necessary to drill 0.2 mm holes along the nozzle axial length. This will have some impact on the nozzle pressure profile, but it is important to note that the holes will cover small parts of the nozzle internal area. With such small holes, however, it is important to assure that the actual pressures are measured.

7.7.3 3D nozzle flow visualisation

In connection with nozzle design optimisation, it is important to assure that the nozzle jet is as homogeneous as possible. This because a non-homogeneous jet will cause losses arising from liquid droplets decelerating the turbine when there is differences between the gas and the liquid velocities of the turbine jet. The nozzle flow visualisation could be made with techniques as PIV (Particle Imaging Velocimetry). Compared to the visualisation tests that were made, use of PIV would give extra information, but it would also require extra instrumentation. And it would require a new nozzle flow inspection glass where the nozzle jet is not covered by secondary flow profiles. PIV can give information about

- Droplet velocity
- Amount of liquid

Alternatively a high-speed camera can be used. This will however give less information, but also cost less. The most important imformation is about the jet shape, and that can be retrieved by a high-speed camera.

7.7.4 Expander wheel flow visualisation

It would be useful to visualise the conditions at the turbine wheel inlet and in the turbine wheel. With a radial inflow impulse turbine, there will be challenges with regards to directing low-pressure two-phase CO_2 from the turbine wheel internals. Flow visualisation might be used to get an impression about how big this challenge is. Another important issue is stagnation losses at the turbine wheel inlet. For every turbine blade, the nozzle jet will be hitting from disadvantageous positions. And when it does, the jet will be deflected back towards the nozzle. This will have an impact on the turbine efficiency, and the extent of this loss should be investigated further.

7.7.5 Turbine blades' optimisation

In order to optimise the turbine, it is important to have an optimal shape of the turbine blades. This is difficult to achieve by experiments alone, but using CFD-modelling could be a possible way for predicting fluid dynamic conditions in the turbine wheel. CFD-modelling could also be used to estimate the impact of stagnation losses at the turbine blade entrance.

7.7.6 Shielding of the turbine blades

Considerable losses have been indicated due to reasons originating from non-optimal and un-controlled fluid flow conditions in and around the turbine rotor. These are losses due to expected back-flow through non-active turbine blades, and due to expected entrainment of discharge liquid around the turbine wheel. These losses will represent challenges for any turbine design as long as an impulse turbine is being used. The ability to handle such losses will also be crucial for the feasibility of an impulse turbine in work recovery from high-pressure CO_2. Shielding of the turbine blades in order to gain more control over the fluid dynamic conditions in and around the turbine blades will require small costs, and the effect of this action is important in evaluation of the potential for this type of expander.

References

Abdelmalek, F. T., "Centrifugal gas compressor-expander for refrigeration", United States Patent 5136854, Filed May 28 1991

Akagawa, K. & Asano, Y., "Performance of Pelton-type Turbine Driven by Gas-Liquid Two-phase flow", Bulletin of JSME, Vol. 29, No. 247, January 1986, pp. 106-112

Alamgir, Md. & Lienhard, J. H., "Correlation of Pressure Undershoot During Hot-Water Depressurization", Trans. ASME, 103 (1981), pp 52-55

Angus, S., Armstrong, B., DeReuck, K.M, "Carbon Dioxide - International thermodynamic Tables of The Fluid State", Pergamon Press, 1976

Balje, O. E., "TURBOMACHINES A guide to Design, Selection and Theory", John Wiley & Sons, New York, 1981, ISBN 0-471-06036-4

Baljé, O. E., "A Study on Design Criteria and Matching of Turbomachines: Part A-Similarity Relations and Design Criteria of Turbines", Journal of Engineering for Power Trans. ASME, January 1962, pp. 83-102

Baljé, O. E., "A Study on Design Criteria and Matching of Turbomachines: Part B-Compressor and Pump Performance and Matching of Turbocomponents", Journal of Engineering for Power Trans. ASME, January 1962, pp. 103-114

Blander, M. & Katz, J. L., "Bubble Nucleation in Liquids", AIChE Journal, Vol. 21, No. 5, 1975, pp 833-848

Blinkov, V. N., Jones, O. C. & Nigmatulin, B. I., "Nucleation and Flashing in Nozzles-2", Int. J. Multiphase Flow, Vol. 19, No. 6, 1993, pp. 965-986

Brändlein, J., Eschmann, P., Hasbargen, L., Weigand, K., "Ball and Roller Bearings Theory, Design and Application, 3rd ed.", John Wiley & Sons Ltd, West Sussex PO19 1UD, England, 1999

Brasz, J. J., "Improving the Refrigeration Cycle with Turbo-Expanders", Proceedings of the 19th International Congress of Refrigeration, Volume IIIa, pp. 246-253, 1995

Brekke, H. "Pumper & Turbiner", Vannkraftlaboratoriet NTNU, 1999

Corty, C. & Foust, A. S., "Surface Variables in Nucleate Boiling", Chem. Eng. Progr. Symp. Ser., Vol. 51, No. 17, 1955, pp. 1-12

Fenghour, A, Wakeham, W. A, Vesovic , V, "The Viscosity Of Carbon Dioxide", J. Phys, Chem. Ref. Data, vol. 27, issue 1, pp. 31-44, 1998

Fister, W., "Fluidenergiemaschinen Band 1", Springer-Verlag, Bochum, Germany, 1984

Försterling, S; Lauterbach, B.; Kaiser, H.; Köhler, J., "Experimentelle Untersuchungen eines Verdichters für Busklimaanlagen und Transportkälteanlagen mit Kohlendioxid als Kältemittel", DKV Tagungsbericht 1999, Berlin 17-19 November

Friedel, L., " Improved friction pressure drop correlation for horizontal and vertical two phase pipe flow", European Two phase Flow Group Meeting, Paper E-2, Ispra, June 5- 8, 1979

Fukuta, M.; Radermacher, R.; Lindsay, D.; Yanagisawa, T., "Performance of vane compressor for CO2 cycle", IIF-IIR Commissions, Purdue University, USA, 2000

Fukuta, M.; Yanagisawa, T.; Ogi, Y.; Radermacher, R., "Cycle performance of CO2 cycle with vane compressor-expander combination", International Conference on Compressors and their Systems, City University, London, UK, 2001

Fukuta, M.; Yanagisawa, T.; Radermacher, R., "Performance prediction of vane type expander for CO_2 cycle", International Congress of Refrigeration 2003, Washington, D. C.

Geankoplis, C. J., "Transport Processes and unit operations 3rd ed.", Prentice-Hall International, New Jersey, 1993. ISBN 0-13-045253-X

Gerhart, P. M.; Gross, R. J.; Hochstein, J. I., "Fundamentals of fluid mechanics" 2nd ed., Addison-Wesley Publishing Company, ISBN 0-201-18358-7, 1992

Gosney, W. B., "Principles of refrigeration", Ashford Overload Services Ltd.", Southampton, GB, 2000

Hays, L. G. & Brasz, J. J., "Two-Phase Turbines for Compressor Energy Recovery", Proceedings of the 1996 International Compressor Engineering Conference at Purdue, Vol. II, pp. 657-662

Hays, L. G. & Brasz, J. J., "Two-phase flow turbines as stand-alone throttle replacement units in large 2000-5000 ton centrifugal chiller installations", Proceedings of the 1998 International Compressor Engineering Conference at Purdue, vol. II, pp. 797-802, 1998

Heidelck, R. & Kruse, H., "Expansion machines for carbon dioxide based on modified reciprocating machines", IIF-IIR Commissions, Purdue University, USA, 2000

Heidelck, R. & Kruse, H., "CO2-Expansionsmaschinen auf der Basis modifizierter Hubkolbenmaschinen", KI Luft- und Kältetechnik, 3, 2001

Heyl, P., "Prozessberechnungen transkritischer CO_2-Prozesse mit arbeitsleistender Entspannung", KI Luft- und Kältetechnik, 8, 2001

Heyl, P.; Kraus, W. E.; Quack, H., Expander-compressor for a more efficient use of CO_2 as refrigerant", IIF-IIR – Commission, Oslo, Norway, 1998

Heyl, P.; Quack, H.; Kühne, M., "Kombinierte Expansions-Kompresions-Maschine für Kohlendioxid in Freikolbenbauweise", Industriepumpen + Kompressoren, Heft 1/2000

Heyl, P.; Maurer, T., « Versuchergebnisse transkritischer CO_2-Kältemaschinen mit arbeitsleistender Entspannung », KI Luft- und Kältetechnik 1/2002

Heyl, P. & Quack, H., "Free piston expander-compressor for CO_2 – Design, applications and results", 20th International Congress of Refrigeration, IIR/IIF, Sydney, 1999

Huff, H-J.; Lindsay, D.; Radermacher, R., "Positive displacement compressor and expander simulation", Purdue 2002

Huff, H-J.; Radermacher, R.; Preissner, M., "Experimental investigation of a scroll expander in a carbon dioxide air conditioning system" , International Congress of Refrigeration 2003, Washington, D. C.

Idelchick, I. E. "Handbook of hydraulic resistance, 3rd Edition", 1994, CRC Press, ISBN 0-8493-9908-4

Izumi, H., Harada, S., Matsubara, K. & Saito, S., "Development of small size claude cycle helium refrigerator with micro turbo-expander", Advances in Cryogenic Engineering, Vol. 31, 1986, pp. 811-818

Jonassen, O., "Rotasjonskompressor Et grunnlag for design av ulike typer tannhjulskompressorer", Institutt for Kuldeteknikk, NTH, Universitetet i Trondheim, 1991

Kim, Y., O'Neal, D. L., "A Comparison of Critical flow models for estimating two-phase flow of HCF22 and HFC134a through short tube orifices", Int. J. Refrig. Vol. 18, No. 7, 1995, pp. 447-455

Maurer, T. & Zinn, T., "Experimentelle Untersuchung von Entspannungsmaschinen mit mechanischer Leistungauskopplung für die transkritische CO_2-kältemaschine", DKV Tagungsbericht 1999, Berlin 17-19 November, Band II, 1999

Kwak, H-Y, & Lee, S., "Homogeneous Bubble Nucleation Predicted by a Molecular Interaction Model", Trans. ASME, Vol. 113, August 1991, pp. 714-721

Moffat, R. J., "Describing the uncertainties in experimental results", Experimental Thermal and Fluid Science, 1988, 1:3-17

Nickl, J.; Will, G.; Kraus, W. E.; Quack, H., "Third generation CO_2 expander", International Congress of Refrigeration 2003, Washington, D. C., USA, 2003

Peirs, J. Reynaerts, D. & Verplaetsen, F., "Development of an axial microturbine for a portable gas turbine generator", J. Micromech. Microeng. 13 (2003), pp. 190-195

Pitzer, K. S, Schreiber, D. R, "Improving equation-of-state accuracy in the critical region; Equations for Carbon Dioxide and Neopentane as examples", Fluid Phase Equilibria, vol. 41, 1988, pp. 1-17

Sato, S., Kakihara, K., Sakamoto, Y. & Nomura, i., "An experimental study on the efficiency of very low quality two-phase flow turbine", ASME/JSME Thermal Eng, Joint Conf., Honolulu, Hawai, 3 (1983) pp 207-214

Schlichting, H. & Gersten, K., "Boundary Layer Theory", 8th Revised and Enlarged Edition, Springer-Verlag Berlin Heidelberg 2000.

Shin, T. S. & Jones, O. C., "Nucleation and Flashing in Nozzles-1", Int. J. Multiphase flow, Vol. 19, No. 6, 1993, pp. 943-964

Sixsmith, H., Hasenbein, R. & Valenzuela, J. A., "A Miniature Wet Turboexpander", Advances in Cryogenic Engineering, Vol. 35, 1990, pp. 989-995

Sixsmith, H.; Miniature Expansion Turbines; "Advanced Cryogenics", C. A. Bailey, ed., Plenum Press, New York, (1971), p. 225.

Vesovic, V; Wakeham , W.A; Olchowy, G.A; Sengers, J.V; Watson, J.T.R; Millat, J.; "The Transport Properties Of Carbon Dioxide", J. Phys.Chem.Ref.Data, vol. 19, issue 3, pp. 763-808, 1990

Websters, J. G., "The Measurement, Instrumentation, and Sensors Handbook", CRC press, 1999

Xu, J. L., Chen, T. K., Chen, X. J., "Critical Flow in Convergent-Divergent Nozzles with Cavity Nucleation Model", Experimental Thermal and Fluid Science, 14 (1997), pp 166-173

Zha, S.; Ma, Y.; Sun, X., "The development of CO2 expander in CO2 transcritical cycles", International Congress of Refrigeration 2003, Washington, D. C., USA, 2003

Øverli, J. M., "Strømningsmaskiner bind 3 termiske maskiner", 2nd ed., Tapir forlag, Trondheim, 1992

Symbols list

Symbol	Explanation	Unit
A	Cross section area	m^2
C	Friction coefficient	
c	Absolute velocity	m/s
c_p	Specific heat capacity	J/kgK
d	Nozzle diameter	m
D	Turbine diameter	m
F	Force	N
g	Specific gravity	m/s^2
G_{cr}	Critical mass flow	kg/m^2h
h	Specific enthalpy	J/kg
H	Head	m
k	Slip ratio	
L	Length	m
l	Length	m
m	Mass flow	kg/s
n	Rotational speed	rpm
p	Pressure	Pa
P	Power	W
PCD	Pitch circle diameter	
Q	Heat	J
q	Specific heat	J
R	Radius	m
r_N	Local nozzle radius	m
r_C	critical bubble radius	m
s	Specific entropy	J/kgK
T	Temperature	K
U	Voltage signal	V
u	Tip speed	m/s
V	Volume flow	m^3/s
V_G	Bubble volume	
v	Specific volume	m^3/kg
v_{FG}		
w	Relative velocity	m/s
W	Work	J
x	Gas- or liquid fraction	
x	Refrigerant quality	
Y	Specific nozzle losses	J/kg
z	Axial coordinate	m

Dimensionless groups

Gb	Gibbs number	
Re	Reynolds number	
N_S	Turbine specific speed	
D_S	Turbine specific diameter	

Greek letters

α	Angle	
β	Angle	
Σ'	Constant rate of depressurization	
φ	Heterogeneity factor	
μ	Chemical potential	
ω	Angular velocity	rad/s
ξ	Resistance coefficient	-
ε	Process COP	
σ	Surface tension	N/m
η	Efficiency	
φ	Nozzle coefficient	
ρ	Density	kg/m^3
τ	Shaft torque	Nm

Appendix 1. Calculations and uncertainties in calculated values

State functions and basic properties

Inlet enthalpy

The inlet enthalpy is a function of temperature and pressure, h = h(t,p)

The uncertainty of the inlet enthalpy is then

$$\delta h_{in} = \sqrt{\left(\frac{\partial h_{in}}{\partial T}\delta T\right)^2 + \left(\frac{\partial h_{in}}{\partial p}\delta p\right)^2}$$

Inlet entropy

The inlet entropy is a function of temperature and pressure, s = s(t,p)

The uncertainty of the inlet entropy is then

$$\delta s_{in} = \sqrt{\left(\frac{\partial s_{in}}{\partial T}\delta T\right)^2 + \left(\frac{\partial s_{in}}{\partial p}\delta p\right)^2}$$

Isentropic outlet enthalpy

The outlet enthalpy is a function of inlet entropy and outlet pressure, h = h(t,p)

The uncertainty of the outlet enthalpy is then

$$\delta h_{out} = \sqrt{\left(\frac{\partial h_{out}}{\partial s}\delta s\right)^2 + \left(\frac{\partial h_{out}}{\partial p}\delta p\right)^2}$$

Isentropic enthalpy difference

The enthalpy difference is a function of the inlet enthalpy and the isentropic outlet enthalpy

The uncertainty of the isentropic enthalpy difference is then

$$\delta\Delta h_s = \sqrt{\left(\frac{\partial \Delta h_s}{\partial h_{out}}\delta h_{out}\right)^2 + \left(\frac{\partial \Delta h_s}{\partial h_{in}}\delta h_{in}\right)^2}$$

Estimated nozzle jet velocity

$$c_1 = \sqrt{\eta \cdot 2 \cdot \Delta h_s}$$

Hereby the uncertainty in the estimated nozzle jet velocity is

$$\delta c_1 = \sqrt{\left(\frac{\sqrt{2 \cdot \Delta h_s}}{2 \cdot \sqrt{\eta}}\delta\eta\right)^2 + \left(\frac{\sqrt{2 \cdot \eta}}{2 \cdot \sqrt{\Delta h_s}}\delta\Delta h_s\right)^2}$$

Optimal angular velocity

The optimal angular velocity as a function of c_1 and geometrical parameters is

$$\omega = \frac{c_1}{2 \cdot r} \cdot \cos\alpha_1 \cdot \cos\lambda$$

The uncertainty in ω is then

$$\delta\omega = \frac{\delta c_1}{2 \cdot r} \cdot \cos\alpha_1 \cdot \cos\lambda$$

Nozzle testing

Nozzle jet velocity

As c_0 contributes very little to the exit velocity, the uncertainty of c_0 is neglected in the calculation of the uncertainty of c_1

$$\delta c_1 = \sqrt{\left(-\dot{m} \cdot \delta F\right)^2 + \left(\frac{F}{\dot{m}^2} \cdot \delta \dot{m}\right)^2}$$

The uncertainty in c_1^2 is then

$$\delta c_1^2 = \left|2 \cdot c_1 \cdot \delta c_1\right|$$

Isentropic efficiency

The nozzle isentropic efficiency is

$$\eta_s = \frac{c_1^2}{2 \cdot \Delta h_s}$$

$$\delta \eta = \sqrt{\left(\frac{\delta c_1^2}{2 \cdot \Delta h_s}\right)^2 + \left(\frac{c_1^2}{2 \cdot \Delta h_s^2} \delta \Delta h_s\right)^2}$$

Blocked shaft testing

Optimal torque

The blocked shaft optimal torque is

$$\tau = \dot{m} \cdot c_1 \cdot \left(r_2 \cdot \cos(180 - \beta_2) + r_1 \cdot \cos\alpha_1\right) \cdot \cos\lambda$$

As geometrical parameters are not included in the uncertainty calculations, the optimal torque uncertainty is

$$\delta\tau = \sqrt{(c_1 \delta\dot{m})^2 + (\dot{m}\delta c_1)^2} \cdot \left(r_2 \cdot \cos(180 - \beta_2) + r_1 \cos\alpha_1\right) \cdot \cos\lambda$$

Torque ratio

$$\delta\left(\frac{M}{\tau}\right) = \sqrt{\left(\frac{\delta M}{\tau}\right)^2 + \left(\frac{M}{\tau^2}\delta\tau\right)^2}$$

Torque difference

$$\delta(\tau - M) = \sqrt{(\delta\tau)^2 + (\delta M)^2}$$

Non rotational losses

The sum of non rotational losses is estimated as

$$P_{non-rotational} = \frac{\tau - M}{2} \cdot \omega_{opt}$$

The uncertainty of the estimate is then

$$\delta P_{non-rotational} = \sqrt{\left(\frac{\omega_{opt}}{2}\delta(\tau - M)\right)^2 + \left(\frac{\tau - M}{2}\delta\omega_{opt}\right)^2}$$

Turbine performance

Shaft power

The shaft power is the energy that is delivered on the expander shaft. It is the most important property of the experiments. The power is not measured directly, but it is calculated as the product of the shaft torque and the angular velocity of the shaft. The shaft power is calculated by

$$P = M \cdot \omega$$

The uncertainty in the power is hereby

$$\delta P = \sqrt{\left(\frac{\partial P}{\partial M} \cdot \delta M\right)^2 + \left(\frac{\partial P}{\partial \omega} \cdot \delta \omega\right)^2} = \sqrt{(\omega \cdot \delta M)^2 + (M \cdot \delta \omega)^2}$$

Total efficiency

The energy efficiency of the expander characterizes the utilization of the available energy. It is an important parameter, because the use of expansion work recovery depends on an acceptable efficiency. The energy efficiency is calculated as the quotient between the shaft power and the isentropic available power

$$\eta_t = \frac{P_{shaft}}{P_{theoretic}} = \frac{M \cdot \omega}{\dot{m} \cdot (h_{ut} - h_{in})_s}$$

The uncertainty is then

$$\delta \eta_t = \sqrt{\left(\frac{\partial \eta_t}{\partial P_{theor}} \cdot \delta P_{theor}\right)^2 + \left(\frac{\partial \eta_t}{\partial P_{shaft}} \cdot \delta P_{shaft}\right)^2} = \sqrt{\left(\frac{P_{shaft}}{P_{theor}^2} \cdot \delta P_{theor}\right)^2 + \left(\frac{\delta P_{shaft}}{P_{theor}}\right)^2}$$

Where the uncertainty in the theoretical power, δp_{theor}, is

$$\delta P_{theor} = \sqrt{\left(\frac{\partial P_{theor}}{\partial \dot{m}} \delta \dot{m}\right)^2 + \left(\frac{\partial P_{theor}}{\partial h_{in}} \delta h_{in}\right)^2 + \left(\frac{\partial P_{theor}}{\partial h_{ut}} \delta h_{ut}\right)^2}$$

$$= \sqrt{\left((h_{ut} - h_{in})_s \delta \dot{m}\right)^2 + (\dot{m} \cdot \delta h_{in})^2 + (\dot{m} \cdot \delta h_{ut})^2}$$

Zero point uncertainty in nozzle tests

The analysis results from the regression analysis where the uncertainty in nozzle characterisation zero point was estimated are shown here. The uncertainty used is found under Regression Statistics-Standard Error. In uncertainty analysis 2x this value is used as uncertainty for reactive power zero point, which is the most important uncertainty in the reactive power measurement.

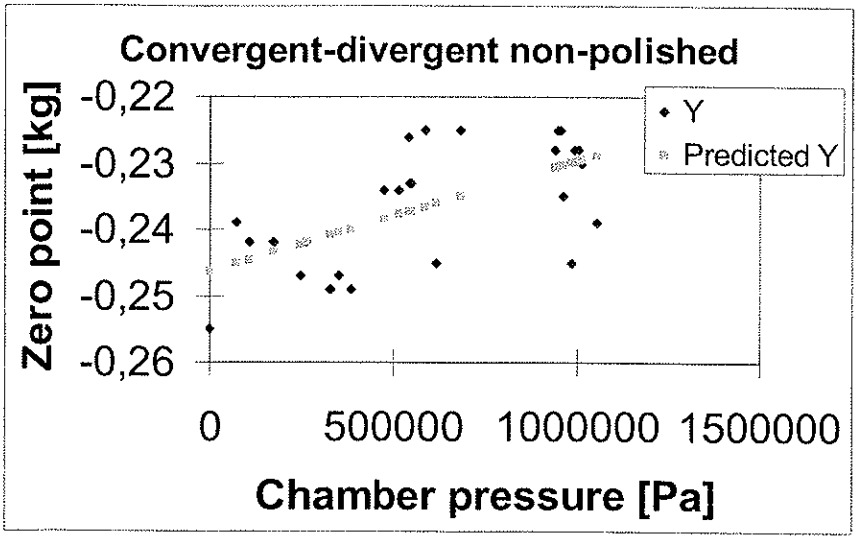

SUMMARY OUTPUT Convergent-Divergent Non-polished

Regression Statistics	
Multiple R	0,619444588
R Square	0,383711597
Adjusted R Square	0,358032914
Standard Error	0,007273922
Observations	26

ANOVA

	df	*SS*	*MS*	*F*	*Significance F*
Regression	1	0,000790623	0,000790623	14,94281	0,000739503
Residual	24	0,001269839	5,29099E-05		
Total	25	0,002060462			

	Coefficients	*Standard Error*	*t Stat*	*P-value*	*Lower 95%*	*Upper 95%*	*Lower 95,0%*	*Upper 95,0%*
Intercept	-0,246276473	0,002895016	-85,06911232	2,75E-31	-0,252251494	-0,2403015	-0,25225149	-0,240301453
X Variable 1	1,65944E-08	4,29286E-09	3,865592641	0,00074	7,73441E-09	2,5454E-08	7,73441E-09	2,54544E-08

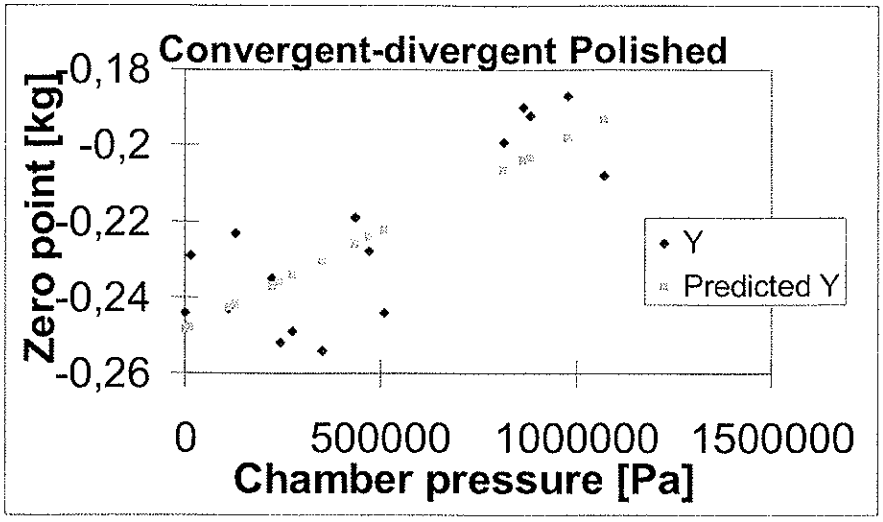

SUMMARY OUTPUT Convergent-Divergent Polished

Regression Statistics	
Multiple R	0,792213667
R Square	0,627602493
Adjusted R Square	0,601002672
Standard Error	0,014659467
Observations	16

ANOVA

	df	*SS*	*MS*	*F*	*Significance F*
Regression	1	0,005070401	0,005070401	23,59424	0,000253726
Residual	14	0,003008599	0,0002149		
Total	15	0,008079			

	Coefficients	*Standard Error*	*t Stat*	*P-value*	*Lower 95%*	*Upper 95%*	*Lower 95,0%*	*Upper 95,0%*
Intercept	-0,248501482	0,00611073	-40,66641419	6,18E-16	-0,261607694	-0,2353953	-0,26160769	-0,235395269
X Variable 1	5,15395E-08	1,06105E-08	4,857389904	0,000254	2,87622E-08	7,4297E-08	2,87622E-08	7,42968E-08

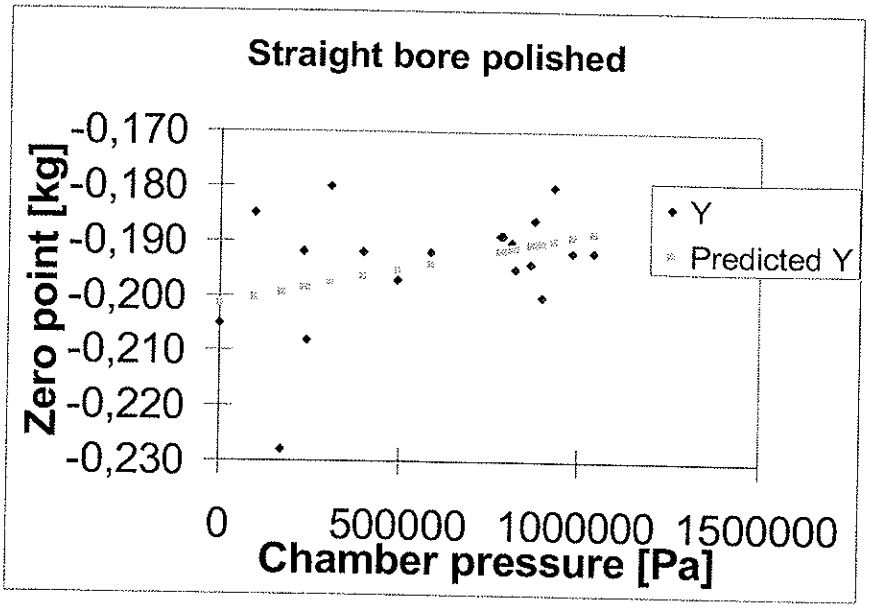

SUMMARY OUTPUT Straight bore Polert

Regression Statistics	
Multiple R	0,389515367
R Square	0,151722221
Adjusted R Square	0,101823528
Standard Error	0,010338423
Observations	19

ANOVA

	df	*SS*	*MS*	*F*	*Significance F*
Regression	1	0,000324989	0,000324989	3,040605	0,09825976
Residual	17	0,001817011	0,000106883		
Total	18	0,002142			

	Coefficients	*Standard Error*	*t Stat*	*P-value*	*Lower 95%*	*Upper 95%*	*Lower 95,0%*	*Upper 95,0%*
Intercept	-0,201503494	0,004913479	-41,01035426	1,93E-18	-0,211870026	-0,191137	-0,21187003	-0,191136961
X Variable 1	1,26163E-08	7,23521E-09	1,743733086	0,09926	-2,64869E-09	2,7881E-08	-2,6487E-09	2,78813E-08